Development of Nanomaterial-based Gas Microsensors for Environmental Application

Thesis submitted in accordance with the requirements of the University of Liverpool for the degree of Doctor in Philosophy

by

Lin Liu

School of Environmental Sciences

University of Liverpool

August 2019

Dedicated to my husband and loving family

邓小俊

Thank you for your unwavering support and unending love.

Declaration

I, **Lin Liu**, wish to declare that this thesis is my own independent work/investigation. It is being submitted in partial fulfillment of the requirement for the award of the requirements for the degree of PhD. I further declare that this work has never been submitted for any degree at this or any other University, and that the thesis is presented with the consent of my supervisor. Works by other authors, which served as a source of information, have been duly acknowledged by references to the authors. The views expressed are my own. I hereby give consent for my thesis, if accepted, to be available for photocopying and for inter-library loan, and for the title and summary to be made available to outside organizations.

Signed: _____

Lin Liu (Candidate)

5th August 2019

This page intentionally left blank

Abstract

Air pollution is a serious environmental problem that jeopardizes human' health. Inhalation of gas pollutants can cause many health problems such as respiratory disease, lung cancer, leukemia, or even death. Thus, development of new technologies and novel portable miniaturized sensors to detect trace gas pollutants has received significant attention. This study aims to develop high performance gas sensors by designing hierarchical nanostructured materials and new device structures.

In Chapter 2, novel brush-like (B-) ZnO@SnO_2 n-n hierarchical nanostructures (HNSs) were successfully synthesized by using a simple two-step hydrothermal method. The growth mechanism of the B-ZnO@SnO_2 HNSs was studied. The B-ZnO@SnO_2 HNS-based NO_2 sensor showed high sensing performance including high sensitivity (response value: 25.5 to1 ppm NO_2), fast response (< 60 s), and low detection limit (5 ppb). The enhanced sensing mechanism was attributing to the unique structure of B- ZnO@SnO_2 HNSs, which can provide large specific surface area and can induce synergism effect due to the formed multi-junctions.

In Chapter 3, NiO nanowalls decorated by SnO_2 nanoneedles (NiO@SnO_2) were directly grown on ceramic chips via a chemical bath deposition method to obtain uniform sensing materials without aggregation instead of using slurry-coating method, which is used in the Chapter 2. The morphologies and compositions of the NiO@SnO_2 HNSs were well tuned by varying the growth time to optimize the sensing performance. The response of the NiO@SnO_2 HNSs (2 h) to 1 ppm H_2S was over 23 times higher than that of the pure NiO nanowalls and 17 times higher than that of the pure SnO_2 nanosheets. This dramatic enhancement is mainly due to the large surface area of the NiO@SnO_2 HNSs and the p-n heterojunction at the hetero-interface of SnO_2 and NiO. The variation in the depletion layers (W_{SnO_2} and W_{NiO}) at the

interface of SnO_2 and NiO greatly depends on the properties of the target gases (*e.g.*, electron-withdrawing property (NO_2) or electron-donating property (H_2S)).

In Chapter 4, based on the in situ growth method ("bottom-up") which was reported in Chapter 3, a "top-down" and "bottom-up" combined strategy was proposed to manufacture wafer-scale miniaturized gas sensors with high-throughput by growth of patterned $Ni(OH)_2$ nanowalls at specific locations. First, micro-hotplates were fabricated on a two-inch (2") silicon wafer by micro-electro-mechanical-system (MEMS) techniques ("top-down" strategy). Then a template-guided controllable de-wetting method was used to assemble a thermoplastic elastomer (TPE) thin film with uniform micro-sized holes (relative standard deviation (RSD) of the size of micro-holes < 3.5 %, n >300), which serves as the mask for growing $Ni(OH)_2$ nanowalls ("bottom up" strategy). The obtained sensors based on these strategies showed great reproducibility of electric properties (RSD < 0.8%, n=8) and sensing performance toward H_2S (RSD <3.5%, n=8).

Different from the chemiresistive gas sensors reported in this thesis, which are driven by external power source, a novel device structure was proposed to construct photovoltaic self-powered H_2S sensor based on p-type single-walled carbon nanotubes (SWNTs) and n-type silicon (n-Si) heterojunction. The energy from visible light suffices to drive the device owing to a built-in electric field (BEF) induced by the differences between the Fermi energy levels of SWNTs and n-Si. Under 600 nm illumination (1.8 mW/cm^2), linearly self-powered detecting H_2S in the range of 100 ppb to 800 ppb was implemented, with fast response time (57 s) and recovery time (110 s) at room temperature. Compared with conventional chemiresistive sensor based on SWNTs, the response time and response of the photovoltaic self-powered device were significantly enhanced. When exposing to 400 ppb H_2S, the sensing response increased more than 4 times attributed to the BEF.

Overall, three different heterostructure-based gas sensors were studied to enhance their performance and the sensing mechanisms of the sensors were also investigated. Moreover, a novel “top-down” & “bottom-up” strategy was proposed for wafer-scale fabrication of miniaturized gas sensor.

Keywords:

gas sensor; hierarchical nanostructures; heterojunctions; self-powered; bottom-up; top-down

This page intentionally left blank

Acknowledgments

First and foremost, I would like to thank all the people that supported me on my journey. I am grateful to my dear supervisor, Dr. Sujie Qin, for all of her help and support and encouragement throughout my PhD studies. I would also like to appreciate Prof. Ting Zhang and Prof. George Wollf for being amazing mentors and for their patience and the many hours of insightful discussions. I also wish to thank Dr. Pascal Salaun, Dr. Zheng Chen and Dr. Bailiang Li for their valuable advises as the yearly progress committee members.

I would like to thank Yingyi Wang, who is a undergraduate student in XJTLU, for her assistance and useful discussions. I also want to express thanks to all the members of the Prof. Ting Zhang's Group for their valuable insights and constant motivation. Especially Yanbing Dai, Fuqin Sun, Dr. Guanghui Li, Dr. Shuqi Wang, Dr. Yuanyuan Bai and Dr. Qifeng Lu for their technical and academic suggestions and useful discussions. I also wish to express my appreciation to Prof. Wu Zhao, Prof. Zhengchun Peng, Prof. Xuewen Wang and their students (Manzhang Xu, Xiao Yan) and Prof. Yi Wang for offer the cooperation opportunity.

Finally, I want to acknowledge my classmates Williamson Gustave, Zhaofeng Yuan, Xiaokai Zhang, Qingqian Ning and Maede Faghihinia for their support and comfort once I feel sad. I also wish to express my immense gratitude to my loving family for their patience and support.

This page intentionally left blank

Contents

Declaration III

Abstract V

Acknowledgments IX

List of Figures XVII

List of Tables XXV

List of Abbreviations and Symbols XXVII

List of Publications and Author's Contributions XXXI

List of Conferences XXXIV

List of Patents XXXIV

Chapter 1: Overview of Gas Sensors Based on Heterostructural Metal Oxides 1

1.1. Motivation and Background 1

1.2. Development of Portable Gas Sensing Technologies 2

1.3. Basic Sensing Mechanism of Gas Sensors Based on Metal Oxides 4

1.4. Typical Sensing Mechanism of Gas Microsensors Based on Heterostructures 7

1.4.1. Sensing Mechanism of the Type-I Sensor Structure 8

1.4.2. Mechanism of the Type-II Sensor Structure 11

1.4.3. Sensing Mechanism of the Type-III Sensor Structure 18

1.5. Remaining Challenges 22

1.6. Research Aims and Objectives 23

1.7. References 26

Chapter 2: Design of Novel ZnO@SnO_2 n-n Heterostructures for Highly Sensitive NO_2 Sensing 36

2.1. Abstract 36

2.2. Introduction 37

2.3 Experimental Section 38

2.3.1 Synthesis of Materials. 38

2.3.2 Characterization 39

2.3.3 Gas Sensing Measurement 40

2.4. Results and Discussion 41

2.4.1 Structure and Morphology Characterization 41

2.4.2. Growth Mechanism of the B-ZnO@SnO_2 HNSs 44

2.4.3. Gas Sensing Performances of the B-ZnO@SnO_2 HNSs 51

2.4.4. Gas Sensing Mechanism of the B-ZnO@SnO_2 HNSs 53

2.5. Conclusions 55

2.6. Reference 57

2.7. Supplementary Data 67

Chapter 3: In situ Growth of NiO@SnO_2 p-n Heterostructures for High Performance H_2S Sensing 75

3.1. Abstract 75

3.2 Introductions 76

3.3 Experimental Sections 78

3.3.1 Synthesis of Material 78

3.3.2. Characterization 79

3.3.3. Gas Sensing Measurement 79

3.4. Results and Discussions 79

3.4.1. Structure and Morphology Characterization 79

3.4.2. Growth Mechanism of the $Ni(OH)_2$@SnO_2 HNSs 82

3.4.3. Gas-sensing Performance of NiO@SnO_2 HNSs 83

3.4.4. Gas Sensing Mechanism of NiO@SnO_2 HNSs 86

3.5. Conclusions 89

3.6. References 91

3.7. Supplementary Data 98

Chapter 4: In situ Growth of Patterned NiO Nanowalls for Wafer-scaled Miniaturized Gas Sensors Design and Fabrication 103

4.1. Abstract 103

4.2. Introduction 104

4.3. Experimental Section 105

4.3.1. Chemicals 105

4.3.2. Preparing Porous TPE Film 106

4.3.3. Characterization 106

4.3.4. Measurement of Gas Sensing Performance 107

4.4 Results and Discussion 108

4.4.1. Schematic of Fabrication of Wafer-scaled Gas Sensors 108

4.4.2. Effect of DFP Dots' Size to Assemble Porous TPE Film 110

4.4.3. Effect of the Concentration of TPE Solution to Assemble Porous TPE Film 113

4.4.4. Structure and Morphology Characterization 114

4.4.5. Sensing Performance of Fabricated Sensors 117

4.5 Conclusion.....119

4.6 References 120

4.7. Supplementary Data 125

Chapter 5: Design of Photovoltaic Self-Powered Gas Sensor Based on Single-Walled Carbon Nanotubes/Si p-n Heterojunction.....127

5.1. Abstract 127

5.2. Introduction 128

5.3. Experimental Section 129

5.3.1. Fabrication Process.....129

5.3.2. Characterization.....130

5.4. Results and Discussion.....130

5.4.1. Morphology Characterization.....130

5.4.2. Sensing Performance of Photovoltaic Self-powered Sensor.....132

5.4.3. Influence of the Wavelength of Illuminated Light 135

5.4.4. Sensing Mechanism of Photovoltaic Self-powered Sensor.....136

5.5. Conclusions 138

5.6. References 139

5.7. Supplementary Data 144

Chapter 6: General Conclusion and Future Work.....149

6.1 General Conclusion.....149

6.2. Future Work.....151

6.3. References.....155

This page intentionally left blank

List of Figures

Figure 1.1 Internet search results of web of knowledge on June 14th 2019 about the p-type and n-type metal oxide-based gas sensors. 4

Figure 1.2 Summary of most cited sensor performance enhancing mechanisms and the types of heterostructures that are most optimal for each mechanism type. Some types of mechanisms and structures have been omitted for space [44]. 7

Figure 1.3 Schematic graph of three types of device structure. 8

Figure 1.4 Schematic diagram of number of junctions in the three selected compositions; (a) SnO_2-rich composition; (b) $0{\cdot}5SnO_2$-$0{\cdot}5Co_3O_4$ composition; (c) Co_3O_4-rich composition; (d) the sensor resistance of $xSnO_2$-(1-x)Co_3O_4 compositions; (e) sensing response of $xSnO_2$-(1-x)Co_3O_4 compositions sensors to 10 ppm CO, acetone, C_6H_6, and SO_2 gases at 350 ℃ [50]. 11

Figure 1.5 Summary of gas response to 10 ppm of reducing gases (a), and oxidizing gases (b) based on pure SnO_2 nanowires and SnO_2@Cr_2O_3 nanowires; Schematic of sensing mechanism based on pure SnO_2 nanowires (c), and SnO_2@Cr_2O_3 nanowires (d), respectively [57]. 13

Figure 1.6 (a) NiO@SnO_2 nanofilms for ethanol sensing [61]; (b) WO_3@Ga_2O_3 nanofilms for ethanol sensing [58]. 14

Figure 1.7 Conceptual description showing the dual functional sensing mechanism of C−S NWs: (a) resistance modulation by radial modulation of the electron-depleted shell layer, (b) adverse effect by smearing on resistance modulation, and (c) total resistance modulation of C−S NWs by a combination of both effects [66]. 16

Figure 1.8 Schematic diagram of ethanol sensing mechanisms in NiO@ZnO C-S nanotubes with different ZnO ALD cycles. (a), (b) Discontinuous ZnO nanoparticle shell model. (c) Quasi-continuous ZnO nanoparticle shell model. (d), (e) Continuous ZnO nanoparticle shell model [73]. 17

Figure 1.9 (a) Schematic drawings of the p-NiO/n-SnO_2 nanohelixes; (b) H_2 and (c) NO_2 sensing properties of the p-NiO/n-SnO_2 nanohelixes heterojunction sensor at 200 °C [76]. ..19

Figure 1.10 (a), (d) Schematic pictures of photovoltaic self-powered gas sensors based on Si/ZnO p-n heterojunction; (b) Linear relation between measured V_{oc} and the number of diodes under illumination; (c) Self-powered sensing responses of sensor toward oxidizing (O_2) and reducing (1000 ppm ethanol) gases under solar illumination [80, 82]. ……....21

Figure 2.1 (a) SEM images, (b) XRD pattern and (c) EDXS spectrum of B-ZnO@SnO_2 HNSs. 41

Figure 2.2 (a) SEM image of B-ZnO@SnO_2 HNSs and the EDXS line profile in the radial direction, (b) The EDXS line-scan spectrum and (c-f) elemental mapping patterns of Sn, O, and Zn of B-ZnO@SnO_2 HNSs. 42

Figure 2.3 (a) TEM image of B-ZnO@SnO_2 HNSs, (b) SAED and (c) HRTEM image of SnO_2 nanowire.....43

Figure 2.4(a) XPS survey spectrum of B-ZnO@SnO_2 HNSs, (b) Sn 3d region, (c) Zn 2p region, (d) O1s region (full) with the corresponding fits for lattice oxygen in crystalline ZnO (red) and SnO_2 (green).....44

Figure 2.5 (a-f) The SEM images (Scale bars, 2 μm) and (g) XRD patterns of B-ZnO@SnO_2 HNSs at 200 °C for different reaction time: (a) 15 min, (b) 2, (c) 6, (d) 10, (e) 20, (f) 24 h. .45

Figure 2.6 The SEM images (Scale bars, 2 μm) and (g) XRD patterns of B-ZnO@SnO_2 HNSs with different reaction temperature: (a) 160, (b) 170, (c) 180, (d) 190, (e) 200, (f) 210 °C for 20 h.....46

Figure 2.7 Schematic illustration of the reasonable growth mechanism of B-ZnO@SnO_2 HNSs. 48

Figure 2.8 (a-b) The tilted view SEM images of well–aligned SnO_2 nanowires grow on ZnO non-polar surface along the [001] direction. (c) HRTEM image of the interfacial area of B-

ZnO@SnO_2 HNSs. (d-e) FFT images of selected areas on SnO_2 nanowire and ZnO nanorod marked by the squares 1 and 2 in Figure 2.8c, respectively. (f) High magnification image of the interfacial area marked by the dotted box 3 in Figure 2.8c. (g) Interfacial area (green plane) of [001]-growth-orientation SnO_2 nanowires. (h) Atoms arrangements of the SnO_2 interfacial area in panel g, (i) The schematic representation of the atomic configuration of the B–ZnO@SnO_2 interface viewed along the [0001] direction of ZnO. 50

Figure 2.9 (a) Real-time response of the B-ZnO@SnO_2 HNSs sensor to NO_2 from 5 ppb to 10 ppm. (b) The linear relationship of the B-ZnO@SnO_2 HNSs sensor to NO_2 in the range of 5 ppb to 800 ppb and 1 ppm to 10 ppm. (c) Selectivity comparison of pure ZnO, SnO_2, and B-ZnO@SnO_2 HNSs sensors for different target gases at 1 ppm.....52

Figure 2.10 Schematic illustration of the sensing mechanisms with respect to (a) SnO_2 nanowires and (b) B-ZnO@SnO_2 HNSs; schematic diagrams of B–ZnO@SnO_2 at different stage: (c) Energy band diagram of SnO_2-ZnO system. Energy band diagram of SnO_2-ZnO heterojunction after contact in vacuum (d), in air (e), and in NO_2 (e).....55

Figure 3.1Schematic diagrams of the bare ceramic microchip (a), with $Ni(OH)_2$ nanowalls (b), and $Ni(OH)_2$@SnO_2 hierarchical nanostructures (HNSs) (2 h) (c); SEM images of $Ni(OH)_2$@SnO_2 HNSs with different reaction time: (f) 2 h, (g) 4 h, (h) 8 h and (i) 12 h. 80

Figure 3.2 (a) XRD patterns of the prepared $Ni(OH)_2$, SnO_2, and different $Ni(OH)_2$@SnO_2 HNSs and PET substrate; (b) TEM, and (c) HRTEM and the corresponding fast Fourier transform (FFT) of $Ni(OH)_2$ nanowall; (d) TEM, and HRTEM and the corresponding fast Fourier transform (FFT) images of SnO_2 nanoneedle (2 h) at the edge of $Ni(OH)_2$ nanowall. 82

Figure 3.3 Schematic graph of the proposed growth processes of $Ni(OH)_2$@SnO_2 HNSs. 83

Figure 3.4 (a) Operating temperature dependence sensing response of NiO@SnO_2 HNS (2 h)-based sensor to 1 ppm H_2S; (b) Real-time response of sensors based on different NiO@SnO_2

HNSs (2, 4, 8, and 12 h), pure NiO nanowalls and pure SnO_2 nanosheets to different concentration of H_2S (ranging from 0.2 to 1 ppm); (c) Selectivity of sensors 2, 4, 8, and 12 h) to different gases with same concentration (0.5 ppm); (d) Real-time response of the sensor based on NiO@SnO_2 HNSs (2 h) to different concentration of H_2S (0.1 – 50 ppm) and (e) linear relationship of sensing response verse different concentration of H_2S; (f) Sensing response of sensor (2 h) to 1 ppm H_2S of day one and one month later. 86

Figure 3.5 (a) Schematic band gap structure of NiO@SnO_2 p-n heterojunction; (b) Schematics show changes of the conduction channel when exposure to different gases such as air, H_2S, and NO_2. 87

Figure 4.1 (a) schematic of a top-down and bottom-up combined strategy for fabricating wafer-scale miniaturized gas sensors; (b) schematic of template-guided controllable de-wetting and in situ growth steps during wafer-scale fabrication process and relevant photograph results of some steps: (1) patterned dry film photoresist (DFP) dots were formed on the two-inch (2”) micro-hotplate wafer via photolithography; (2) the formed of water droplet array on the surface of DFP dots; (3) spin-coating of 18% TPE solution and waiting for evaporation of n-hexane; (4) the formed uniform porous TPE film with a gap to the DFP dots; (5) strip off of the DFP dots; (6) in situ growth of $Ni(OH)_2$ nanowalls; (7) peel off of the porous TPE film.....110

Figure 4.2 (a-c) the photographs of porous TPE films and the size distribution of micro-holes based on different sizes of DFP dots. From left to right of each row are the picture of assembled TPE film on the micro-hotplates surrounding the DFP dots, the picture of porous TPE film after stripping off the DFP dots, the size distribution mapping and histogram graphs of size of the micro-holes, respectively. 111

Figure 4.3 Sross-sectional SEM images of TPE film on polyethylene terephthalate (PET) substrate obtained from different concentration of TPE solution: (a) 10%; (b) 18%; (c) 25%; (d) the peel off result of the porous TPE film (10%) after in situ growth of $Ni(OH)_2$ nanowalls;

(e) the peel off result of the porous TPE film (10%) after in situ growth of $Ni(OH)_2$ nanowalls and annealed at 400 ℃ for 2 h; (f) the photograph of spin-coated TPE film (25%) after spin-coating ethanol. 113

Figure 4.4 (a) The optical picture of wafer-scale micro-hotplate; (b-i) SEM images of 8 sensors which are randomly chosen in the marked area of the wafer-scale micro-hotplate. Scale bar of sensor chip is 500 μm and for NiO nanowalls is 5 μm. 114

Figure 4.5 (a) FTIR result of DFP after Standard UV exposure (10 s) and contact angle results of Si_3N_4 and DFP (inset pictures); (b) a series of optical images of process (from stage 1 to stage 4) of forming water droplets based on template-guided controllable de-wetting method using 400 μm DFP dots.....115

Figure 4.6 (a) I-V curves of heating electrodes of eight gas sensors from -2 V to 2 V (inset graph is the box chart of resistance of heating electrodes); (b) I-V curves of eight sensors at different heating voltage; (c) heating voltage dependent responses of eight gas sensors to 5 ppm H_2S; (d) dynamic response of eight gas sensors to different H_2S concentrations; (e) scatter graph of response to various H_2S concentrations (inset graph is the linear relationship of logarithm of response with the logarithm of H_2S concentrations); (f) response of eight gas sensors toward different gases and the concentration is 5 ppm. 117

Figure 5.1 (a) The schematic graph of photovoltaic self-power H_2S sensor based on SWNTs/Si heterojunction. Electrode A (Ti/Au) is sputtered on SiO_2 layer, while Electrode B (Ti/Au) is on the bare n-Si. (b), (c) SEM images of device and the formed SWNT film. (d) The current density-voltage (J-V) curves of self-power H_2S sensor in dark and illuminated circumstance (λ = 600 nm, P = 1.8 mW/cm^2, applied potential: -2 V to 2 V). The red line is the J-V curve of self-power sensor at dark state, while the dark line is J-V curve when exposing to light. 132

Figure 5.2 (a), (c), (d) The response of devices to different H_2S concentrations based on SWNTs/Si, SWNTs-only, and n-Si-only, respectively. The measurements are carried at zero bias with light illumination (λ = 600 nm, P = 1.8 mW/cm^2) to monitor the changing of open-circuit voltage (V_{oc}). (b) The response of the device to difference H_2S concentration under 600 nm light and its corresponding fitting curve (R^2=0.996).....134

Figure 5.3 (a) The sensing response of photovoltaic self-powered H_2S sensor when applied different wavelength light (420 nm and 600 nm) with same power intensity (1.8 mW/cm^2); (b), (c) The schematic band diagram of the photovoltaic self-powered device at dark and illumination state. 136

Figure S 2.1 (a) XRD and (b) SEM image of ZnO nanorod. …..... 67

Figure S 2.2 The SEM images (Scale bars, 2 μm) of B-ZnO@SnO_2 HNSs at 200 °C with different reaction time: (a) 15, (b) 30 min, (c) 1, (d) 2, (e) 4, (f) 6, (g) 8, (h) 10, (i) 12, (j) 16, (k) 20, (l) 24 h. 67

Figure S 2.3 The XRD patterns of B-ZnO@SnO_2 HNSs at 200 °C for different reaction time. 68

Figure S 2.4 The SEM images (Scale bars, 2 μm) of B-ZnO@SnO_2 HNSs with different reaction temperature: (a) 160, (b) 170, (c) 180, (d) 190, (e) 195, (f) 200, (g) 205, (h) 210 °C for 20 h.....68

Figure S 2.5The XRD patterns of B-ZnO@SnO_2 HNSs at 200 °C with different reaction temperature. 69

Figure S 2.6 (a) XRD and (b) SEM image of SnO_2 nanowires. 69

Figure S 2.7 (a) Real–time response of the B-ZnO@SnO_2 HNSs sensor to NO_2 from 500 ppb to 10 ppm over 7 months. 69

Figure S 2.8 Reproducibility characterization of the B-ZnO@SnO_2 HNSs based sensor to 500 ppb and 1 ppm NO_2 over 7 months.....70

Figure S 2.9 Reproducibility characterization of the B-ZnO@SnO_2 HNSs based sensor under the relative humidity of 85% over 7 months. 70

Figure S 2.10 (a) Optical photograph of the micro hotplate. (b) SEM images of the B-ZnO@SnO_2 HNSs sensor and (c–d) the B-ZnO@SnO_2 HNSs bridging the two electrodes. 101

Figure S 3.1 SEM images (Scale bar: 1 μm) of prepared $Ni(OH)_2$@SnO_2 hierarchical nanostructures (HNSs) before and after annealing treatment. 98

Figure S 3.2 XRD pattern of pure SnO_2. 98

Figure S 3.3 The SEM images (Scale bars, 500 nm) of (a) pure $Ni(OH)_2$ nanowalls and $Ni(OH)_2$@SnO_2 HNSs under different reaction times: (b) 0.5 h, (c) 1 h, (d) 2 h, (e) 4 h, and (f) 8 h. 99

Figure S 4.1 Pictures of a designed fixture (a) is used for in situ growth of $Ni(OH)_2$ nanowalls; (b) is used for wet-etching of silicon on the back of micro-hotplate wafer. 125

Figure S 4.2 Temperature distribution simulation result on micro-hotplate. 125

Figure S 4.3 XRD patterns of grown $Ni(OH)_2$ and NiO nanowalls on silicon substrate with a layer of SiO_2. 126

Figure S 4.4 A series of optical images of process (from stage 1 to stage 4) of forming water droplet array based on template-guided method using different size of DFP dots (500 μm (a), and 300 μm (b), respectively). 126

Figure S 5.1 Schematic fabrication process of gas sensor. 144

Figure S 5.2 (a), (c) The EDXS results of sensor at different locations; (b) The SEM image of the sensor at specific. 145

Figure S 5.3 (a) The Current-Voltage (I-V) curves of SWNTs-only device after annealed treatment. (b) The Current-Voltage (I-V) curves of n-Si-only device. 145

Figure S 5.4 Schematic graph of gas sensor testing process, all parts of the testing system are vertically placed. 146

Figure S 5.5 The sensing response of photovoltaic self-powered gas sensor under dark state. 146

Figure S 5.6 Dynamic response of conventional SWNTs-only device to different H_2S concentration (V_{ds} = 2 V, λ = 600 nm, P = 1.8 mW/cm^2).....147

Figure S 5.7 Dynamic response of sensor to different concentration of H_2S at day one (a), and after five days (b) (λ = 600 nm, P = 1.8mW/cm^2). 147

List of Tables

Table 1.1 Comparison of three types of gas sensors (e: excellent; g: good; p: poor; b: bad) [11]. 2

Table 4.1 The size dispersion of micro-holes based on different size of DFP dots.....112

Table S 2.1 NO_2 gas sensing abilities of SnO_2-ZnO composite materials. 71

Table S 3.1 EDXS results of $Ni(OH)_2$@SnO_2 HNSs 99

Table S 3.2 Comparison results of H_2S sensors based on NiO-SnO_2 system and NiO-based and SnO_2-based nanomaterials in recent few years. 100

This page intentionally left blank

List of Abbreviations and Symbols

Abbreviations

ALD	Layer Deposition
B-	Brush-like
BEF	Build-in-electric Field
C-S	Core-shell
D	Diameter
DFP	Dry Film Photoresist
EC	Electrochemical
EDL	Electron-depletion Layer
EDXS	Energy Dispersive X-ray Spectrometer
EPA	Environmental Protection Agency
FFT	Fast Fourier Transform
FTIR	Fourier Transform Infrared Spectroscopy
GC	Gas Chromatography
HAL	Hole-accumulation Layer
HNSs	Hierarchical Nanostructures
IR	Infrared
LVQ	Learning Vector Quantization

NAAQS	National Ambient Air Quality Standards
MEMS	Micro Electro Mechanical System
MS	Mass Spectrometry
n-Si	N-type Silicon
PCA	Principal Component Analysis
PID	Photoionization Detector
PLS	Partial Least Squares
RE	Reference Electrode
RH	Relative Humidity
RIE	Reactive Ion Etching
RSD	Relative Standard Deviation
SAED	Selected Area Electron Diffraction
SEM	Scanning Electron Microscope
SWNTs	Single-walled Carbon Nanotubes
TEM	Transmission Electron Microscope
TMAH	Tetramethylammonium Hydroxide
TPE	Thermoplastic Elastomer
UV	Ultraviolet
VOC	volatile Organic Compounds
WE	Working Electrode

XRD	X–ray Powder Diffraction
XPS	X-ray Photoelectron Spectroscopy
ZHS	$ZnSn(OH)_6$

Symbols

E_c	Conduction Band
E_v	Valency Band
E_f	Fermi Level
D_n	Electron Diffusion Coefficient
D_p	Hole Diffusion Coefficient
I_s	Reverse Saturation Current
I_L	Photogenerated Current
L_n	Electron Diffusion Length
L_p	Hole Diffusion Length
n_{n0}	Electron Concentration
p_{n0}	Hole Concentration
k	Boltzmann Constant
T	Absolute Temperature
V_{ds}	Source-drain Bias Voltage
V_{oc}	Open-circuit Voltage

ΔE_v	Difference Value of Valence Band
ΔE_c	Difference Value of Conduction Band
V_{bi}^0	Built-in Potential
$\Delta\Phi_{hetero}$	Heterojunction Potential Barrier
$\Delta\Phi_{homo}$	Homojunction Potential Barrier
λ_d	Debye Length

List of Publications and Author's Contributions

1. Zhiyong Zhang*[#], Manzhang Xu[#], **Lin Liu**[#], Xiongfei Ruan, Junfeng Yan, Wu Zhao, Jiangni Yun, Yingnan Wang, Sujie Qin, Ting Zhang, Novel SnO_2@ZnO hierarchical nanostructures for highly sensitive and selective NO_2 gas sensing. Sensors and Actuators B, 2018, 257, 714–727. (**co-first author, Chapter 2 is finished based on this article**)

The paper work of this publication is finished by Manzhang Xu and **Lin Liu**. Prof. Zhiyong Zhang is responsible for TEM and XPS characterization and data analysis; Manzhang Xu is responsible for XRD, EDXS, and SEM characterization and relevant data analysis; **Lin Liu** is responsible for fabrication of sensors, measurement of sensing performance and analysis of data; other authors provide some suggestions when discussing growth and sensing mechanisms. The foundations of this work are provided by Prof. Zhiyong Zhang, Prof. Wu Zhao, and Prof. Ting Zhang.

2. **Lin Liu**, Guanghui Li, Yanbing Dai, Yingyi Wang, Shuqi Wang, Tie Li, Ting Zhang, Sujie Qin, In situ Growth of NiO@SnO_2 Hierarchical Nanostructure for High Performance H_2S Sensing (**Under review, Chapter 3**)

All the paper work and data analysis are finished by **Lin Liu** and most of the data including SEM, EDXS, sensing performance are also collected by **Lin Liu**. Dr. Guanghui Li offers some useful suggestions when proposing the growth mechanism. Yanbing Dai assists me to test the sensing performance. The XRD data is collected by Yingyi Wang. The foundations of this work are provided by Dr. Shuqi Wang, Dr. Tie Li, Prof. Ting Zhang and Dr. Sujie Qin's applied foundations.

3. **Lin Liu**, Yingyi Wang, Fuqin Sun, Yanbing Dai, Shuqi Wang, Yuanyuan Bai,

Lianhui Li, Tie Li, Ting Zhang, Sujie Qin, 'Top-down' & 'Bottom-up' Strategies to Fabricate Wafer-scale Miniaturized Gas Sensors (**Under review, Chapter 4**)

All the paper work and data analysis are finished by **Lin Liu** and the fabrication strategy is proposed and conducted by **Lin Liu**. Most of the data including SEM, FTIR, contact angle, size distribution of micro-hole size of porous TPE film, photographs, sensing performance measurement are collected by **Lin Liu.** Both Yingyi Wang and Yanbing Dai assist me to count the size of micro-hole of porous TPE film as well as measure sensing performance. Fuqin Sun assists me to laminate dry film photoresist. Yuanyuan Bai is responsible for the COMSOL simulation of temperature distribution of micro-hotplate. Dr. Shuqi Wang gives a hand to revise the paper. The foundations of this work are provided by Dr. Shuqi Wang, Dr. Tie Li, Prof. Ting Zhang and Dr. Sujie Qin's applied foundations.

4. **Lin Liu**[#], Guanghui Li[#], Yi Wang, Yingyi Wang, Tie Li, Ting Zhang, Sujie Qin, A photovoltaic self- powered gas sensor based on a single-walled carbon nanotube/Si heterojunction. Nanoscale, 2017, 9, 18579-18583. **(Chapter 5)**

All the paper work, data collection and data analysis are finished by **Lin Liu**. Dr. Guanghui Li designs the structure of the micro-electrode chip and Dr. Yi Wang contributes to revise the paper. Yingyi Wang assists me to finish sensing performance measurement. The foundations of this work are provided by Dr. Yi Wang, Dr. Tie Li, Prof. Ting Zhang and Dr. Sujie Qin's applied foundations.

Other publications produced during my PhD studies

1. **Lin Liu**[#], Yingyi Wang[#], Guanghui Li, Sujie Qin, Ting Zhang, Ultrathin Free-standing Graphene Oxide Film Based Flexible Touchless Sensor, Journal of Semiconductors, 2018, 39, 206-211.

2. Wu Zhao*[#], **Lin Liu**[#], Manzhang Xu, Xuewen Wang, Ting Zhang, Yingnan Wang, Zhiyong Zhan g, Sujie Qin, Ting Zhangl., Single CdS Nanorod for High Responsivity UV/Visible Photodetector. Advanced Optical Materials, 2017, 1700159, 1-7. (**co-first author**)

3. Guanghui Li[#], **Lin Liu**[#], Guan Wu, Wei Chen, Sujie Qin, YiWang, Ting Zhang, Self-Powered UV–Near Infrared Photodetector Based on Reduced Graphene Oxide/n-Si Vertical Heterojunction, Small 2016, 12, 5019-5026. (**co-first author**)

4. Yan Xiao[#], **Lin Liu**[#], Zhihao Ma, Weihui Ou, Sujie Qin, Bo Meng, GeBo Pan, Ting Zhnag, Zhengchun Peng, High-performance self-powered ultraviolet photodetector based on CoPc and porous GaN p–n vertical heterojunction, Nanomaterials (**co-first author, Minor revision**)

5. Chunyan Qu[#], Shuqi Wang[#], **Lin Liu**, Yuanyuan Bai, Lianhui Li, Fuqin Sun, Mingming Hao, Tie Li, Qifeng Lu, Lili Li, Sujie Qin, Ting Zhang, Bioinspired Flexible VOCs Sensor Based on Dynamic Surface Wrinkling with Dual-Signal Response, Small, 2019, DOI: 10.1002/smll.201900216.

6. Shuqi Wang, Chunyan Qu, **Lin Liu**, Lianhui Li, Tie Li, Sujie Qin, Ting Zhang, Rhinophore bio-inspired stretchable and programmable electrochemical sensor, Biosensors and Bioelectronics, 142(2019) 111519.

7. Qifeng Lu, Fuqin Sun, **Lin Liu**, Lianhui Li, Yingyi Wang, Mingming Hao, Zihao Wang, Shuqi Wang, and Ting Zhang, Biological Receptor Inspired Flexible Artificial Synapse Based on Ionic Dynamics **(Submitted)**.

List of Conferences

[1] **Lin Liu**, Guanghui Li, Yingyi Wang, Sujie Qin "Novel Self-powered Microsensors Based on Carbon Nanomaterials" Xian Jiaotong-Liverpool University Graduate Students Poster Day, Suzhou, China (Poster).

[2] **Lin Liu**, Yingyi Wang, Ting Zhang, Sujie Qin, "Self-powered Microsensors Based on p-n heterojunction for trace gas pollutant detection" The 9th National Conference on Environmental Chemistry (2017), Hangzhou, China (Poster).

[3] **Lin Liu,** Yingyi Wang, Fuqin Sun, Yanbing Dai, Shuqi Wang, Ting Zhang, Sujie Qin, "'Top-down' & 'Bottom-up' Strategies to Fabricate Wafer-scale Miniaturized Gas Sensors" BIT's 7th Annual Conference of AnalytiX-2019 (2019), Singapore (Oral).

List of Patents

Lin Liu, Ting Zhang, Sujie Qin, Yingyi Wang, "Top-down" & "Bottom-up" Strategies for Wafer-scaled Miniaturized Gas Sensors Fabrication and Application, China (Application Number: 201910720998.5)

Chapter 1: Overview of Gas Sensors Based on Heterostructural Metal Oxides

1.1. Motivation and Background

Air pollution is becoming a growing concern and a serious worldwide environment problem that threatens human and organism's well being. Reaction products of natural activities, combustion products of solid fuels, and exhausts of vehicles and industries are three main air pollution sources, which emit various gas pollutants (*e.g.*, volatile organic compounds (VOCs), NOx, SO_2, O_3, H_2S, NH_3, and so forth) [1-5]. Inhalation of gas pollutants can cause many health problems such as respiratory disease, lung cancer, leukemia, or even early death [6-9]. It is reported that from 2012 to 2016, millions of people died from air pollution and billions of people face unsafe air every year [10]. All the gas pollutants can be divided into two classes, namely, reducing gases and oxidizing gases based on their chemical properties. Among the gas pollutants, NO_2 and H_2S are typical oxidizing and reducing gases, respectively, and have aroused great interest in the field of air pollution monitoring. Although some standard analytical methods have been developed to detect and distinguish gas pollutants based on laboratory analytical instruments (*e.g.*, Mass Spectrometry (MS), Gas Chromatography (GC), and Fourier Transform Infrared Spectroscopy (FTIR)), these instruments are bulky, analyses are expensive and time consuming, and so cannot provide real-time feedback. Therefore, the development of portable miniaturized gas sensors to obtain real-time feedback with high sensing performance (*e.g.*, sensitivity, selectivity, stability, response and recovery time (t_{res} and t_{rec}), and so on) is needed.

1.2. Development of Portable Gas Sensing Technologies

Up to now, several types of portable gas sensing technologies are available such as optical, electrochemical (EC), and chemiresitive sensors. Korotcenkov et al. [11] summarized the disadvantages and advantages of these three types of gas sensors (Table 1.1).

Table 1.1 Comparison of three types of gas sensors (e: excellent; g: good; p: poor; b: bad) [11].

Types	Parameters					
	Sensitivity	Selectivity	Response time	Stability	Cost	Portable
Optical	e	e	p	g	p	b
Electrochemical	g	g	p	b	g	p
Chemiresitive	e	p	e	g	e	e

The device with the highest sensitivity and selectivity is achieved by the optical sensors. An infrared (IR) sensor, one type of optical sensor, works by detecting changes of light intensity upon exposure of a target gas (such as greenhouse gases and combustible hydrocarbon gases) [12-14]. The photoionization detector (PID), which is another type of optical sensor, normally uses ultraviolet (UV) to ionize VOCs and generates detectable current signal [15-17]. However, both the IR sensor and PID are expensive which limits the widespread application. The EC sensors are more cost-effective than optical sensors. Generally, the typical EC sensors consist of two functional parts, namely, an electrode system (e.g., two-electrode system (working electrode (WE) and counter electrode (CE)) or three-electrode system (WE, CE and reference electrode (RE))), electrolyte (*e.g.*, solid-state electrolyte and ionic liquid electrolyte) [18-21]. When exposed to the gas pollutants, the gases pass through the protection membrane, which is on the top of the WE and electrolyte, and then react with WE to generate an electrical current. However, the poor stability of the electrolyte and high working temperatures of the EC sensors greatly influence their stability, which leads to a short life-time [11, 21]. For

chemiresistive sensors, gas detection is achieved by detecting changes in the resistance of a semiconductor [22, 23]. Metal oxide semiconductor-based gas sensors are the most popular choice in commercial applications due to their high stability and low cost when selectivity is not critical. The selectivity issue of the chemiresistive gas sensors can be partially addressed by constructing gas sensor arrays, known as an "electronic nose", and combining computational analysis algorithms such as learning vector quantization (LVQ), principal component analysis (PCA), partial least squares (PLS), and so on [24-26].

At the beginning of the 1960s, Seiyama et al. [27] reported the first chemiresistive gas sensor based on ZnO film and this aroused great attention [27, 28]. To date, many chemiresistive gas sensors based on various metal oxides have been developed. Figure 1.1 shows the search results of reported gas sensors based on metal oxides (20603 articles in total) (SnO_2, ZnO, TiO_2, WO_3, In_2O_3, and Fe_2O_3) up to June 14th 2019 [29]. A portion of the research articles are based on p-type metal oxides with a percentage of 11.4%, and NiO is one of the most popular p-type metal oxides in gas sensing (35%). For the n-type metal oxides, SnO_2 (~31.3%) and ZnO (~25.4%) are the most representative gas sensing materials due to their good stability and sensitivity, as summarized in the Figure 1.1. Hence, this project mainly focuses on studying the SnO_2, ZnO, NiO and heterostructural materials based on these metal oxides.

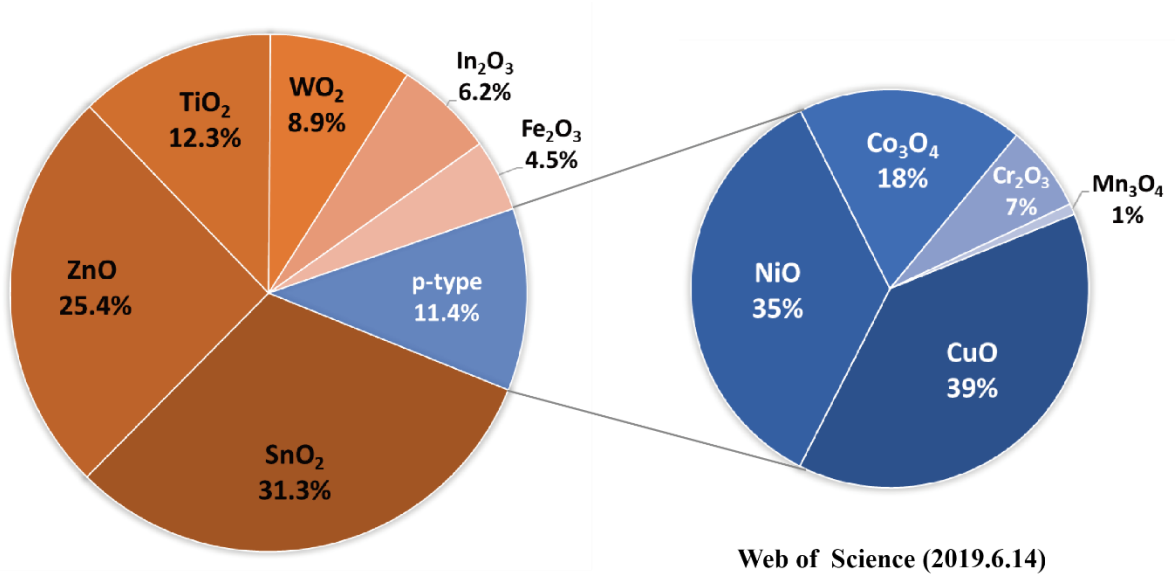

Figure 1.1 Internet search results of web of knowledge on June 14th 2019 about the p-type and n-type metal oxide-based gas sensors.

1.3. Basic Sensing Mechanism of Gas Sensors Based on Metal Oxides

Understanding the sensing mechanism of metal oxide-based gas sensors can provide a guideline for high-performance sensor design. For example, increase of the specific surface area and fabrication of heterostructural materials can be effective approaches. The typical gas sensing mechanism model based on a metal oxide can be explained as follows. First, when the temperature is elevated, the adsorption of oxygen molecules (O_2) from the ambient air on the surface of the metal oxide will withdraw electrons from the metal oxide to form anionic species (such as O_2^- and O^-). Then, an electron-depletion layer (EDL) for a n-type metal oxide or a hole accumulation layer (HAL) for a p-type metal oxide is formed at the surface of the metal oxide [14, 22, 30]. This reaction leads to the conduction band of the metal oxide bending upward at the surface and forming a potential barrier. Second, when exposed to target gases, the adsorption of the target gases on the surface of the metal oxide will react with the formed ionic oxygen species by withdrawing electrons (oxidizing gases) or donating electrons (reducing gases) [31, 32]. The transfer of the electrons between the target gases and metal oxide can

regulate the width of the EDL or HAL [29, 33]. Thus, the overall resistance of the metal oxide-based sensor will change. For example, when exposed to reducing gases, the electrons will transfer from the reducing gases to the n-type metal oxide. As a result, the EDL will shrink, which causes a decrease in resistance, named n-type sensing behavior. In contrast, if a p-type metal oxide is exposed to the reducing gases, the HAL will shrink due to the donated electrons and lead to an increase in resistance, named p-type sensing behavior. The response to the oxidizing gases is opposite to the reducing gases.

However, the sensing mechanism of the chemiresistive sensors is always more complex as it is not only dependent on the properties of the sensing materials (*e.g.*, p-type or n-type semiconductor) but also influenced by various parameters such as grain size, working temperatures, density of defects, and even the exposed crystal facet of the sensing materials [11, 34-40]. For example, Xu et al. [38] studied the effects of crystal diameter (D) of SnO_2 on sensitivity of the sensor. The SnO_2-based sensor reaches the highest sensitivity when the D is comparable with or less than two times of the Debye length (λ_D) of the SnO_2 [38]. Because when the $D \leq 2\lambda_D$, the SnO_2 is completely depleted after absorbing O_2 molecules and then the response to the reducing gases is maximized. The λ_D of the studied metal oxide can be calculated according to the following equation (1-1) [41, 42],

$$\lambda_D = \sqrt{\frac{\varepsilon_{MO} kT}{q^2 N_{MO}}} \qquad (1\text{-}1)$$

where ε_{MO} is the dielectric constant of the studied metal oxide, k is Boltzmann constant, T is the absolute temperature, q is electrical charge of the carrier, and N_{MO} is carrier concentration of the studied metal oxide. The influence of the working temperatures is ascribed to the possible competition between adsorption and desorption rates of the target gases, and the surface reactivity of the adsorbed gas molecules and oxygen species [9, 43]. In addition, the sensing

performance of the metal oxide can also be influenced by the exposed crystal facets due to the different activity [34].

Thus, by tuning the above-mentioned parameters the sensing performance of sensors can be greatly modulated. Miller et al. [44] summarized several of the most likely mechanisms responsible for enhancing the sensing performance (Figure 1.2). Three categories of enhancement mechanism are illustrated, namely, surface-dependent, interface-dependent, and structure-dependent. Among them, the interface-dependent enhancement mechanism is too complicated to cover all the interface interactions by one theory as various heterostructural material-based sensors are available (*e.g.*, n-n heterojunction and p-n heterojunction). Up to now, numerous publications of the chemiresistive sensors based on heterostructural materials are often using an inefficient trail-and-error type approach. Therefore, understanding the sensing mechanism of the heterostructural material-based sensors is essential and can guide researchers for bottom-up design of gas sensors according to their demands. In the following section of this chapter, the basic sensing mechanism of three typical types of device structure based on heterostructural materials will be introduced and discussed.

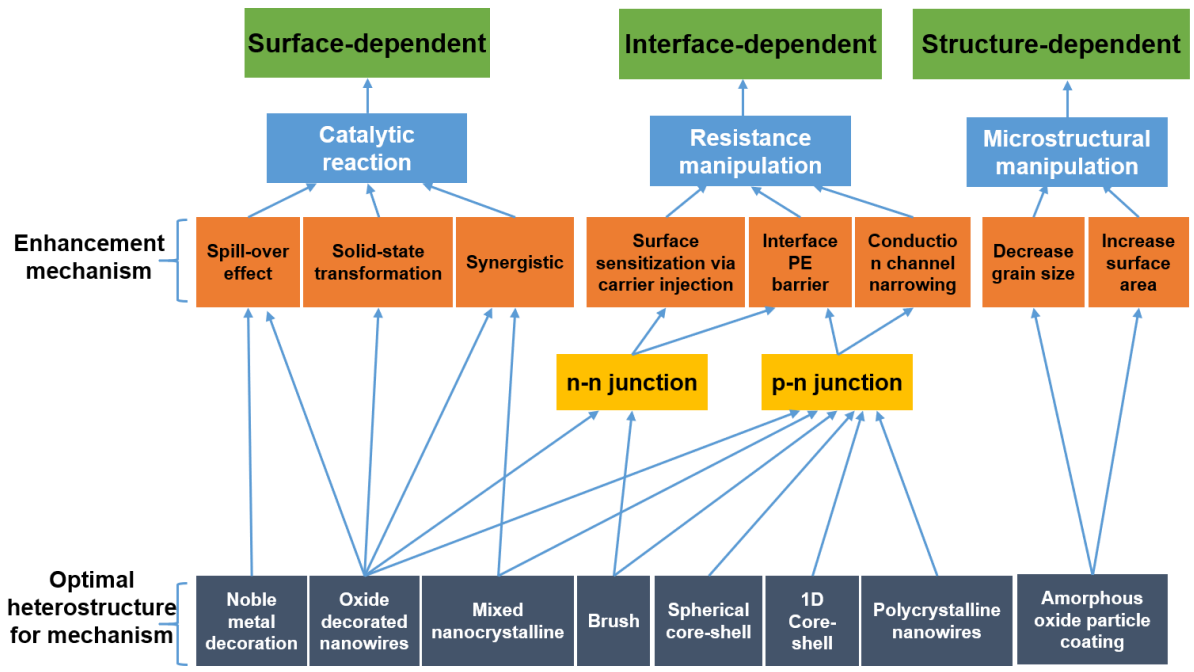

Figure 1.2 Summary of most cited sensor performance enhancing mechanisms and the types of heterostructures that are most optimal for each mechanism type. Some types of mechanisms and structures have been omitted for space [44].

1.4. Typical Sensing Mechanism of Gas Microsensors Based on Heterostructures

As mentioned above, the n-type metal oxides are much more widely used than the p-type metal oxides for gas sensors. So, n-n heterojunction- and p-n heterojunction-based structures are very common. The transfer of charges at the hetero-interface is basically depending on the different Fermi levels (E_f) of the constituents. The electrons will flow from the constituent with a higher E_f to the constituent with a lower E_f at the hetero-interface and vice versa for holes until the Fermi levels reach equilibrium. Then the carriers at the hetero-interface will be depleted and form a depletion layer, which facilitates to tune the conduction channel of the sensors.

Although the heterojunction plays a very important role in gas sensing performance, the device structure of the whole sensors (geometric structure or electronic structure) can also significantly affect the sensing behavior. Here, three typical types of device structure based on

metal oxide heterojunctions are discussed as shown in Figure 1.3: (type-I) two kinds of metal oxide compounds are randomly dispersed between two electrodes; (type-II) heterostructural materials are consisted of two kinds of metal oxides in order and only one kind of the metal oxides connects the electrodes; (type-III) two materials connect to the two electrodes separately and the device is channeled by the formed heterojunction between the two materials.

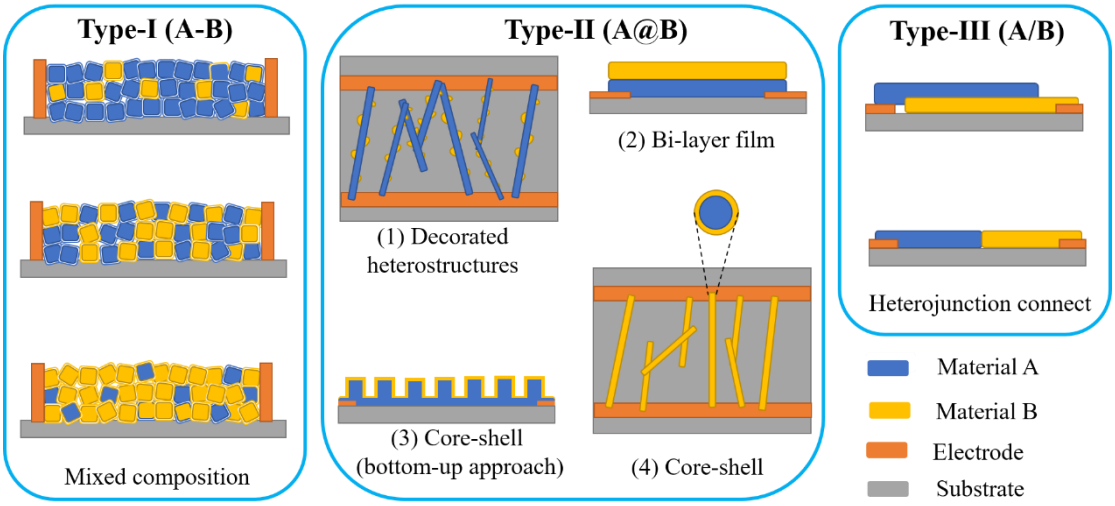

Figure 1.3 Schematic graph of three types of device structure.

● A hyphen between compounds (*e.g.*, "SnO_2–NiO") represents that the two constituents are simply mixed (type-I).

● An "@" between two compounds (*e.g.*, "SnO_2@NiO") represents that the host material (SnO_2) is decorated with NiO which is used in the type-II sensor structure.

● A forward slash (*e.g.*, "NiO/SnO_2") represents the type-III sensor structure and the former material is p-type semiconductor and the later is n-typesemiconductor.

1.4.1. Sensing Mechanism of the Type-I Sensor Structure

For metal oxide composite-based gas sensors, the two kinds of metal oxides are randomly distributed between the electrodes. Many fabrication methods have been developed and reported to obtain the metal oxide composites including sol-gel, co-precipitation, hydrothermal,

and the simplest mechanical mixing method [45-47]. Notably, even though the composition percentage of the metal oxide composites is the same, the sensing performance of the sensors can be quite different with different fabrication processes [48, 49]. For instance, Gao et al. [48] prepared two sensors based on MoO_3-SnO_2 composites using chemical-solution and mechanical mixing methods, respectively. The sensing results demonstrate that even though the MoO_3-SnO_2 composites obtained by the two methods have the same atomic ratio (Mo:Sn; 1:1.9), the sensing performance of the MoO_3-SnO_2 composites prepared by the chemical solution method is much better owing to the stronger interconnection between the MoO_3 and SnO_2.

Generally, the sensing behavior of the metal oxide composites is greatly dependent on which metal oxide acts as the dominating conduction channel of the sensor. Thus, it is very important to determine the dispersal state of the composites such as the percent composition and the nanostructure of the composites. Naik et al. [45] studied the SnO_2-ZnO composites prepared by the mechanical mixing method and varied the percent composition of the ZnO from 0 wt% to 100 wt%. When one constituent dominates in the percentage composition of the composites (*e.g.*, 0.9ZnO-0.1SnO_2 and 0.1ZnO-0.9SnO_2 composites), the conduction channel is determined by the major metal oxide, which is called homojunction conduction channel. When the percentage compositions of two constituents are comparable, the conduction channel is believed to be heterojunction dominated [45, 50]. Yamazoe et al. [51, 52] reported that the hetero-contact regions of two constituents can dramatically enhance the sensitivity of the sensor due to a heterojunction potential barrier. This is because the heterojunction potential barrier, formed owing to different working functions of the constituents, can efficiently tune the drift mobility of electrons when exposed to different ambient gases [51, 52]. Kim et al. [50] further confirmed this conclusion, a series of $xSnO_2$-$(1-x)Co_3O_4$ composite nanofibers were synthesized by an electrospinning method to study the sensing performance. Obviously, the

sensing behavior of sensors based on SnO_2-Co_3O_4 composites transits from the n-type to the p-type sensing behavior by decreasing the SnO_2 percentage (Figure 1.4) [50]. When the major constituent is SnO_2, the sensor shows a typical n-type sensing behavior and then transforms to the p-type sensing behavior when Co_3O_4 dominates. For the 0·5SnO_2-0·5Co_3O_4 (nominal composition), although maximum number of p-n heterojunction exists, the sensor shows the n-type sensing behavior due to the nominal composition. However, compared with homojunctions dominated sensors (*e.g.*, the SnO_2-rich or Co_3O_4-rich cases), the heterojunctions dominated sensor (0·5SnO_2-0·5Co_3O_4-based sensor) shows the highest sensing response to C_6H_6. The high initial resistance of 0·5SnO_2-0·5Co_3O_4-based sensor and the more evident ability to modulate the overall resistance of the sensor caused by the p-n heterojunction both lead to high sensitivity to C_6H_6. Moreover, defects formed at the SnO_2-Co_3O_4 hetero-interfaces, which result from lattice mismatch, can provide preferential adsorption sites for the target gases and oxygen molecules resulting in an enhanced sensing response [48, 53].

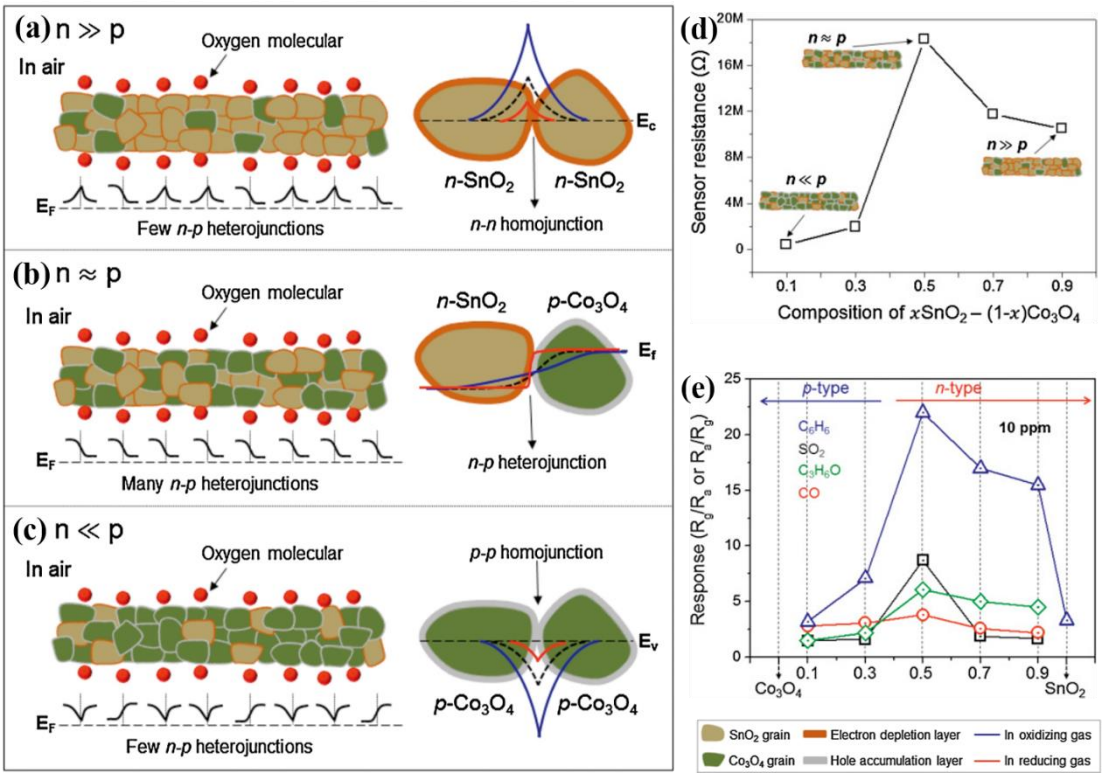

Figure 1.4 Schematic diagram of number of junctions in the three selected compositions; (a) SnO_2-rich composition; (b) $0{\cdot}5SnO_2$-$0{\cdot}5Co_3O_4$ composition; (c) Co_3O_4-rich composition; (d) the sensor resistance of $xSnO_2$-(1-x)Co_3O_4 compositions; (e) sensing response of $xSnO_2$-(1-x)Co_3O_4 compositions sensors to 10 ppm CO, acetone, C_6H_6, and SO_2 gases at 350 ℃ [50].

1.4.2. Mechanism of the Type-II Sensor Structure

The type-II sensor structure is another popular sensor structure and various heterostructural materials are available, which consist of one type of host nanomaterials and a second or even third phase nanomaterials. For instance, one dimensional materials (1D) or 2D materials decorated with nanoparticles, and core-shell (C-S) heterostructures are different heterostructural materials used in the type-II sensor structure. For the first kind of heterostructural materials (decorated heterostructures) as demonstrated in Figure 1.3, the conduction channel of sensor is connected by the host materials, and the modified nanoparticles can provide more reaction sites for adsorption or desorption of gases and can also work as catalysts to enhance the sensing performance [48, 54, 55]. In addition, the formed

heterojunctions between the host material and the nanoparticles can efficiently modulate the conduction channel via a radial modulation mechanism [56]. Figures 1.5a and b demonstrate the sensing performance of pure SnO_2 nanowires and SnO_2@Cr_2O_3 nanowires to the reducing and oxidizing gases [57]. Compared with the pure SnO_2 nanowires, the response of the SnO_2@Cr_2O_3 nanowires to the reducing gases is greatly enhanced whereas it is deteriorated to oxidizing gas. These phenomena are closely related to the local suppression of the conduction channel of the SnO_2 nanowires in radial direction ascribing to the p-n heterojunction [57]. Figures 1.5c and d illustrate the sensing mechanism of the pure SnO_2 nanowires and SnO_2@Cr_2O_3 nanowires. For the pure SnO_2 nanowires, the resistance of the sensor is simply tuned by changing the width of the EDL on the surface of SnO_2 nanowires after exposure to the reducing and oxidizing gases [57]. For the SnO_2@Cr_2O_3 nanowires, as the electrons will flow from SnO_2 to Cr_2O_3 at the hetero-interfaces due to the formed heterojunctions, the initial EDL of the SnO_2 nanowires in the air is expanded and the conduction channel is suppressed compared with the pure SnO_2 nanowires. Thus, when exposed to the reducing gas, captured electrons are released to the SnO_2 nanowires and the EDL dramatically shrinks resulting in a higher sensitivity than the pure SnO_2 nanowires. On the contrary, when switching to oxidizing gas, the expansion of the EDL is marginal, which leads to low sensitivity.

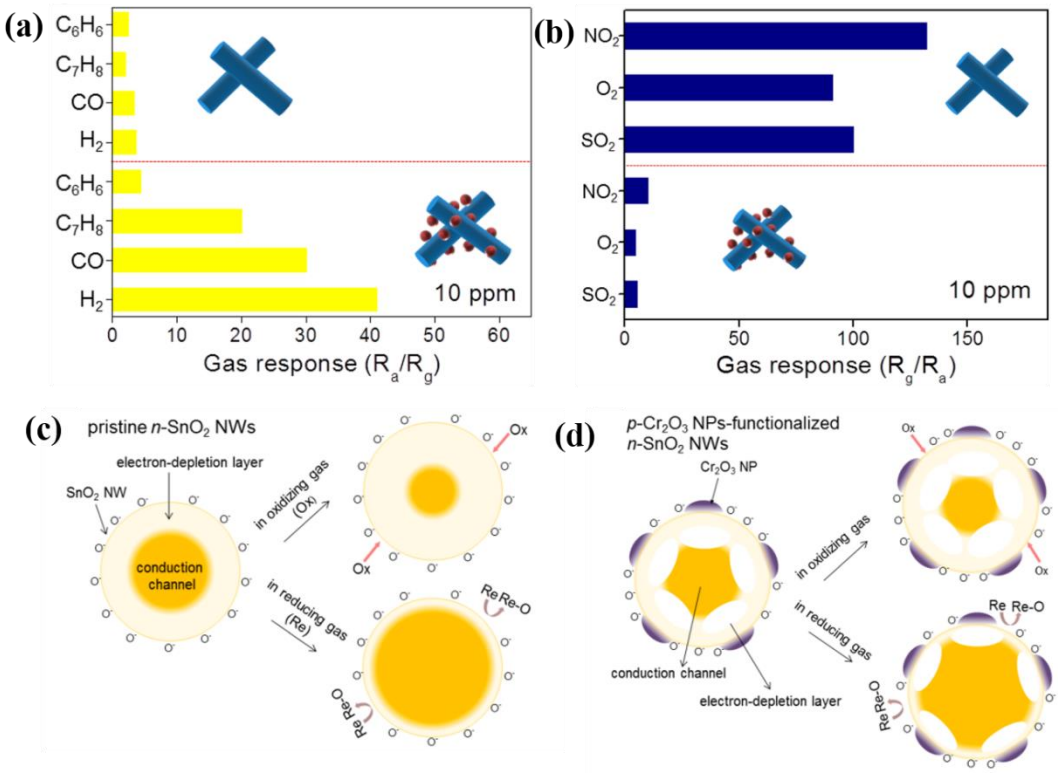

Figure 1.5 Summary of gas response to 10 ppm of reducing gases (a), and oxidizing gases (b) based on pure SnO_2 nanowires and SnO_2@Cr_2O_3 nanowires; Schematic of sensing mechanism based on pure SnO_2 nanowires (c), and SnO_2@Cr_2O_3 nanowires (d), respectively [57].

Bilayer or multi-layer heterostructures are commonly obtained by micro-fabrication techniques such as sputtering and atomic layer deposition (ALD) [37, 58-60]. The thicknesses of the films and the contact areas of the two materials can be well controlled. Therefore, it is much easier to characterize the structure and to study the sensing mechanism than other type-II sensor structures due to the well-defined dimensions and contact area between two films. The conduction channel of the bilayer heterostructure is dominated by the bottom layer which is directly contacting with the electrodes. The heterojunctions formed at the contact regions of the two layers can facilitate modulation of the conductance of the bottom layer. Figures 1.6a and b show the NiO@SnO_2 and WO_3@Ga_2O_3 nanofilms are both prepared via the micro-fabrication processes for ethanol sensing. Obviously, the micro-fabrication approaches demonstrate the feasibility for wafer-scaled fabrication of the gas sensor based on bilayer films

with good reproducibility. However, bilayer film heterostructures generally lead to low sensitivity which can limit their applications owing to low specific surface area and low permeation for gases to reach the heterojunction interface [44].

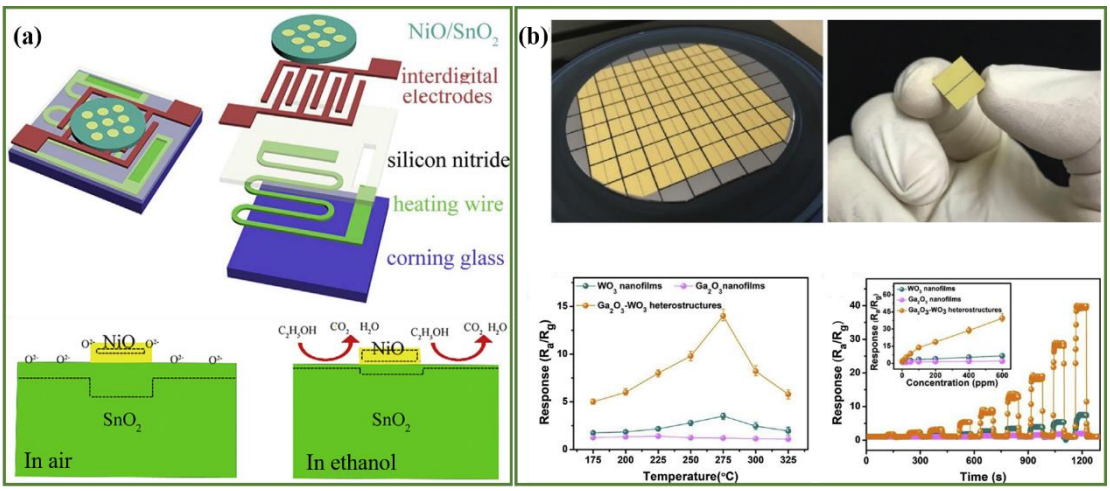

Figure 1.6 (a) NiO@SnO_2 nanofilms for ethanol sensing [61]; (b) WO_3@Ga_2O_3 nanofilms for ethanol sensing [58].

For core-shell (C-S) heterostructures, the sensing mechanism is more complex since the conduction channel is not just confined to the inner of shell. The fabrication routes and the thicknesses of the shell both can determine the location of the conduction channel. For example, the conduction channel is normally confined to the inner of core when using bottom-up approaches to construct C-S heterostructures on the micro-electrode chip [54, 62-65]. Xu et al. [41] reported a bottom-up approach to prepare α-Fe_2O_3@NiO and α-Fe_2O_3@CuO C-S heterostructures by depositing a layer of NiO or CuO nanoparticals on the α-Fe_2O_3 nanorods, in which the conduction channel is confined to the core part (α-Fe_2O_3 nanorods). Liu et al. [64] also successfully confined the conduction channel to the core part of Si@TiO_2 C-S heterostructures by drop-casting TiO_2 sol onto the prepared Si nanowire array. Thus, the sensing behavior (p-type or n-type) of the Si@TiO_2 C-S heterostructure-based sensor is depending on the semiconducting type of the Si nanowires.

However, most reported heterostructural material-based sensors are prepared by transferring synthesized C-S material powders onto a micro-electrode chip. In this case, the conduction channel of the sensor is influenced by the thickness of shell. Kim's group [50, 66-70] studied the effects of shell thickness to the gas sensing performance and proposed a possible sensing mechanism. It is believed that two factors contribute to the sensing mechanism of this structure: (1) the radial modulation of the EDL of the shell and (2) the electric field smearing effect (Figure 1.7). The authors mentioned that the conduction channel of carriers is mostly confined to the shell layer when the shell thickness is thicker than the λ_D of the shell layer [66]. As a result, the resistance modulation of sensors based on C-S heterostructures is mainly dominated by the radial modulation of the EDL of the shell (Figure 1.7a) [66]. However, when the shell thickness is equal to or less than the λ_D of the shell layer, the shell layer would be fully electron-depleted by the adsorbed oxygen species and the formed heterojunction at the C-S hetero-interface. Then the conduction channel is not only located in the inner of shell layer but also partially in the core part, especially when the shell thickness is smaller than the λ_D of the shell layer. In this case, both the fully electron-depleted shell layer and the partial depleted core layer contribute to modulate the resistance of the whole C-S heterostructures, namely an electric-field smearing effect (Figure 1.7b). Some other studies use the concept of volume fraction of the EDL in the whole C-S heterostructures to analyze the effect of the shell thickness instead of the electric field smearing effect [67, 71]. Taking the two contributions into consideration, the overall resistance modulation of the C-S heterostructures reaches the highest when the shell thickness is comparable with the λ_D of the shell layer as shown in the Figure 1.7c. Therefore, the optimal shell thickness may be close to the λ_D, which is consistent with the most publications [41, 66, 68, 71, 72].

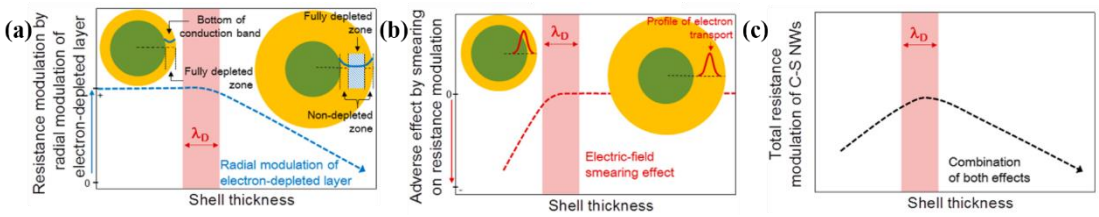

Figure 1.7 Conceptual description showing the dual functional sensing mechanism of C−S NWs: (a) resistance modulation by radial modulation of the electron-depleted shell layer, (b) adverse effect by smearing on resistance modulation, and (c) total resistance modulation of C−S NWs by a combination of both effects [66].

It is worth noting that several publications demonstrated that the shell thickness also can influence the sensing behavior of p-n heterojunction based C-S heterostructures [70, 73]. Lee et al. [70] and Bai et al. [73] studied the influence of the shell thickness to the p-n heterojunction based C-S heterostructures (*e.g.*, CuO@TiO_2 and NiO@ZnO p–n C-S heterostructures) by varying the ALD cycles to the shell thickness. As a result, the sensing behavior of sensors transits from the p-type to the n-type sensing behavior when increasing the shell thickness [70, 73]. Figure 1.8 demonstrates the ethanol sensing mechanism in NiO@ZnO p–n C-S nanotubes with different ZnO ALD cycles [73]. At the beginning (such as ALD cycle of 30), the ZnO shell has not been completely constructed and the model can be viewed as NiO@ZnO decorated heterostructures (Figure 1.8a). Thus, the conduction channel is confined to the NiO matrix and the sensor based on NiO@ZnO shows p-type sensing behavior. When the ALD cycles increase to 50, the ZnO nanoparticles are still discontinuous as shown in Figure 1.8b. In this case, although the conduction channel is still located in the NiO, the effect of the ZnO nanoparticles to the whole gas sensing performance is enhanced. In addition, as the NiO and ZnO are different types of semiconductors, the sensing response of the NiO@ZnO-based sensors decreases when increasing the ALD cycle from 30 to 50. By further increasing the ZnO content (ALD cycle of 70, Figure 1.8c), the ZnO shell becomes quasi-continuous and serves as

the conduction channel, leading to the n-type sensing behavior. But the quasi-continuous shell cannot prevent the NiO from interacting with the ethanol, resulting in a cancellation effect between the NiO and the ZnO and low response. However, when the shell thickness is close to the λ_D of the ZnO, the sensor based on the NiO@ZnO p–n C-S nanotubes reaches the highest sensing response which is consistent with the previous conclusion (Figure 1.8d, e). Similar sensing behavior transitions have also been reported based on branched p-n heterostructures [74, 75]. Zhou et al. [74] studied the sensing behavior of Mn_3O_4@Zn_2SnO_4 branched heterostructures by tuning the content of the Zn_2SnO_4 on the surface of the Mn_3O_4 nanowires. The p-type sensing behavior is observed when just the Zn_2SnO_4 seeds are formed onto the surface of the Mn_3O_4. With further increasing the content of the Zn_2SnO_4, the sensor based on the Mn_3O_4@Zn_2SnO_4 branched heterostructures demonstrates the n-type sensing behavior.

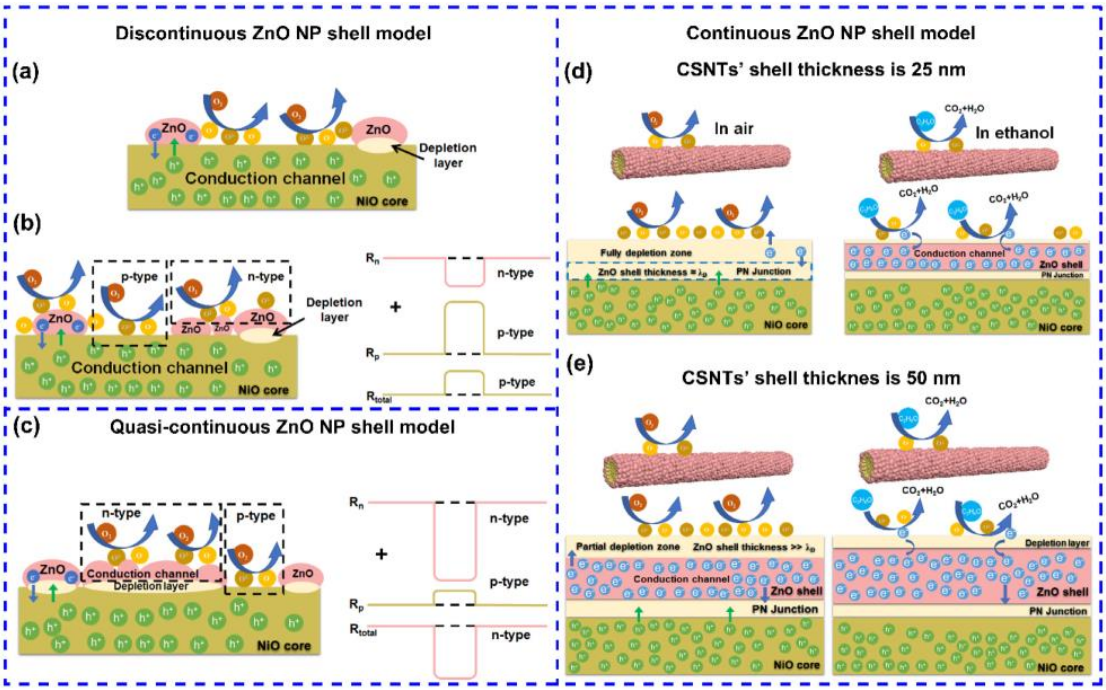

Figure 1.8 Schematic diagram of ethanol sensing mechanisms in NiO@ZnO C-S nanotubes with different ZnO ALD cycles. (a), (b) Discontinuous ZnO nanoparticle shell model. (c) Quasi-continuous ZnO nanoparticle shell model. (d), (e) Continuous ZnO nanoparticle shell model [73].

1.4.3. Sensing Mechanism of the Type-III Sensor Structure

The type-III sensor structure is not very common and the conduction channel is based on the formed heterojunction between the two semiconductors, which are separately connected to the two electrodes. The unique device structure is usually obtained via micro-fabrication techniques. Generally, metal oxide-based gas sensors operate under the principle of conductance change due to the chemisorption of gas molecules onto the surface of sensing materials. However, the sensing mechanism is quite different for the type-III sensor structure.

For example, Kwon et al. [76] proposed a NiO/SnO_2 p-n heterojunction-based gas sensor via an oblique-angle deposition method as shown in Figure 1.9a. The sensor based on NiO/SnO_2 p-n heterojunction shows the same sensing trend to H_2 and NO_2 (Figures 1.9b and c). Because the total current of p-n heterojunction is determined both by the changes of the carrier concentrations and the heterojunction barrier height according to equations (1-2) and (1-3), which represent the hole diffusion current density and electron diffusion current density [77]:

$$J_p = \frac{qD_p}{L_p} p_{p0} exp\left(\frac{-qV_{bi}^0}{kT}\right) \exp\left(\frac{-\Delta E_v}{kT}\right)\left[\exp\left(\frac{qV_a}{kT}\right) - 1\right] \quad (1\text{-}2)$$

$$J_n = \frac{qD_n}{L_n} n_{n0} exp\left(\frac{-qV_{bi}^0}{kT}\right) \exp\left(\frac{-\Delta E_c}{kT}\right)\left[\exp\left(\frac{qV_a}{kT}\right) - 1\right] \quad (1\text{-}3)$$

where n_{n0}, and p_{p0} are electron (hole) concentration in n-type (p-type) metal oxides, V_{bi}^0 is built-in potential, D_p (D_n) is diffusion coefficient for electron (hole), L_n (L_p) is diffusion length for electron (hole), ΔE_v (ΔE_c) is difference value of valence band (conduction band) at hetero-interface, respectively, V_a is the bias voltage. Based on the equations (1-2) and (1-3), although the current density is proportional to carrier density, it is inversely exponential changing to the V_{bi}^0. Thus, the overall change in the current density is significantly dependent on modulation of the heterojunction barrier height. To address the similar sensing trend to NO_2 and H_2 of

NiO/SnO_2-based sensor, Kwon et al. [76] systematically studied the ability of NO_2 and H_2 to change the carrier concentration and modulate the V_{bi}^0 via I-V characterization and computational simulation. When exposed to H_2, the increase of the electron concentration leads to the increase of the J_n and the slight change of the V_{bi}^0 leads to low response. When exposed to NO_2, the dramatical decrease of the electron concentration in the SnO_2 and small increase of the hole concentration in the NiO both lead to the V_{bi}^0 greatly decreasing and ensure high forward response [76].

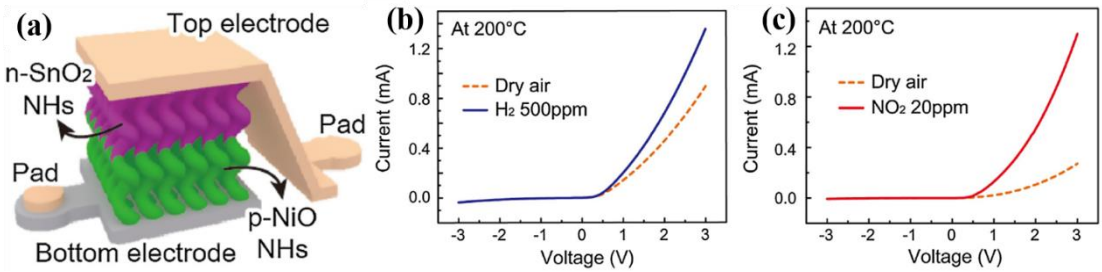

Figure 1.9 (a) Schematic drawings of the p-NiO/n-SnO_2 nanohelixes; (b) H_2 and (c) NO_2 sensing properties of the p-NiO/n-SnO_2 nanohelixes heterojunction sensor at 200 °C [76].

In addition, the build-in electric field (BEF) at the hetero-interface, resulting from the difference in Fermi levels of the materials, can contribute to the separation of electron-hole pairs. The p-n heterojunction structure is commonly utilized to construct photovoltaic devices owing to the existence of the BEF and even shows the potential to fabricate photovoltaic room temperature self-powered gas sensors under light illumination [78-82]. The light illumination can enhance charge exchange between the sensing material and adsorbed gas species due to photodissociation of chemisorbed gas species [78, 79]. The merit of the photovoltaic self-powered gas sensor is extremely low energy consumption as it can absorb the energy from illuminated light and then drive itself or other miniaturized device without external energy sources. For instance, Tanuma et al. [83] fabricated NiO/ZnO p-n heterojunction to work as a solar cell to activate polycrystalline SnO_2-based sensor for CO_2 sensing through conductance

changing theory. On the other hand, the sensing mechanism of a photovoltaic self-powered gas sensor based on p-n heterojunction also mainly relies on modulation of the heterojunction barrier height. Gad et al. [80] reported a photovoltaic self-powered gas sensor based on a Si/ZnO@CdS p-n heterojunction as demonstrated in Figure 1.10a. Vertically aligned ZnO nanowires are directly grown on the p-type Si substrate to form Si/ZnO p-n heterojunction after depositing a layer of ZnO seeds. Then CdS nanoparticles are decorated on the surface of the ZnO nanowires via chemical surface modification. Under light illumination, an open-circuit voltage (V_{oc}), which is induced by the separation of electron-hole pairs under the BEF at the hetero-interface of the Si/ZnO, linearly increases with the number of connect diodes (Figure 1.10b) [80, 82]. The V_{oc} is expressed by Equation (1-4) [77],

$$V_{oc} = \frac{kT}{q} \ln\left(\frac{N_D^{ZnO} N_A^{Si}}{N_i^{ZnO} N_i^{Si}}\right) \tag{1-4}$$

where N_D, N_A, and N_i are the concentrations of the donor, acceptor, and intrinsic carrier, k, T, and q represent the same parameters as in previous equations.

The oxidizing gases withdraw electrons from the ZnO nanowires, which causes a decrease of the N_D^{ZnO}, as a result the V_{oc} decreases. In contrast, the reducing gases lead to an increase in V_{oc} (Figure 1.10c). Moreover, the photoexcited electrons in the CdS nanoparticles are injected into the conduction band of ZnO under light illumination to interact with adsorbed gases. Then the sensing response is enhanced compared with pure Si/ZnO p-n heterojunction [80, 81]. Hoffmann et al. [81, 82] reported another similar photovoltaic self-powered gas sensor as displayed in Figure 1.10d. It is worth noting that by modulating the working function of target gases via modification of the ZnO nanowires with amine ([3-(2-aminoethylamino) propyl] trimethoxylsilane) (amine functionalized-SAM) and thiol ((3-mercapto-propyl)-trimethoxysilane) (thiol functionalized-SAM), the sensor can selectively detect NO_2 [80 82]. Moreover, Liu et al. [79, 84] successfully fabricated another kind of photovoltaic self-powered

NH_3 sensor by utilizing a special asymmetric light illumination method. Briefly, S-hyperdoped or Se-hyperdoped Si are partially covered to mimic the electronic structure of heterojunction when under light illumination based on the Dember effect [84,85]. Due to the asymmetric light illumination, the carrier concentration of exposed area is much larger than covered area owing to photoexcited electrons and holes. Thus, the photogenerated carriers diffuse from the exposed area to the covered area to produce a photocurrent attributed to the different mobilities of electrons and holes [79, 84].

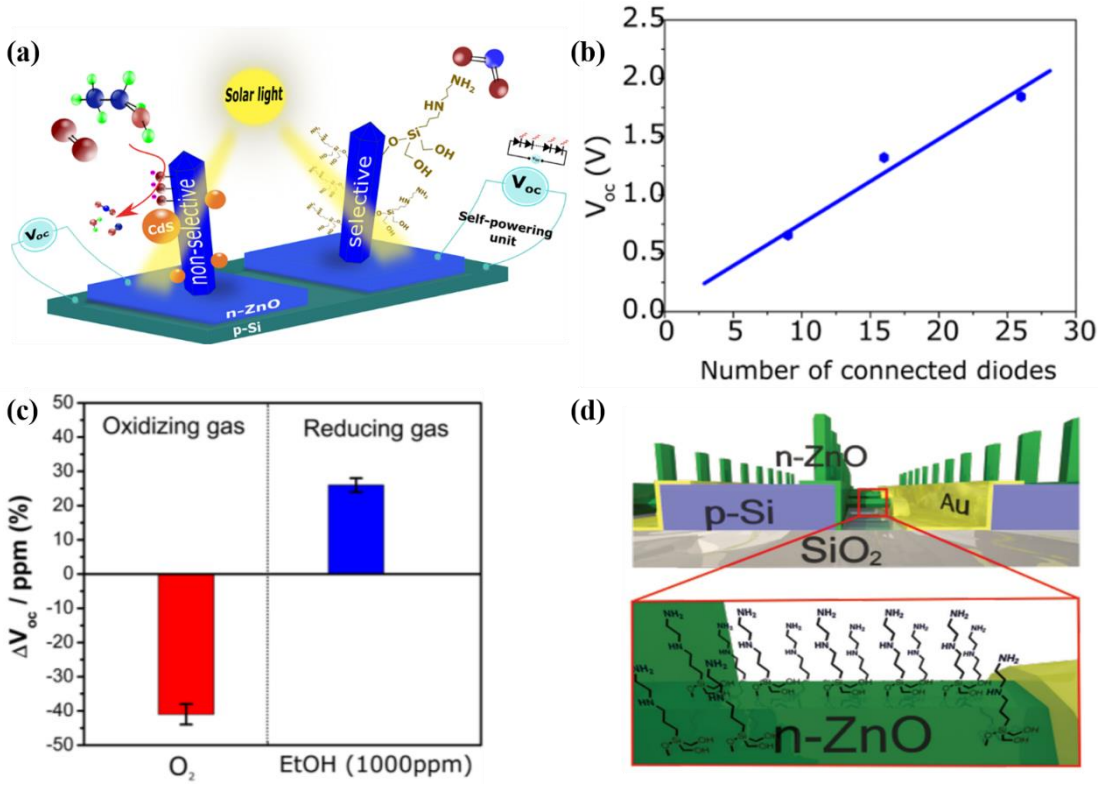

Figure 1.10 (a), (d) Schematic pictures of photovoltaic self-powered gas sensors based on Si/ZnO p-n heterojunction; (b) Linear relation between measured V_{oc} and the number of diodes under illumination; (c) Self-powered sensing responses of sensor toward oxidizing (O_2) and reducing (1000 ppm ethanol) gases under solar illumination [80, 82].

1.5. Remaining Challenges

Based on the above literature review, a lot of different metal oxide-based heterostructures have been developed to enhance the sensing performance. However, there are some drawbacks and challenges in metal oxide-based gas sensors that need to be addressed, such as reproducibility, long-term stability, wafer-scale fabrication, and power consumption. Reproducibility in performance between two sensors prepared via identical fabrication methods is seldom reported and is very important in wafer-scale fabrication of devices. In addition, wafer-scale fabrication of gas sensor array is much more challenging when multiple metal oxide components are involved since the fabrication methods should be able to precisely control the location and structure of the heterostructural materials. Spin- and dip-coating methods are the common low-cost routes to connect sensing materials with micro-electrode chips. However, the sensing materials are easily aggregated, interconnections between the sensing materials and the micro-electrode chips are weak, and the obtained sensing material patterns are inhomogeneous. Thus, the sensitivity and stability of sensors prepared by spin- or dip-coating methods are significantly influenced and the performance reproducibility is poor. Although some micro-fabrication methods are utilized for constructing planner sensing material to ensure the reproducibility, these methods are expensive and the sensitivity of sensors based on planar films is rather poor compared with 3D nanostructured materials. Therefore, novel cost-effective strategies are needed, which are compatible with the micro-fabrication process of micro-electrode chips, to implement wafer-scale fabrication of sensors with high reproducibility and sensitivity. In addition, it is possible to fabricate photovoltaic self-powered gas sensors based on p-n heterojunction to reduce power consumption. However, the reported fabrication process is rather complicated and the sensitivity is much lower than traditional metal oxide-based chemiresistive gas sensor. Therefore, self-powered gas sensors with high performance are still a long way off.

1.6. Research Aims and Objectives

In this project, I aimed to develop high-performance gas microsensors by designing heterostructural nanomaterials, device structures and novel fabrication strategies to address the above-mentioned challenges. In order to ensure the stability, in-situ growth ('bottom-up' strategy) of hierarchical heterostructural materials was proposed to enhance the interconnection between sensing materials and micro-electrode chips. The uniformity and reproducibility were also addressed by integrating micro-fabrication techniques ('top-down' strategy) with 'bottom-up' strategies for wafer-scale fabrication of gas sensors. Inspired by the photovoltaic properties of p-n heterojunction, a self-powered gas sensor was studied for sake of reducing energy consumption. The following work aims to tackle these problems and study the sensing mechanism as it varies with the materials properties, device structures (geometric structure or electronic structure), operating modes (voltage, current, resistance, or capacitance), operating conditions (temperature, humidity, or light illumination), and so forth.

Chapter 2: Design of Novel ZnO@SnO_2 n-n Heterostructures for Highly Sensitive NO_2 Sensing

Metal oxides have received great attention in the field of gas sensors due to their chemical and thermal stability. However, using pure metal oxides (*e.g.*, ZnO, SnO_2) as sensing material have some problems such as low sensitivity, poor selectivity as well as slow response-recovery times. Consequently, design and synthesis of ZnO@SnO_2 composites with novel architectures is a potential approach to enhance the sensing performance and achieve ppb level detection limits for NO_2. In this chapter, we mainly focus on addressing the following questions. *What is the growth mechanism of ZnO@SnO_2 n-n hierarchical nanostructures (HNSs)? How does the sensing performance of the ZnO@SnO_2 HNS-based sensor compare with that of pure ZnO- and pure SnO_2-based sensors? What is the sensing mechanism of the SnO_2@ZnO HNSs?*

Chapter 3: In situ Growth of NiO@SnO_2 p-n Heterostructures for High Performance H_2S Sensing

Until now, most reported gas sensors based on heterostructural materials are manufactured by slurry-coating or screen-printing the sensing material onto a micro-electrode chip as displayed in Chapter 2. However, these methods may affect the sensitivity, stability, and reproducibility of the sensors. First, the sensing materials easily aggregate during the slurry and printing processes, which can significantly reduce the specific surface area of the sensing materials and lead to low sensitivity. Second, the relatively poor interconnection between the sensing materials and electrodes can affect the long-term stability of the sensors for practical application. Moreover, the reproducibility of the sensors is not controllable due to the inhomogeneity of the sensing materials. Therefore, a cost-effective in situ growth method to directly grow high uniform heterostructural materials without adding any binders and surfactants is demanded. In this chapter, we addressed the following problems. *How can in situ growth of NiO@SnO_2 HNSs on the micro-electrode chip be implemented? What are the growth and sensing mechanisms?*

Chapter 4: In situ Growth of Patterned NiO Nanowalls for Wafer-scaled Miniaturized Gas Sensors Design and Fabrication

In situ growth method is an efficient way to strength interconnection between materials and sensors chips and ensure the high uniformity of sensing materials as reported in Chapter 3. The high uniformity of materials is a precondition to obtain high reproducibility of sensing performance among sensors. However, as the sensing materials are fully covered on ceramic chips including electrode wires, the electric contact between sensors and test system are significantly influenced by the next manual welding process. As a result, the sensing performance variation between sensors was not studied in Chapter 3 and the performance

reproducibility of sensors in wafer-scale fabrication is still challenging. Hence, in Chapter 4, a 'top-down' and 'bottom-up' combined strategy was proposed to form patterned materials at specific locations of micro-hot plate wafer without contamination of electrodes. It is a potential strategy for manufacturing miniaturized gas sensors with high-throughput and high reproducibility. *In this Chapter, I aim to tackle two main technological hurdles for low-cost wafer-scale fabrication, namely, how to form patterned microscale sensing materials at specific locations of micro-electrode chips and how to rationally integrate patterning methods with the micro electro mechanical system (MEMS) technique ("top-down" strategy).*

Chapter 5: Design of Photovoltatic Self-Powered Gas Sensor Based on Single-Walled Carbon Nanotubes/Si p-n Heterojunction

Up to now, chemiresistive, field-effect-transistive, and capacitive gas sensors have become available, but all of them are driven by applying a considerable source-drain bias (V_{ds}) to drive the sensor. For the most of metal oxide-based chemiresistive sensors, external power source is demanded to provide high working temperature. Therefore, developing self-powered devices has attracted considerable attention. Compared with conventional semiconductor-based gas sensors, self-powered sensors could dramatically reduce power consumption as well as required space for integration. Inspired by the photovoltaic properties of p-n heterojunction, in this Chapter, the following questions were addressed. *Is it possible to develop a self-powered gas sensor based on p-n SWNTs/Si heterojunction which can be driven by visible light? What's the sensing mechanism of self-powered gas sensor based on p-n heterojunction?*

1.7. References

[1] H. Jing, X. Gao, L. Xu, H. Lin, Z. Zhang, H_2S promotes a glycometabolism disorder by disturbing the Th1/Th2 balance during LPS-induced inflammation in the skeletal muscles of chickens, Chemosphere, 222(2019) 124-131.

[2] G. Wang, S. Bai, J.M. Ogden, Identifying contributions of on-road motor vehicles to urban air pollution using travel demand model data, Transport. Res. D-Tr. 14(2009) 168-179.

[3] F. Bao, M. Li, Y. Zhang, C. Chen, J. Zhao, Photochemical Aging of Beijing Urban PM2.5: HONO Production, Environ. Sci. Technol. 52(2018) 6309-6316.

[4] S.C. Lee, S.Y. Kim, B.W. Hwang, S.Y. Jung, D. Ragupathy, I.S. Son, D.D. Leem, J.C. Kim, Improvement of H_2S sensing properties of SnO_2-based thick film gas sensors promoted with MoO_3 and NiO, Sensors, 13(2013) 3889-3901.

[5] Y. Zhu, Y. Zhan, B. Wang, Z. Li, Y. Qin, K. Zhang, Spatiotemporally mapping of the relationship between NO_2 pollution and urbanization for a megacity in Southwest China during 2005-2016, Chemosphere, 220(2019) 155-162.

[6] N.N. Hansel, P.N. Breysse, M.C. McCormack, E.C. Matsui, J. Curtin-Brosnan, D.L. Williams, J.L. Moore, J.L. Cuhran, G.B. Diette, A longitudinal study of indoor nitrogen dioxide levels and respiratory symptoms in inner-city children with asthma, Environ. Health Perspect. 116(2008) 1428-1432.

[7] G.A. Wellenius, T.F. Bateson, M.A. Mittleman, J. Schwartz, Particulate Air Pollution and the Rate of Hospitalization for Congestive Heart Failure among Medicare Beneficiaries in Pittsburgh, Pennsylvania, Am. J. Epidemiol. 161(2005) 1030-1036.

[8] E.G. Elliott, P. Trinh, X. Ma, B.P. Leaderer, M.H. Ward, N.C. Deziel, Unconventional oil and gas development and risk of childhood leukemia: Assessing the evidence, Sci. Total. Environ. 576(2017) 138-147.

[9] T. Yu, X. Cheng, X. Zhang, L. Sui, Y. Xu, S. Gao, H. Zhao, L. Huo, Highly sensitive H_2S

detection sensors at low temperature based on hierarchically structured NiO porous nanowall arrays, J. Mate. Chem. A 3(2015) 11991-11999.

[10] Start of Global air 2018, (2018), https://www.stateofglobalair.org/sites/default/files/soga-2018-report.pdf.

[11] G. Korotcenkov, Metal oxides for solid-state gas sensors: What determines our choice?, Mater. Sci. Eng. B 139(2007) 1-23.

[12] Marianah Masrie, Ramli Adnan, A. Ahmad, A Hybrid Gas Sensor based on Infrared Absorption for Indoor Air Quality Monitoring, Proceedings of the World Congress on Engineering 2(2012).

[13] P. Werle，, F. Slemr，, Karl Maurer, R. Kormann，, Robert M.uckec, B. J.anker, Near- and mid-infrared laser-optical sensors for gas analysis, Opt. Lasers Eng. 37(2002) 101-114.

[14] A. Dey, Semiconductor metal oxide gas sensors: A review, Mater. Sci. Eng. B 229(2018) 206-217.

[15] S. Narayanan, G. Rice, M. Agah, A micro-discharge photoionization detector for micro-gas chromatography, Microchim. Acta 181(2013) 493-499.

[16] C.M. Zimmer, K.T. Kallis, F.J. Giebel, Micro-structured electron accelerator for the mobile gas ionization sensor technology, Journal of Sensors and Sensor Systems, 4(2015) 151-157.

[17] L. Liu, Q. Tan, Chenyan Xue, J. Xiong, Design of a Gas Sensor for Hydrazines Based on Photo-ionization Principle, Appl. Mech. Mater. 44(2011) 2050-2054.

[18] S.S. SebtAhmadi, M.S. Yaghmaee, B. Raissi, R. Riahifar, M. Javaheri, General modeling and experimental observation of size dependence surface activity on the example of Pt nano-particles in electrochemical CO gas sensors, Sens. Actuators B Chem. 285(2019) 310-316.

[19] J. Gębicki, A. Kloskowski, W. Chrzanowski, Prototype of electrochemical sensor for measurements of volatile organic compounds in gases, Sens. Actuators B Chem. 177(2013)

1173-1179.

[20] M. Dosi, I. Lau, Y. Zhuang, D.S.A. Simakov, M.W. Fowler, M.A. Pope, Ultrasensitive Electrochemical Methane Sensors Based on Solid Polymer Electrolyte-Infused Laser-Induced Graphene, ACS Appl. Mater. Interfaces, 11(2019) 6166-6173.

[21] M. Struzik, I. Garbayo, R. Pfenninger, J.L.M. Rupp, A Simple and Fast Electrochemical CO_2 Sensor Based on $Li_7La_3Zr_2O_{12}$ for Environmental Monitoring, Adv. Mater. 30(2018) e1804098.

[22] M. Yang, X. Cheng, X. Zhang, W. Liu, C. Huang, Y. Xu, S. Gao, H. Zhao, L. Huo, Preparation of highly crystalline NiO meshed nanowalls via ammonia volatilization liquid deposition for H_2S detection, J. Colloid. Interface. Sci. 540(2019) 39-50.

[23] Y. Zhang, D. Li, L. Qin, P. Zhao, F. Liu, X. Chuai, P. Sun, X. Liang, Y. Gao, Y. Sun, G. Lu, Preparation and gas sensing properties of hierarchical leaf-like SnO_2 materials, Sens. Actuators B Chem. 255(2018) 2944-51.

[24] B. Zhang, P. Gao, Metal Oxide Nanoarrays for Chemical Sensing: A Review of Fabrication Methods, Sensing Modes, and Their Inter-correlations, Frontiers in Materials, 6(2019).

[25] J. Chen, Z. Chen, F. Boussaid, D. Zhang, X. Pan, H. Zhao, A. Bermak, C.Y. Tsui, X. Wang, Z. Fan, Ultra-Low-Power Smart Electronic Nose System Based on Three-Dimensional Tin Oxide Nanotube Arrays, ACS Nano (2018).

[26] W. Hu, L. Wan, Y. Jian, C. Ren, K. Jin, X. Su, X. Bai, H. Haick, M. Yao, W. Wu, Electronic Noses: From Advanced Materials to Sensors Aided with Data Processing, Adv. Mater. Technol. (2018) 1800488.

[27] T. Seiyama, A. Kato, K. Fujishi, M. Nagatani, A New Detector for Gaseous Components Using Semiconductive Thin Films, Anal. Chem. 34(1962) 1502.

[28] G. Neri, First Fifty Years of Chemoresistive Gas Sensors, Chemosensors, 3(2015) 1-20.

[29] H.J. Kim, J.H. Lee, Highly sensitive and selective gas sensors using p-type oxide

semiconductors: Overview, Sens. Actuators B Chem. 192(2014) 607-627.

[30] N. Barsan, D. Koziej, U. Weimar, Metal oxide-based gas sensor research: How to?, Sens. Actuators B Chem. 121(2007) 18-35.

[31] M. Batzill, U. Diebold, The surface and materials science of tin oxide, Prog. Surf. Sci. 79(2005) 47-154.

[32] J.H. Lee, Gas sensors using hierarchical and hollow oxide nanostructures: Overview, Sens. Actuators B Chem. 140(2009) 319-336.

[33] E. Comini, G. Faglia, G. Sberveglieri, Z. Pan, Z. Wang, Stable and highly sensitive gas sensors based on semiconducting oxide nanobelts, Appl. Phys. Lett. 81(2002) 1869-1871.

[34] B. Wang, J. Nisar, R. Ahuja, Molecular simulation for gas adsorption at NiO (100) surface, ACS Appl. Mater. Interfaces 4(2012) 5691-5697.

[35] T. Kida, S. Fujiyama, K. Suematsu, M. Yuasa, K. Shimanoe, Pore and Particle Size Control of Gas Sensing Films Using SnO2 Nanoparticles Synthesized by Seed-Mediated Growth: Design of Highly Sensitive Gas Sensors, J. Phys. Chem. C 117(2013) 17574-17582.

[36] P.M. Bulemo, H.J. Cho, D.H. Kim, I.D. Kim, Facile Synthesis of Pt-Functionalized Meso/Macroporous SnO_2 Hollow Spheres through in Situ Templating with SiO2 for H2S Sensors, ACS Appl. Mater. Interfaces 10(2018) 18183-18191.

[37] Y. Wang, C. Liu, Z. Wang, Z. Song, X. Zhou, N. Han, et al., Sputtered SnO2:NiO thin films on self-assembled Au nanoparticle arrays for MEMS compatible NO2 gas sensors, Sens. Actuators B Chem. 278(2019) 28-38.

[38] Chaonan Xu, Jun Tamaki, Norio Miura, N. Yamazoe, Grain size effects on gas sensitivity of porous SnO_2-based elements, Sens. Actuators B Chem. 3(1991) 147-155.

[39] S. Cui, H. Pu, E.C. Mattson, Z. Wen, J. Chang, Y. Hou, J. Chen, Ultrasensitive chemical sensing through facile tuning defects and functional groups in reduced graphene oxide, Anal. Chem. 86(2014) 7516-7522.

[40] N. Bandara, C. Jayathilaka, D. Dissanayaka, S. Jayanetti, Temperature Effects on Gas Sensing Properties of Electrodeposited Chlorine Doped and Undoped n-Type Cuprous Oxide Thin Films, J. Sensor Technol. 04(2014) 119-126.

[41] Q. Xu, Z. Zhang, X. Song, S. Yuan, Z. Qiu, H. Xu, B. Cao, Improving the triethylamine sensing performance based on debye length: A case study on α-Fe_2O_3@NiO(CuO) core-shell nanorods sensor working at near room-temperature, Sens. Actuators B Chem. 245(2017) 375-385.

[42] W. Chen, G. Qin, L. Zhou, W. Wu, J. Zou, M. Xu, J. Peng, A physics-based model of flat-band capacitance for metal oxide thin-film transistors, AIP Adv. 8(2018) 065319.

[43] G.J. Sun, H. Kheel, J.K. Lee, S. Choi, S. Lee, C. Lee, H2S gas sensing properties of Fe_2O_3 nanoparticle-decorated NiO nanoplate sensors, Surf. Coat. Technol. 307(2016) 1088-1095.

[44] D.R. Miller, S.A. Akbar, P.A. Morris, Nanoscale metal oxide-based heterojunctions for gas sensing: A review, Sens. Actuators B Chem. 204(2014) 250-272.

[45] A. Naik, I. Parkin, R. Binions, Gas Sensing Studies of an n-n Hetero-Junction Array Based on SnO_2 and ZnO Composites, Chemosensors, 4(2016) 3.

[46] B. Li, J. Liu, Q. Liu, R. Chen, H. Zhang, J. Yu, et al., Core-shell structure of ZnO/Co_3O_4 composites derived from bimetallic-organic frameworks with superior sensing performance for ethanol gas, Appl. Surf. Sci. 475(2019) 700-709.

[47] S. Mulmi, V. Thangadurai, Semiconducting SnO_2-TiO_2 (S-T) composites for detection of SO_2 gas, Ionics 22(2016) 1927-1935.

[48] X. Gao, Q. Ouyang, C. Zhu, X. Zhang, Y. Chen, Porous MoO_3/SnO_2 Nanoflakes with n–n Junctions for Sensing H_2S, ACS Appl. Nano Mater. 2(2019) 2418-2425.

[49] D. Shaposhnik, R. Pavelko, E. Llobet, F. Gispert-Guirado, X. Vilanova, Hydrogen sensors on the basis of SnO_2–TiO_2 systems, Sens. Actuators B Chem.174(2012) 527-534.

[50] J.H. Kim, J.H. Lee, A. Mirzaei, H.W. Kim, S.S. Kim, Optimization and gas sensing

mechanism of n-SnO_2-p-Co_3O_4 composite nanofibers, Sens. Actuators B Chem. 248(2017) 500-511.

[51] N. Yamazoe, K. Shimanoe, Basic approach to the transducer function of oxide semiconductor gas sensors, Sens. Actuators B Chem. 160(2011) 1352-1362.

[52] N. Yamazoe, K. Shimanoe, Proposal of contact potential promoted oxide semiconductor gas sensor, Sens. Actuators B Chem. 187(2013) 162-167.

[53] J.W. Yoon, Y.J. Hong, G.D. Park, S.J. Hwang, F.A. Hady, A.A. Wazzan, Y.C. Kang, J.H. Lee, Kilogram-scale synthesis of Pd-loaded quintupleshelled Co_3O_4 microreactors and their application to ultrasensitive and ultraselective detection of methylbenzenes, ACS Appl. Mater. Interfaces 7(2015) 7717-7723.

[54] D.X. Ju, H.Y. Xu, Z.W. Qiu, Z.C. Zhang, Q. Xu, J. Zhang, J. Wang, B. Cao, Near Room Temperature, Fast-Response, and Highly Sensitive Triethylamine Sensor Assembled with Au-Loaded ZnO/SnO(2) Core-Shell Nanorods on Flat Alumina Substrates, ACS Appl. Mater. Interfaces 7(2015) 19163-19171.

[55] K. Suematsu, K. Watanabe, A. Tou, Y. Sun, K. Shimanoe, Ultraselective Toluene-Gas Sensor: Nanosized Gold Loaded on Zinc Oxide Nanoparticles, Anal. Chem. 90(2018) 1959-1966.

[56] Y. Wang, A. Maity, X. Sui, H. Pu, S. Mao, N.K. Singh, J. Chen, In Operando Impedance Spectroscopic Analysis on NiO–WO_3 Nanorod Heterojunction Random Networks for Room-Temperature H_2S Detection, ACS Omega, 3(2018) 18685-18693.

[57] S.W. Choi, A. Katoch, J.H. Kim, S.S. Kim, Prominent reducing gas-sensing performances of n-SnO_2 nanowires by local creation of p-n heterojunctions by functionalization with p-Cr_2O_3 nanoparticles, ACS Appl. Mater. Interfaces 6(2014) 17723-17729.

[58] Z. Wei, M.K. Akbari, Z. Hai, R.K. Ramachandran, C. Detavernier, F. Verpoort, E. Kats, H. Xu, J. Hu, S. Zhuiykov, Ultra-thin sub-10 nm Ga_2O_3-WO_3 heterostructures developed by

atomic layer deposition for sensitive and selective C_2H_5OH detection on ppm level, Sens. Actuators B Chem. 287(2019) 147-156.

[59] D. Zappa, V. Galstyan, N. Kaur, H.M.M. Munasinghe Arachchige, O. Sisman, E. Comini, "Metal oxide -based heterostructures for gas sensors"- A review, Anal. Chim. Acta 1039(2018) 1-23.

[60] W. Maziarz, TiO_2/SnO_2 and TiO_2/CuO thin film nano-heterostructures as gas sensors, Appl. Surf. Sci. 480(2019) 361-370.

[61] J. Fang, Y. Zhu, D. Wu, C. Zhang, S. Xu, D. Xiong, P. Yang, L. Wang, P.K.Chu, Gas sensing properties of NiO/SnO_2 heterojunction thin film, Sens. Actuators B Chem. 252(2017) 1163-1168.

[62] A. Saravanan, B.R. Huang, D. Kathiravan, A. Prasannan, Natural Biowaste-Cocoon-Derived Granular Activated Carbon-Coated ZnO Nanorods: A Simple Route To Synthesizing a Core-Shell Structure and Its Highly Enhanced UV and Hydrogen Sensing Properties, ACS Appl. Mater. Interfaces 9(2017) 39771-80.

[63] J. Cao, Z. Wang, R. Wang, S. Liu, T. Fei, L. Wang, T. Zhang, Core–shell $Co_3O_4/\alpha\text{-}Fe_2O_3$ heterostructure nanofibers with enhanced gas sensing properties, RSC Adv. 5(2015) 36340-6.

[64] D. Liu, L. Lin, Q. Chen, H. Zhou, J. Wu, Low Power Consumption Gas Sensor Created from Silicon Nanowires/TiO_2 Core-Shell Heterojunctions, ACS Sens. 2(2017) 1491-7.

[65] F. Li, X. Gao, R. Wang, T. Zhang, Design of WO_3-SnO_2 core-shell nanofibers and their enhanced gas sensing performance based on different work function, Appl. Surf. Sci. 442(2018) 30-37.

[66] S.W. Choi, A. Katoch, G.J. Sun, J.H. Kim, S.H. Kim, S.S. Kim, Dual functional sensing mechanism in SnO(2)-ZnO core-shell nanowires, ACS Appl. Mater. Interfaces 6(2014) 8281-7.

[67] J.H. Kim, S.S. Kim, Realization of ppb-Scale Toluene-Sensing Abilities with Pt-

Functionalized SnO2-ZnO Core-Shell Nanowires, ACS Appl. Mater. Interfaces 7(2015) 17199-208.

[68] J.H. Kim, A. Katoch, S.H. Kim, S.S. Kim, Chemiresistive sensing behavior of SnO_2 (n)-Cu_2O (p) core-shell nanowires, ACS Appl. Mater. Interfaces 7(2015) 15351-15258.

[69] A. Mirzaei, J.-H. Kim, H.W. Kim, S.S. Kim, How shell thickness can affect the gas sensing properties of nanostructured materials: Survey of literature, Sens. Actuators B Chem. 258(2018) 270-94.

[70] J.H. Lee, J.H. Kim, S.S. Kim, CuO-TiO_2 p-n core–shell nanowires: Sensing mechanism and p/n sensing-type transition, Appl. Surf. Sci. 448(2018) 489-497.

[71] J.H. Kim, J.H. Lee, J.Y. Kim, A. Mirzaei, H.W. Kim, S.S. Kim, Enhancement of CO and NO_2 sensing in n-SnO_2-p-Cu_2O core-shell nanofibers by shell optimization, J. Hazard. Mater. 376(2019) 68-82.

[72] L. Zhu, K. Yuan, J. Yang, H. Ma, T. Wang, X. Ji, J. Feng, A. Devi, H. Lu, Fabrication of heterostructured p-CuO/n-SnO_2 core-shell nanowires for enhanced sensitive and selective formaldehyde detection, Sens. Actuators B Chem. 290(2019) 233-241.

[73] J. Bai, C. Zhao, H. Gong, Q. Wang, B. Huang, G. Sun, Y. Wang, J. Zhou, E. Xie, F, Wang, Debye-length controlled gas sensing performances in NiO@ZnO p-n junctional core–shell nanotubes, J. Phys. D: Appl. Phys. 52(2019) 285103.

[74] T. Zhou, X. Liu, R. Zhang, L. Wang, T. Zhang, Constructing Hierarchical Heterostructured Mn_3O_4/Zn_2SnO_4 Materials for Efficient Gas Sensing Reaction, Adv. Mater. Interfaces 5(2018) 1800115.

[75] N. Kaur, D. Zappa, M. Ferroni, N. Poli, M. Campanini, R. Negrea, E. Comini, Branch-like NiO/ZnO heterostructures for VOC sensing, Sens. Actuators B Chem. 262(2018) 477-485.

[76] H. Kwon, J.S. Yoon, Y. Lee, D.Y. Kim, C.K. Baek, J.K. Kim, An array of metal oxides nanoscale hetero p - n junctions toward designable and highly-selective gas sensors, Sens.

Actuators B Chem. 255(2018) 1663-1670.

[77] S.M. Sze, K.K. Ng, Physics of Semiconductor Devices 3rd Edition, John Wiley & Sons Enc., 2007, 124–127

[78] F. Xu, H.P. Ho, Light-Activated Metal Oxide Gas Sensors: A Review, Micromachines (Basel), 8(2017).

[79] X. Liu, S. Ma, S. Zhu, Y. Zhao, X. Ning, L. Zhao, J. Zhuang, Light stimulated and regulated gas sensing ability for ammonia using sulfur-hyperdoped silicon, Sens. Actuators B Chem. 291(2019) 345-353.

[80] A. Gad, M.W.G. Hoffmann, O. Casals, L. Mayrhofer, C. Fàbrega, L. Caccamo, F.H. Ramírez, M.S. Mohajerani, M. Moseler, H. Shen, A. Waag, J.D. Prades, Integrated Strategy toward Self-Powering and Selectivity Tuning of Semiconductor Gas Sensors, ACS Sens. 1(2016) 1256-1264.

[81] M.W.G. Hoffmann, A.E. Gad, J.D. Prades, F. Hernandez-Ramirez, R. Fiz, H. Shen, S. Mathur, Solar diode sensor: Sensing mechanism and applications, Nano Energy, 2(2013) 514-522.

[82] M.W. Hoffmann, L. Mayrhofer, O. Casals, L. Caccamo, F.H. Ramirez, G. Lilienkamp, W. Daum, M. Moseler, A. Waag, H. Shen, J.D. Prades, A highly selective and self-powered gas sensor via organic surface functionalization of p-Si/n-ZnO diodes, Adv. Mater. 26(2014) 8017-8022.

[83] R. Tanuma, M. Sugiyama, Polycrystalline SnO_2 Visible-Light-Transparent CO_2 Sensor Integrated with NiO/ZnO Solar Cell for Self-Powered Devices, Physica. Status. Solidi (a), (2019) 1800749.

[84] X. Liu, S. Zhu, H. Sun, Y. Hu, S. Ma, X. Ning, L. Zhao, J. Zhuang, “Infinite Sensitivity” of Black Silicon Ammonia Sensor Achieved by Optical and Electric Dual Drives, ACS Appl. Mater. Interfaces 10(2018) 5061-5071.

[85] Pankove, J. I. Optical Processes in Semiconductors; Prentice-Hall, Inc.: Englewood Cliffs, NJ, USA, 1971.

Chapter 2: Design of Novel ZnO@SnO_2 n-n Heterostructures for Highly Sensitive NO_2 Sensing

2.1. Abstract

The novel brush-like (B-) ZnO@SnO_2 n-n hierarchical nanostructures (HNSs) were successfully synthesized by using a simple two-step hydrothermal method. The SnO_2 nanowires grown epitaxially on ZnO nanorods with a six-fold symmetry. The heterogeneous nucleation-growth processes of SnO_2 and ZnO were discussed in detail by varying reaction times and temperatures. The excellent sensing performances of B-ZnO@SnO_2 HNSs toward NO_2 were studied, including high sensitivity, fast response, broad detection range and low detection limit (DL). The detection range of the sensor was measured from 5 ppb to 10 ppm, and the DL of the sensor was 5 ppb at 150 ℃. The response and recovery time which reach 90% of the final signal was less than 60 s. The enhanced sensing performance was attributing to the unique structure of B-ZnO@SnO_2 HNSs, which can provide large specific surface area and can induce synergism effect due to the formed multi-junctions.

Author contributions: Lin Liu has got the permission from other co-authors for this paper to her thesis. Lin Liu is responsible for fabrication of sensors, measurement of sensing performance and relevant data analysis, and also contributes to write and revise the manuscript.

2.2. Introduction

O_3, SO_2 and NO_2 are three main hazardous oxidizing gases and have aroused great attention in the society. The secondary national ambient air quality standards (NAAQS) for these gases are 70 ppb, 500 ppb and 53 ppb, respectively, which are set by U.S. Environmental Protection Agency (EPA) [1]. Among them, NO_2 is one of the most hazardous and widespread gas pollutants with the lowest secondary NAAQS, which is generated from industries and automotive engines. Trace concentration of the NO_2 can induce respiratory diseases (*e.g.,* bronchitis and emphysema respiratory) and the emitted NO_2 can also cause many environmental problems such as acid rain and photochemical smog [1-5]. Consequently, measurement of the NO_2 has attracted significant attention in society. Up to now, various NO_2 sensors have been fabricated based on different types of metal oxides including Fe_2O_3, In_2O_3, WO_3, NiO, ZnO, CdO, and SnO_2 [5-8]. Among them, SnO_2 and SnO_2–based nanomaterials have received significant attention in both theoretical and experimental studies [9, 10]. However, using pure SnO_2 as sensing material may result in some problems such as low response, poor selectivity as well as slow response-recovery time [7, 11-13]. Several approaches have been developed to address these problems such as modifying with noble metals, doping elements and constructing heterostructures [14-16]. The heterostructures containing two or more phases can promise a variety of properties to enhance the sensing performance, such as multi-junction modulations, synergic effects and the hetero-interfacial effect [7, 11, 17-19]. For example, owing to the multi-junction modulations, different metal oxide/SnO_2 heterostructures offer the possibility to enhance the sensing performance by modulating potential barriers and charge transduction at the hetero-interface and grain boundaries [18-21].

ZnO, as an important semiconductor material with a band gap of 3.37 eV, has a good performance in extensive applications [22-24]. For the gas sensors, ZnO-based hetero-

nanostructures are considered as an ideal material system to detect various hazardous and toxic gases due to their high sensitivity and selectivity [25-31]. Recently, many studies verify the enhanced performance of sensors based on SnO_2@ZnO or ZnO@SnO_2 heterostructures [11, 16, 32-36]. For example, the response of the SnO_2@ZnO C-S heterostructures improves 2~3- and 3~6-fold compared to that of pure SnO_2 nanowires and that of pure ZnO nanorods, respectively [16]. However, these sensors require high operation temperature (*e.g.,* 300 to 400 ˚C) and the detection limits (DLs) are far from the ultralow concentrations (several ppb level) [17, 32-41]. Consequently, designing and synthesizing of SnO_2-ZnO composites with novel architectures which can work at relative low temperature with ultralow DLs are still facing with much challenges so far.

Various of SnO_2@ZnO materials [16, 42-46], ZnO@SnO_2 materials [47-52], and SnO_2-ZnO composites [21, 53-55] have been reported by using the vapor phase [16, 42, 43, 50-52], liquid phase [44-49, 53], and electrospinning method [21, 54, 55], respectively. Compare with these methods, liquid phase, especially hydrothermal method is regarded as a high-throughput and low-cost route to synthesize nanomaterials. In this work, brush-like (B-) ZnO@SnO_2 hierarchical nanostructures (HNSs) were synthesized via a two-step hydrothermal method without template, seed layer, additive-salt and surfactant. The growth mechanism was investigated systematically by varying the reaction time and temperature. The performances of sensors based on the pure ZnO, pure SnO_2, and B-ZnO@SnO_2 HNSs were investigated. The B-ZnO@SnO_2 HNS-based sensor achieved the highest sensing performance at a relative low working temperature (150 ˚C). The DL of B-ZnO@SnO_2 HNS-based sensor was as low as 5 ppb and the response-recovery time of that was less than 60 s.

2.3 Experimental Section

2.3.1 Synthesis of Materials.

All chemicals and reagents were analytical grade and were used without further

purification. The B-ZnO@SnO_2 HNSs were synthesized using a two–step hydrothermal method. The fabrication of B-ZnO@SnO_2 HNSs nanostructures was identical to the previous work [56].

In order to synthesis of ZnO nanorods, 4.0833 g NaOH (96%) solution was rapidly dropped into 1.5520 g $Zn(CH_3COO)_2{\cdot}2H_2O$ (99%) solution under stirring conditions for 30 min. After that, a total of 35 mL solution was transferred into a 50 mL stainless steel Teflon–lined autoclave and then was heated in bake oven at 100 ˚C for 12 h. Finally, the products were purged in deionized water for several times. The sample was separated in absolute ethyl alcohol and dried at 60 ˚C in air.

The B-ZnO@SnO_2 HNSs were synthesized by using the as-prepared ZnO nanorods as zinc source. In a typical experiment, 1.2395 g $SnCl_4{\cdot}5H_2O$ (99%) solution was slowly dropped into 1.6042 g NaOH (96%) solution under stirring conditions. Then, 0.0475 g ZnO nanorods were added in the solutions under stirring conditions for 1 h followed by ultrasonic treatment for 10 min. 35 mL solution in total was transferred into a 50 mL stainless steel Teflon–lined autoclave and then was heated in bake oven at 200 ˚C for 20 h. Finally, the products were washed with deionized water for several times. The sample was separated in absolute ethyl alcohol and dried at 60 ˚C in air for further characterization.

The SEM and EDXS samples were prepared by pasting a little amount of material powders onto the conductive tape and then some Au nanoparticles were deposited to enhance the conductivity of the material. Before preparation the TEM samples, a small amount of material powders was added into ethanol and sonicated for 5 min. Then, 10 μL of prepared ZnO@SnO_2 dispersion solution was dropped onto the Cu film and then the TEM samples were obtained after the Cu film was dried.

2.3.2 Characterization

The prepared samples were characterized using X-ray powder diffraction (XRD,

SHIMADZU 6100) equipped with Cu Kα X-ray source operated at 40 kV and 30 mA. The scan rate of 6 degree/min and step size of 0.02 degree were used. The scanning electron microscope (SEM, Zeiss ΣIGMA/VP) analyses were performed at 3 kV with a working distance of ~9 mm. The energy dispersive X-ray spectrometer (EDXS) and elemental mapping studies were performed at 15 kV under the SEM. Transmission electron microscope (TEM) characterizations were performed on JEM-3010 at operating voltage of 200 kV. The X-ray photoelectron spectroscopy (XPS, ESCALAB 250Xi) experiments were carried out with a monochromatized Al Kα X-ray source (hν=1486.6 eV). A 30-μm diameter X-ray spot with a step size of 5 μm was used in the analyses. The binding energies (standard deviation = ±0.2 V) correction for charging was performance by assigning a value of 284.8 eV to the adventitious C1s line [57, 58].

2.3.3 Gas Sensing Measurement

Before fabricating the gas sensors, 0.3 ml terpilenol was added into a small tube which contains 100 mg B-ZnO@SnO_2 HNSs powders to make sensing material paste. Then the prepared paste was drop-coated onto the centric part of the micro-hotplates (Leanstar Co.Ltd), and dried in the air at room temperature. Then, the sensors were annealed in the oven under the argon atmosphere at 200 ˚C for 1 h. The fabricated sensors were placed in a small quartz chamber with one air inlet and one air outlet for real-time measurement. Real–time response of the sensors was conducted by a costumed LabVIEW program under 2 V DC (National Instruments, Austin, TX, USA). Different concentrations of the NO_2 were prepared by stoichiometric mixing the target gas and the dry air using two mass flow controllers (MFCs). The working temperatures of the sensors were controlled by tuning voltages of heating electrodes. Responses toward oxidizing and reducing gases were defined as $S = (R_g - R_a)/R_a = \Delta R/R_a$ and $S = (R_a - R_g)/R_g = \Delta R/R_g$, respectively. Where R_a (R_g) is the resistance in air (target gas).

2.4. Results and Discussion

2.4.1 Structure and Morphology Characterization

Figure 2.1a shows the SEM image of the B-ZnO@SnO_2 HNSs. Each ZnO nanorod was wrapped by the SnO_2 nanowires densely and formed the brush-like morphologies. Figure 2.1b shows the XRD pattern of B-ZnO@SnO_2 HNSs, which are in accordance with the hexagonal ZnO (space group $P6_3/mc$, JCPDS file NO. 36-1451) and the rutile SnO_2 (space group $P4_2/mnm$, JCPDS file No. 41-1445). Besides, the EDXS (Figure 2.1c, area-scan) results indicated that the B-ZnO@SnO_2 HNSs were consisted of Zn, Sn, and O elements. The atomic ratio (Sn/Zn) was measured to be ~2.44, which deviated from the initial molar ratio of Sn/Zn (Sn:Zn=6:1), indicating that just some of Sn source participated in the growing process. The observed peaks of C and Au are ascribing to the substrate (conductive tape) and the deposited Au nanoparticles, respectively.

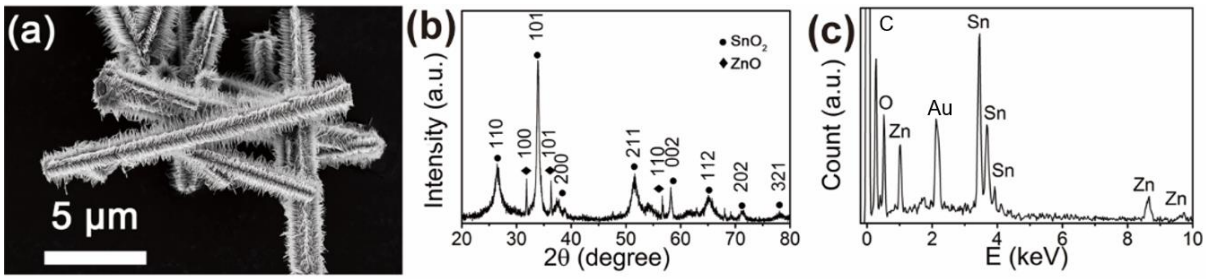

Figure 2.1 (a) SEM images, (b) XRD pattern and (c) EDXS spectrum of B-ZnO@SnO_2 HNSs.

The SEM image and the EDXS line profile of B-ZnO@SnO_2 HNSs in the radial direction are shown in Figure 2.2. The EDXS (line-scan) spectrum of B-ZnO@SnO_2 HNSs (Figure 2.2b) demonstrates that the percentage of Sn mass exceeds that of O and Zn, which is in accordance with the area scanning results (Figure 2.1c). The elemental mapping (Figure 2.2c-f) reveals the uniform distribution of Sn, O and Zn elements in the B-ZnO@SnO_2 HNSs.

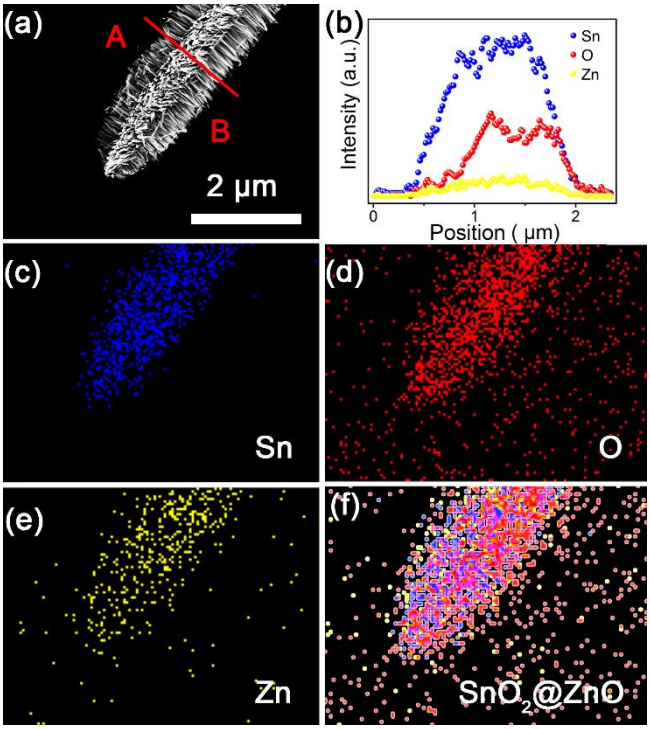

Figure 2.2 (a) SEM image of B-ZnO@SnO_2 HNSs and the EDXS line profile in the radial direction, (b) The EDXS line-scan spectrum and (c-f) elemental mapping patterns of Sn, O, and Zn of B-ZnO@SnO_2 HNSs.

The TEM image (Figure 2.3a) of the B-ZnO@SnO_2 HNSs illustrated that the uniform SnO_2 nanowires (with a length of 1-1.5 μm and a diameter of ~50 nm) were grown on the ZnO nanorods densely. The selected area electron diffraction (SAED) of an individual SnO_2 nanowire (Figure 2.3b) proved that the SnO_2 nanowires were single crystalline. The high-resolution TEM (HRTEM) image (Figure 2.3c) and corresponding fast Fourier transform (FFT) image (inset, taken from the marked box) further confirmed the single crystalline of the SnO_2 nanowires. The spacing between adjacent lattice planes was 0.333 nm, which is corresponding to (110) planes of rutile SnO_2, indicating that [001] facet was the preferential growth direction.

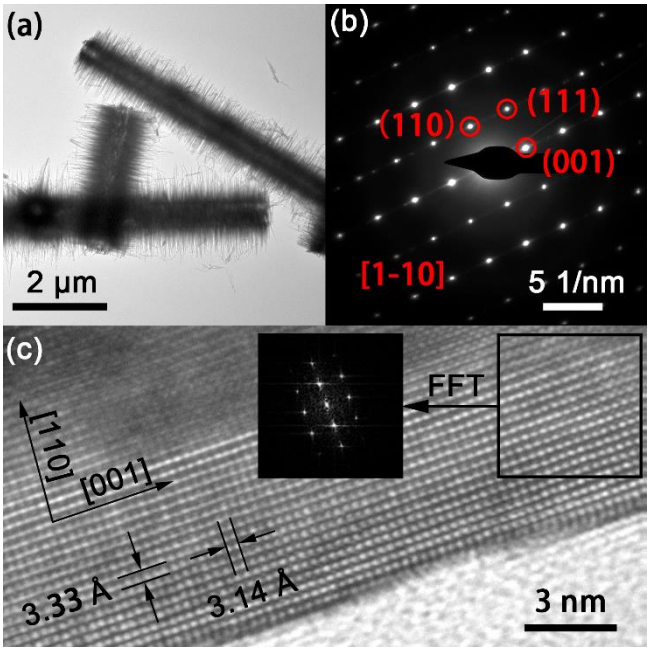

Figure 2.3 (a) TEM image of B-ZnO@SnO_2 HNSs, (b) SAED and (c) HRTEM image of SnO_2 nanowire.

In order to further confirm the chemical composition of the B-ZnO@SnO_2 HNSs, the XPS spectrum was carried out as shown in Figure 2.4. The peaks of Zn, Sn, O, and C could be observed in the spectrum without any extra peaks of impurities. The peaks centered at 486.4 and 494.8 eV correspond to Sn $3d_{5/2}$ and Sn $3d_{3/2}$, respectively, and the peaks centered at 1021.6 and 1044.7 eV correspond to Zn $2p_{3/2}$ and Zn $2p_{1/2}$, respectively (Figure 2.4b and c) [28, 59-61]. Figure 2.4d shows the O 1s spectrum of the B-ZnO@SnO_2 HNSs. The peaks centered at 530.2 eV and 531.6 eV are corresponding to the lattice oxygen in ZnO and in SnO_2, respectively [28, 58, 59, 62]. In addition, the atomic ratio (Sn/Zn) of B-ZnO@SnO_2 HNSs is 2.54 according to the XPS result, which is in conformity with EDXS results.

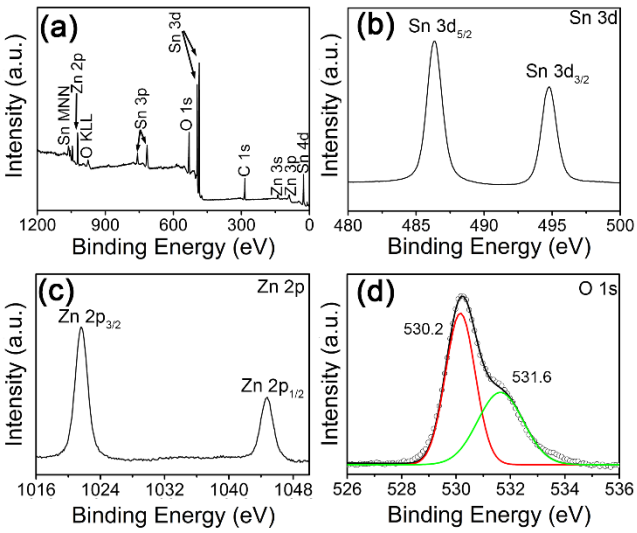

Figure 2.4(a) XPS survey spectrum of B-ZnO@SnO_2 HNSs, (b) Sn 3d region, (c) Zn 2p region, (d) O1s region (full) with the corresponding fits for lattice oxygen in crystalline ZnO (red) and SnO_2 (green).

2.4.2. Growth Mechanism of the B-ZnO@SnO_2 HNSs

The ZnO nanorods were synthesized in the first hydrothermal step and were used as the zinc sources in the second step. The XRD pattern and SEM image of synthesized pure wurtzite structure ZnO nanorods in the first step were demonstrated in Figure S2.1. The growth process of B-ZnO@SnO_2 HNSs was investigated via changing the reaction times and temperatures in the second step. Figures 2.5a to f depict the SEM images of B-ZnO@SnO_2 HNSs by increasing the reaction time (15 min, 2, 6, 10, 20 and 24 h) at 200 °C. At beginning, the ZnO nanorods reacted with OH^- anions to form $Zn(OH)_4^{2-}$ and then reacted with $Sn(OH)_6^{2-}$to produce octahedral $ZnSn(OH)_6$ (ZHS, space group Pn-3, JCPDS file NO. 73-2384) (Figure 2.5a). Then, the octahedral ZHS was decomposed starting from the points, and the ZnO nanorods were formed and embedded in the truncated octahedron after reaction of 2 h (Figure 2.5b). The increase of XRD peak intensity of ZnO and the decrease of XRD peak intensity of ZHS indicated that the content of ZnO increased along with the reaction time (Figure 2.5g). The initial morphology of B-ZnO@SnO_2 HNSs was formed when the reaction time was prolonged

to 6 h (Figure 2.5c). Meanwhile, the diffraction peaks of both ZnO and ZHS were disappeared in the XRD results due to the complete decomposition of ZHS and the densely covered of SnO_2 nanowires on the surface of ZnO (Figure 2.5g). Then, the SnO_2 nanowires were further grown (Figure 2.5d, 10 h) and the B-ZnO@SnO_2 HNSs were obtained at 20 h (Figure 2.5e). However, the cubic ZHS was observed when the reaction time is prolonged to 24 h. In addition, the SEM images and XRD patterns of more samples with the different reaction times (15, 30 min, 1, 2, 4, 6, 8, 10, 12, 16, 20 and 24 h) were given in Figure S2.2 and Figure S2.3, respectively. These morphology and structure results indicate that 20 h is the most suitable reaction time for synthesizing B-ZnO@SnO_2 HNSs.

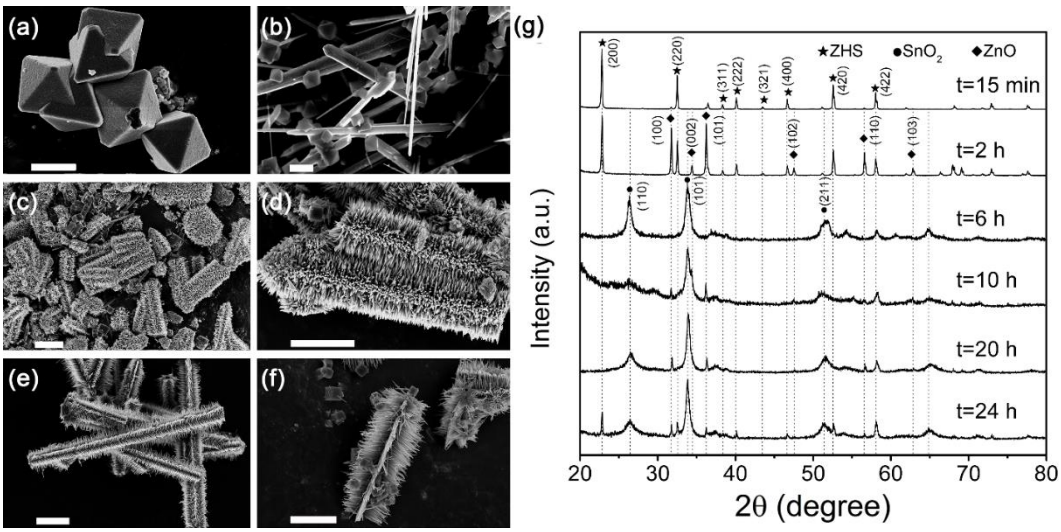

Figure 2.5 (a-f) The SEM images (Scale bars, 2 μm) and (g) XRD patterns of B-ZnO@SnO_2 HNSs at 200 °C for different reaction time: (a) 15 min, (b) 2, (c) 6, (d) 10, (e) 20, (f) 24 h.

The effect of reaction temperature was also studied to figure out the growth mechanism of the B-ZnO@SnO_2 HNSs. Figures 2.6a to f show the SEM images of B-ZnO@SnO_2 HNSs by increasing the reaction temperatures (160, 170, 180,190, 200 and 210 °C) after growing 20 h. Some octahedral ZHS gathered around ZnO nanorods and others combined with ZnO at 160 °C (Figure 2.6a). With increasing of the reaction temperature, the quantity of the ZnO nanorods increased and some SnO_2 nanoparticles appeared on the surface of ZnO nanorods at

170 °C (Figure 2.6b). When the reaction temperature reached at 180 °C, some SnO_2 nanowires grew on the ZnO nanorods chaotically and sparsely (Figure 2.6c). While, the SnO_2 nanowires grew on the ZnO uniformly and densely at 190 °C (Figure 2.6d), which caused the diffraction peaks of ZnO almost disappear at 190 °C (Figure 2.6g). The perfect B-ZnO@SnO_2 HNSs were formed at 200 °C. However, the diffraction peaks of ZnO were disappeared again at 210 °C. In order to explore the growth mechanism, additional samples were prepared at 195 and 205 °C and characterized with SEM and XRD (Figure S2.4 and Figure S2.5). The density of SnO_2 nanowires at 195 °C was lower than that of sample at 190 °C, so that the diffraction peaks of ZnO could be observed. While, at 205 °C, the length of ZnO was reduced and ZnO nanorods were almost dissolved so that the diffraction peaks of ZnO disappeared.

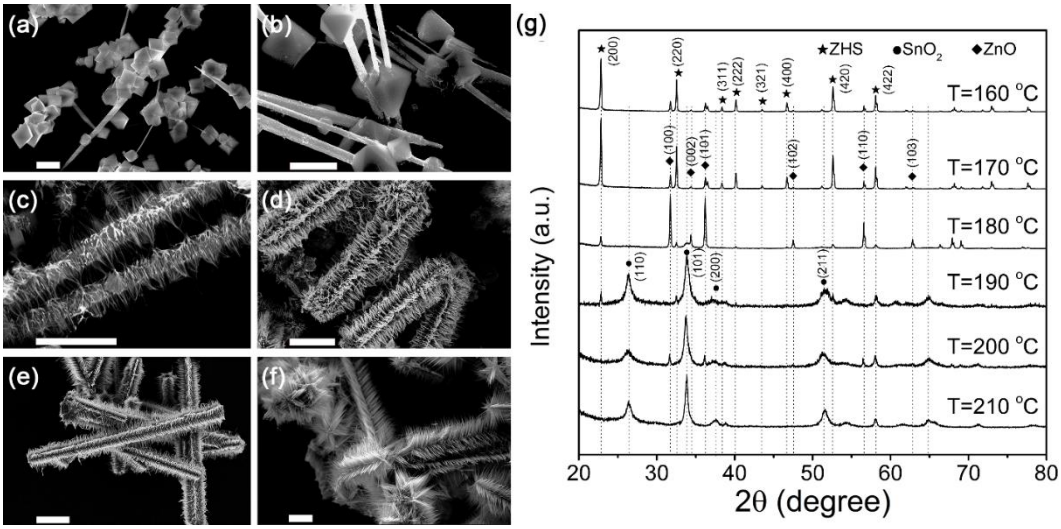

Figure 2.6 The SEM images (Scale bars, 2 μm) and (g) XRD patterns of B-ZnO@SnO_2 HNSs with different reaction temperature: (a) 160, (b) 170, (c) 180, (d) 190, (e) 200, (f) 210 °C for 20 h.

Based on the experimental results, we proposed a reasonable growth mechanism for the B-ZnO@SnO_2 HNSs. Both of the ZnO nanorods and Sn^{4+} play an important role in synthesizing B-ZnO@SnO_2 HNSs. In the first hydrothermal step, the hydrolyzation of zinc acetate dihydrate can form $Zn(OH)_4^{2-}$ and ZnO crystal nucleus in the alkali solution.

Subsequently, $Zn(OH)_4^{2-}$ anions tend to fold together on the polar surface (0001) of ZnO crystalline due to the electrostatic attraction. resulting in that the ZnO nanorods preferentially grow along with the orientation of c–axis.

In the second hydrothermal step, the ZnO nanorods are dissolved in the alkaline solution (NaOH) to form $Zn(OH)_4^{2-}$ anions to serve as zinc source [53, 63]. In addition, the $Sn(OH)_6^{2-}$ anions are generated owing to the reaction between the Sn^{4+} and OH^- in the strong alkaline solution [64]. Then, under the hydrothermal conditions, the $Sn(OH)_6^{2-}$ and $Zn(OH)_4^{2-}$ react to form ZHS [65, 66]. It is reported that the concentration of OH^- can affect the morphology of the ZHS [66-68]. When increasing molar ratio of OH^-:Zn:Sn to ~17:1:1, the octahedral ZHS is obtained [66-68]. Hence, in this case, as the molar ratio of OH^-:Zn:Sn is 69:1:6, the high concentration of OH^- leads to rapid formation of the octahedral ZHS (Figure 2.7, 15 min). Because ZHS is not very stable in a solution contained excessive OH^-, the ZHS will react with the OH^- and be decomposed to form ZnO and SnO_2 nanocrystalline [66]. As a result, the octahedral ZHS is decomposed by the OH^- which starts from the maximum active sites (the point angles) to form the truncated octahedral ZHS (Figure 2.7, 1 h). Therefore, the high concentration of the $Zn(OH)_4^{2-}$ and $Sn(OH)_6^{2-}$ are coexisted in a small range of the point angles [67]. It is known that bond enthalpies of Zn–O and Sn–O bonds are 159 ± 4 and 531.8 ± 12.6 kJ/mol at 298 K [69], respectively, and lattice energies of ZnO and SnO_2 are 3971 and 11807 kJ/mol, respectively [70]. Thus, it is much easier to form ZnO compared with the formation of SnO_2. The high supersaturation of ZnO crystal nucleus ensures ZnO nanorods grow rapidly and the existed few SnO_2 crystal nucleus in this stage have little influence on the growth of ZnO [71, 72]. As, the ZnO crystal nucleus are distributed at the point angles of the truncated octahedral ZHS, the initial formed ZnO nanorods are embedded in the point angles of truncated octahedral ZHS (Figure 2.7, 1 h). The XRD intensity of ZnO became significantly strong with increased reaction time (Figure S2.3).

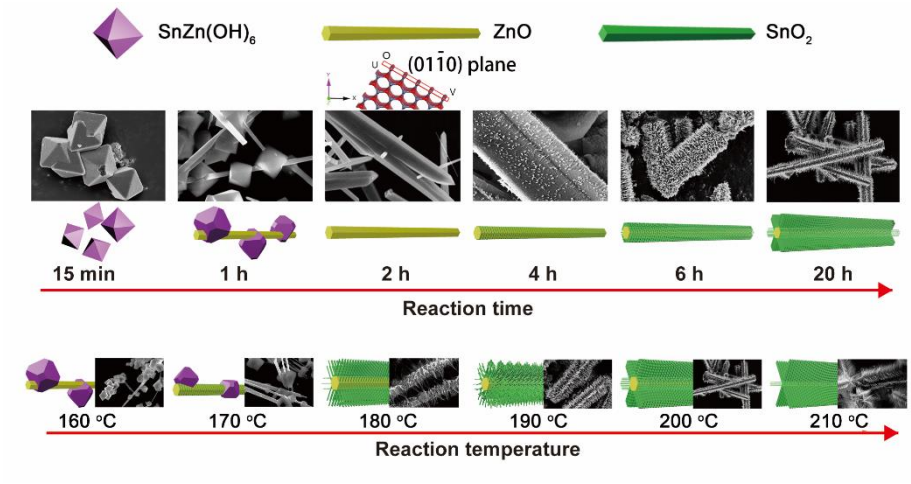

Figure 2.7 Schematic illustration of the reasonable growth mechanism of B-ZnO@SnO_2 HNSs.

By further increasing the reaction time, the crystal nucleus of SnO_2 are appeared. As the (001) facet of SnO_2 owns the highest surface energy, the [001] direction is the preferred growth direction for SnO_2 [73, 74]. When the reaction time is increased to 6 h, the SnO_2 nanocrystalline gradually grow into SnO_2 nanowires along with the [001] direction via the Ostwald ripening and then the initial morphology of B-ZnO@SnO_2 HNSs was formed [75-77]. When the reaction time was 20 h, the SnO_2 nanowires gradually grew on the surface six non–polarized plane of ZnO nanorods uniformly and completely.

The decomposition rate of ZHS is greatly enhanced by increasing the reaction temperature. At 160 °C, the temperature is too low to completely decompose the ZHS to form ZnO and SnO_2, because it cannot ensure the nucleation and growth speeds and supersaturation degree of ZnO or SnO_2 are high enough simultaneously. Therefore, the SnO_2 was not observed in the final results and a lot of ZHS were remained. At 170 °C, the reaction rate of the ZHS increases, as a result, the growth speed of ZnO and the amount of ZnO nanorods increase noticeably. In addition, as mentioned that the formation of SnO_2 is much more difficult than formation of ZnO, thus the low temperature (170 °C) results in the slow growth of SnO_2. Hence, only some SnO_2 nanocrystals can be seen on the surface of the ZnO nanorods at 170 °C. The growth speed

of the SnO_2 is significantly improved by further increasing the reaction temperatures (180 °C, 190 °C). When the reaction temperature is increased to 200 °C, some irregular SnO_2 nanoparticles or nanowires are further dissolved and then recrystallized via Ostwald ripening to form single crystal SnO_2 nanowires [75-77]. In addition, the decomposition rate of ZnO nanorods is dramatically enhanced at high reaction temperature (210 °C). Thus, once the ZnO nanorods are completely decomposed, the left hexagonal holes are sealed by the SnO_2 nanowires.

Figures 2.8a and b reveal that the SnO_2 nanowires were not perpendicular but inclined at an angle of 56° to the ZnO. In addition, no obvious evidence of a buffer layer between the ZnO nanorod and the SnO_2 nanowire was found, which meant that SnO_2 nanowires were epitaxially grown on the ZnO nanorod directly. To further investigate the hetero-interface between SnO_2 nanowire and ZnO nanorod, the HRTEM image viewed along the (0001) plane of ZnO nanorod is shown in Figure 2.8c. The SnO_2 nanowires were inclined at an angle of 56° to the ZnO nanorod, which is consistent with the SEM images. FFT patterns (Figure 2.8d-e) of the SnO_2 nanowire and ZnO nanorod (marked by the squares) indicated that SnO_2 nanowires were grown on the (01-10) plane of ZnO nanorods along [001] direction of the SnO_2. The HRTEM image (Figure 2.8f) further confirmed that the (110) plane of SnO_2 and the (01-10) plane of ZnO were connected at the hetero-interface with a ~4° tilt attributing to the lattice mismatch.

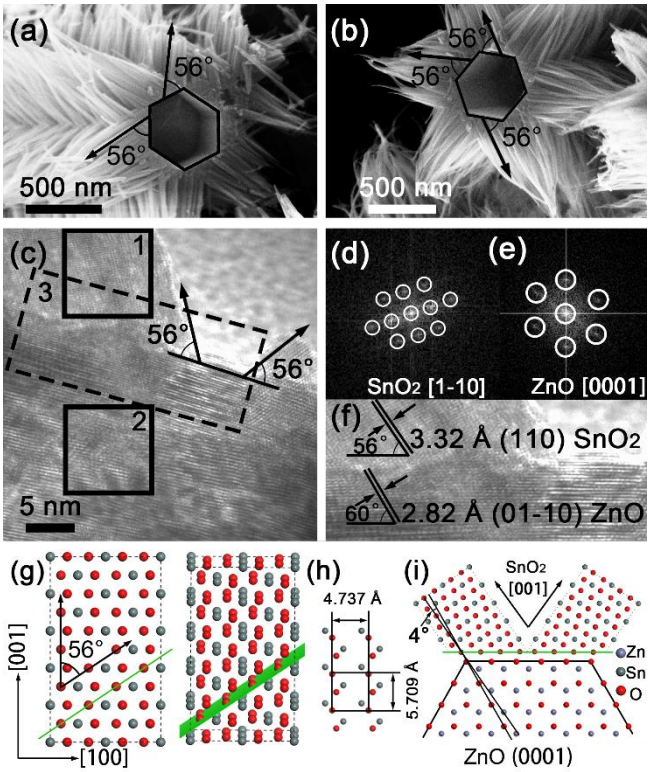

Figure 2.8 (a-b) The tilted view SEM images of well–aligned SnO_2 nanowires grow on ZnO non-polar surface along the [001] direction. (c) HRTEM image of the interfacial area of B–ZnO@SnO_2 HNSs. (d-e) FFT images of selected areas on SnO_2 nanowire and ZnO nanorod marked by the squares 1 and 2 in Figure 2.8c, respectively. (f) High magnification image of the interfacial area marked by the dotted box 3 in Figure 2.8c. (g) Interfacial area (green plane) of [001]-growth-orientation SnO_2 nanowires. (h) Atoms arrangements of the SnO_2 interfacial area in panel g, (i) The schematic representation of the atomic configuration of the B–ZnO@SnO_2 interface viewed along the [0001] direction of ZnO.

The epitaxial relation about SnO_2 and ZnO in most reports are the $(010)_{SnO2} \| \{01-10\}_{ZnO}$, $(010)_{SnO2} \| \pm(0001)_{ZnO}$ and $\{101\}_{SnO2} \| (0001)_{ZnO}$ [44, 52, 74, 78, 79]. However, in our case, the SnO_2 nanowires show a selective growth on the (01–10) plane of ZnO with an inclined 56°. The interfacial area (green plane) of [001]-growth-orientation SnO_2 nanowires is shown in Figure 2.8g and corresponding atoms' arrangement is shown in Figure 2.8h. The lattice (O-O distance) mismatches in the interfacial area between SnO_2 and (01-10) of ZnO are 12.2 % and

8.9 %, respectively. Figure 2.8(i) shows a schematic model of the SnO_2 nanowires surrounding on all the {01-10} surfaces of a ZnO hexagonal nanorods. The model is projected from the [0001] direction of the ZnO. The theoretical misorientation between ZnO and SnO_2 is 4°, agreeing well with the experimental result.

2.4.3. Gas Sensing Performances of the B-ZnO@SnO_2 HNSs

The performance of B-ZnO@SnO_2 HNS-based sensors were evaluated and compared with that of pure ZnO and pure SnO_2-based sensors at 150 °C. The dynamic response of the B-ZnO@SnO_2 HNS-based sensor to different NO_2 concentrations is shown in Figure 2.9a. The sensor showed obvious response (0.2) to 5 ppb NO_2 with fast response and recover time (60 s and 45 s, respectively) with a signal-to-noise ratio over the threshold of 3. Obviously, it takes longer time for the device to reach equilibrium for high gas concentration (> 60 s for 10 ppm) as compared with low concentration (45 s for 5 ppb). This is because the equilibrium rate constant may reduce when increase the initial NO_2 concentrations [80]. Nashaat N.Nassar has reported that when increase the initial concentration of asphaltene, the obtained equilibrium rate constant decrease based on the pseudo-second-order kinetic model [80]. The response of the sensor exhibited a linear relationship when detection range changed from 5 ppb to 800 ppb and 1 ppm to 10 ppm, respectively, (Figure 2.9b). The responses of the sensors based on B-ZnO@SnO_2 HNSs, SnO_2 nanowires and ZnO nanorods to 1 ppm NO_2, acetone, C_7H_8, H_2S, $CHCl_3$, NH_3, and ethanol were measured at 150 °C (Figure 2.9c). Compared with other two sensors, the sensor based on B-ZnO@SnO_2 HNSs showed the highest sensing response to NO_2.The sensing response of B-ZnO@SnO_2 HNS-based sensor to 1 ppm NO_2 was 25.5, while the sensing response to other six gases were measured to be less than 1. Compared with other reported NO_2 sensors based on ZnO@SnO_2 (Table S2.1), our work shows superior sensing performances such as high response, low DL, and fast response-recovery time. The stability was also studied, Figure S2.7 and Figure S2.8 shows the dynamic sensing response of B-

ZnO@SnO_2 HNS-based sensor after staying in air for 7 months. The response of the sensor just changed around 14% over 7 months, which demonstrates the sensor based on B-ZnO@SnO_2 HNSs has a good stability. In addition, the humidity effect was also investigated at 150 °C under the relative humidity (RH) of 85% after staying for 7 months (Figure S2.9). The response to the humidity was very low (less than 3 to 85% RH) similar to the other detected reducing gases in this work.

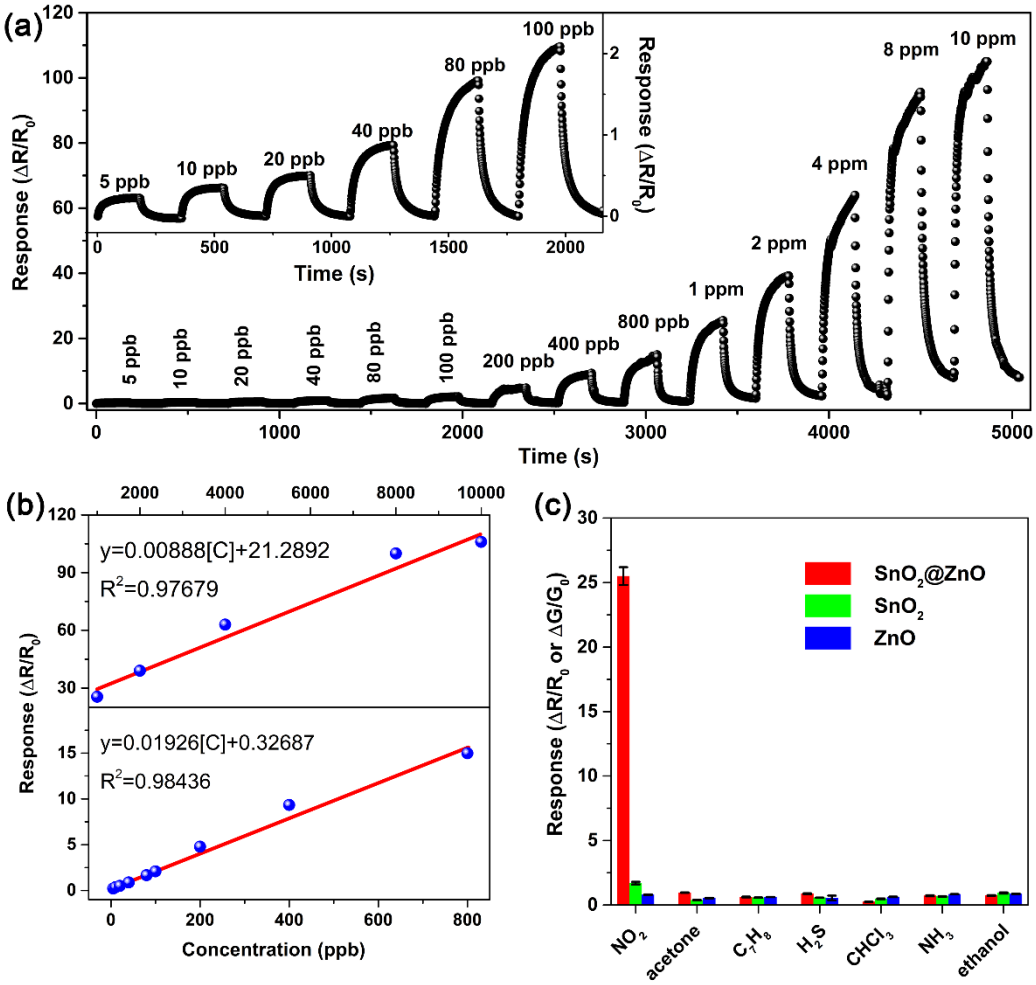

Figure 2.9 (a) Real-time response of the B-ZnO@SnO_2 HNSs sensor to NO_2 from 5 ppb to 10 ppm. (b) The linear relationship of the B-ZnO@SnO_2 HNSs sensor to NO_2 in the range of 5 ppb to 800 ppb and 1 ppm to 10 ppm. (c) Selectivity comparison of pure ZnO, SnO_2, and B-ZnO@SnO_2 HNSs sensors for different target gases at 1 ppm.

2.4.4. Gas Sensing Mechanism of the B-ZnO@SnO_2 HNSs

In order to address the sensing mechanism, the schematic sensing mechanism and the relevant energy band diagrams were demonstrated in Figure 2.10. Figure 2.10a is the schematic sensing mechanism of sensor based on single sensing material (take the pure SnO_2 for example in this case). When exposed to air, oxygen molecules will absorb onto the surface of the SnO_2 by extracting electrons from SnO_2 nanowires and form oxygen ions such as O_2^- and O^-. Then an electron-depletion layer (EDL) at the surface of SnO_2 nanowires is formed. When switching to NO_2, due to the high affinity, the NO_2 molecules will draw out the electrons from both SnO_2 and oxygen ions, resulting in expansion of EDL and increase of the resistance (Figure 2.10a) (Equations (2-1) - (2-4)) [38]. This is the sensing mechanism of the sensor based on single sensing material (pure SnO_2 or pure ZnO) and the sensing response is strictly dependent on the size of the sensing materials [81,82].

$$NO_2 + e^- \rightarrow NO_2^- \tag{2-1}$$

$$NO_2 + e^- \rightarrow NO + O^- \tag{2-2}$$

$$NO_2^- + O_2^- + 2e^- \rightarrow NO_2^- + 2O^- \tag{2-3}$$

$$NO_2^- + O^- + 2e^- \rightarrow NO + 2O^{2-} \tag{2-4}$$

For the sensor based on B-ZnO@SnO_2 HNSs, the enhancement sensing mechanism is ascribing to the increased specific surface area, the defects introduced by the lattice mismatch, and the formed multi-junctions compared with pure SnO_2- and pure ZnO-based sensors. The increased specific surface area guarantees more adsorption sites. The lattice mismatch between ZnO and SnO_2 could bring in the increase of oxygen vacancies, which provide more adsorption and reaction sites for oxygen and NO_2 molecules [83]. Besides, as the ZnO nanorods are densely covered by the SnO_2 nanowires, in this case, SnO_2 nanowires work as the main sensing sites and the conduction channel. The enhanced sensing performance of the sensor based on B-ZnO@SnO_2 HNSs is closely relevant with synergism effects of the formed multi-junctions [34,

35]. First, the unique heterostructure of B-ZnO@SnO_2 HNSs compels the electrodes to contact with the SnO_2 nanowires to form Schottky barrier (Figure S2.10 b-d). Part of the contact points were located at the tap of the SnO_2 nanowires with a diameter of ~10 nm, which is smaller than the range of the Debye length (λ_D) (around 8.4-21.6 nm for SnO_2 nanowires at 150 °C) [84,85]. Therefore, the modulated of the EDL in the radial direction is more obviously and the conduction channel in the tap of SnO_2 can be cut down rapidly and effectively by trace NO_2 (ppb level). Second, similar to the sensing mechanism of pure SnO_2-based sensor, the EDL will be broaden when the sensor is exposed to NO_2 and then the homojunction potential barrier ($\Delta\Phi_{homo}$) between SnO_2 nanowires will increase to hamper the transportation of electrons (Figure 2.10b). Last, the formed heterojunction at the hetero-interface of the SnO_2 and ZnO also contributes to enhance the gas sensing. In the vacuum, the electrons will transfer from SnO_2 to ZnO due to their different work functions ($\Phi_{(ZnO)}$=5.2 eV, $\Phi_{(SnO2)}$=4.9 eV) till their Fermi levels equilibrate and form a depletion layer at the hetero-interface of ZnO and SnO_2 (Figure 2.10c,d) [32, 34, 86]. The heterojunction potential barrier ($\Delta\Phi_{hetero}$) at the hetero-interface is produced by the different work functions. According to the ref. 86 and ref. 88, the overall resistance of the sensor can be described as following formula (2-5):

$$R = R_0 \exp\left(\frac{\Delta\Phi}{k_b T}\right) \tag{2-5}$$

where R_0 is constant, k is Boltzmann's constant, T is absolute temperature, and $\Delta\Phi$ is the effective potential barrier (including $\Delta\Phi_{homo}$ and $\Delta\Phi_{hetero}$). When the B-ZnO@SnO_2 HNSs are exposed in to the air, the O_2 molecule will absorb onto the surface of the SnO_2 nanowires and extract electrons from SnO_2 to form the oxygen ions such as O_2^- and O^-. As the diameter of SnO_2 nanowire is comparable with $2\lambda_D$ of SnO_2, the electrons of SnO_2 nanowire is almost depleted in the air [84,85]. Then, the Fermi level (E_f) of the SnO_2 will shift far away from the conduction band even lower than that of ZnO due to the reduced electron concentration. Thus, in order to reach a balance, the electrons will inject from ZnO nanorods to react with the oxygen

molecules (Figure 2.10e). Owing to the high affinity of NO_2 molecules, the NO_2 molecules will further withdraw the electrons from SnO_2 and oxygen ions. Thus, the $\Delta\Phi_{hetero}$ enlarges obviously compared with it in the air due to the further reduced electron concentration leading to increase of the resistance (Figure 2.10f) [88]. Therefore, the multi-junctions play an important role in enhancing the sensing performance of the B-ZnO@SnO_2 HNSs [88].

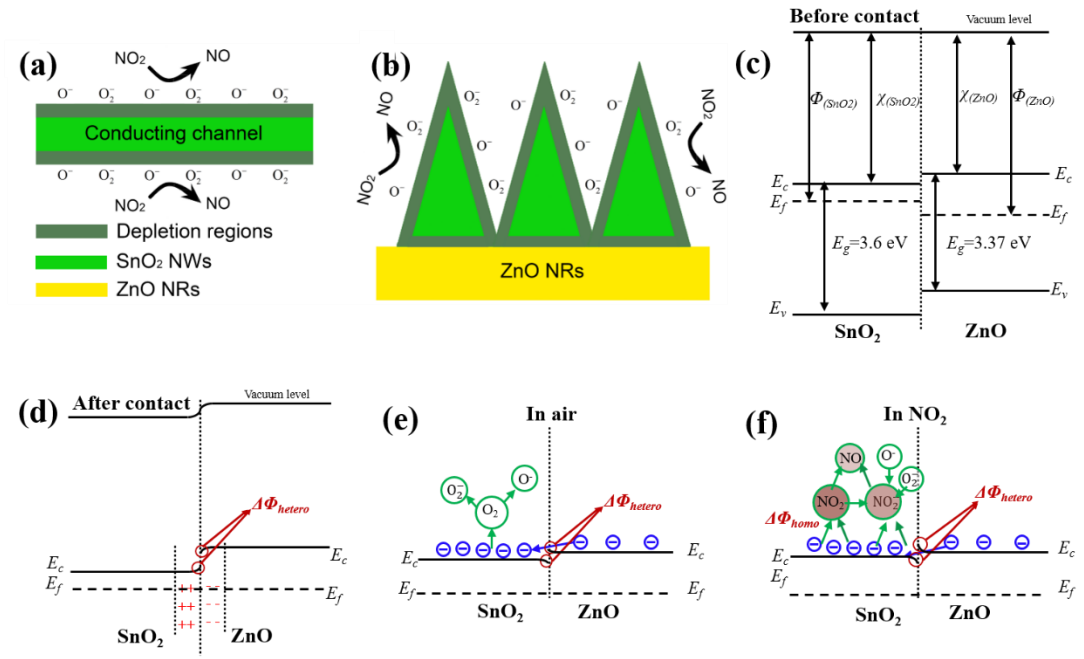

Figure 2.10 Schematic illustration of the sensing mechanisms with respect to (a) SnO_2 nanowires and (b) B-ZnO@SnO_2 HNSs; schematic diagrams of B–ZnO@SnO_2 at different stage: (c) Energy band diagram of SnO_2-ZnO system. Energy band diagram of SnO_2-ZnO heterojunction after contact in vacuum (d), in air (e), and in NO_2 (e).

2.5. Conclusions

B-ZnO@SnO_2 HNSs have been successfully synthesized using a facile two-step hydrothermal method, and the reaction time and temperature have a great impact on the morphology of B-ZnO@SnO_2 HNSs. The B-ZnO@SnO_2 HNSs based gas sensor shows the ultralow DL of 5 ppb with the fast response and recovery time (less than 60 s) at relatively low working temperature (150 ^{o}C). The great sensing performance of B-ZnO@SnO_2 HNSs sensor

is mainly due to the synergism effect of multi-junction in the B-ZnO@SnO_2 HNSs and also the enhanced specific surface area as well as the introduced defects. Overall, the synthesis strategy presents great potential for developing high performance sensing materials, which can also be applied to the synthesis of many other metal oxide nanomaterials. The terpilenol is used as organic binder to connect the prepared B-ZnO@SnO_2 powders and sensor chips for construction of gas sensor. However, the B-ZnO@SnO_2 powders will aggregate and influence the uniformity of sensing materials during the slurry-coating process. Thus, development of in situ grow method is a potential approach to obtain highly uniform sensing materials without aggregation.

2.6. Reference

[1] "NAAQS Table", United States Environmental Protection Agency, https://www.epa.gov/criteria-air-pollutants/naaqs-table.

[2] H. Long, H.T. Anna, T. Pham, Z. Tang, T. Shi, A. Zettl, C. Carraro, M.A. Worsley, R. Maboudian, High Surface Area MoS_2/Graphene Hybrid Aerogel for Ultrasensitive NO_2 Detection, Adv. Funct. Mater. 26 (2016) 5158-5165.

[3] J. Kong, N.R. Franklin, C. Zhou, M.G. Chapline, S. Peng, K. Cho, H. Dai, Nanotube Molecular Wires as Chemical Sensors, Science 287 (2000) 622-625.

[4] M.W.G. Hoffmann, J.D. Prades, L. Mayrhofer, F. Hernandez Ramirez, T.T. Järvi, M. Moseler, A. Waag, H. Shen, Highly Selective SAM–Nanowire Hybrid NO_2 Sensor: Insight into Charge Transfer Dynamics and Alignment of Frontier Molecular Orbitals, Adv. Funct. Mater. 24 (2014) 595-602.

[5] D. Zhang, Z. Liu, C. Li, T. Tang, X. Liu, S. Han, B. Lei, C. Zhou, Detection of NO_2 down to ppb Levels Using Individual and Multiple In_2O_3 Nanowire Devices, Nano Lett. 4 (2004) 1919-1924.

[6] G. Li, X. Wang, L. Liu, R. Liu, F. Shen, Z. Cui, W. Chen, T. Zhang, Controllable Synthesis of 3D $Ni(OH)_2$ and NiO Nanowalls on Various Substrates for High-Performance Nanosensors, Small 11 (2015) 731-739.

[7] J. Zhang, X. Liu, G. Neri, N. Pinna, Nanostructured Materials for Room-Temperature Gas Sensors, Adv. Mater. 28 (2016) 795-831.

[8] D. Peeters, D. Barreca, G. Carraro, E. Comini, A. Gasparotto, C. Maccato, C. Sada, G. Sberveglieri, Au/ε-Fe_2O_3 Nanocomposites as Selective NO_2 Gas Sensors, J. Phys. Chem. C. 118 (2014) 11813-11819.

[9] A. Sharma, M. Tomar, V. Gupta, Enhanced Response Characteristics of SnO_2 Thin Film Based NO_2 Gas Sensor Integrated with Nanoscaled Metal Oxide Clusters, Sens. Actuators B

Chem. 181 (2013) 735-742.

[10] A. Maiti, J. A. Rodriguez, M. Law, P. Kung, J. R. McKinney, P. Yang, SnO_2 Nanoribbons as NO_2 Sensors: Insights From First Principles Calculations, Nano Lett. 3 (2003) 1025-1028.

[11] D. Fu, C. Zhu, X. Zhang, C. Li, Y. Chen, Two-Dimensional Net-Like SnO_2/ZnO Heteronanostructures for High-Performance H2S Gas Sensor, J. Mater. Chem. A 4 (2016) 1390-1398.

[12] L. Wang, Y. Chen, J. Ma, L. Chen, Z. Xu, T. Wang, Hierarchical SnO_2 Nanospheres: Bio-inspired Mineralization, Vulcanization, Oxidation Techniques, and the Application for NO Sensors, Sci. Rep-UK 3 (2013) 3500.

[13] W. Li, S. Ma, Y. Li, G. Yang, Y. Mao, J. Luo, D. J. Gengzang, X. Xu, S. Yan, Enhanced Ethanol Sensing Performance of Hollow ZnO–SnO_2 Core–Shell Nanofibers, Sens. Actuators B Chem. 211 (2015) 392-402.

[14] A. Kolmakov, D.O. Klenov, Y. Lilach, S. Stemmer, M. Moskovits, Enhanced Gas Sensing by Individual SnO_2 Nanowires and Nanobelts Functionalized with Pd Catalyst Particles, Nano Lett. 5 (2005) 667-673.

[15] P. Sun, X. Zhou, C. Wang, B. Wang, X. Xu, G. Lu, One-Step Synthesis and Gas Sensing Properties of Hierarchical Cd-doped SnO_2 Nanostructures, Sens. Actuators B Chem. 190 (2014) 32-39.

[16] S.H. Park, S. An, Y. Mun, C. Lee, UV-Enhanced NO_2 Gas Sensing Properties of SnO_2-Core/ZnO-Shell Nanowires at Room Temperature, ACS Appl. Mater. Interfaces 5 (2013) 4285-4292.

[17] S.W. Choi, A. Katoch, G.J. Sun, J.H. Kim, S.H. Kim, S.S. Kim, Dual Functional Sensing Mechanism in SnO_2–ZnO Core–Shell Nanowires, ACS Appl. Mater. Interfaces 6 (2014) 8281-8287.

[18] H. Huang, H. Gong, C.L. Chow, J. Guo, T.J. White, M.S. Tse, O.K. Tan, Low-Temperature

Growth of SnO_2 Nanorod Arrays and Tunable N–P–N Sensing Response of a ZnO/SnO_2 Heterojunction for Exclusive Hydrogen Sensors, Adv. Funct. Mater. 21 (2011) 2680-2686.

[19] J. Liu, M. Dai, T. Wang, P. Sun, X. Liang, G. Lu, K. Shimanoe, N. Yamazoe, Enhanced Gas Sensing Properties of SnO_2 Hollow Spheres Decorated with CeO_2 Nanoparticles Heterostructure Composite Materials, ACS Appl. Mater. Interfaces 8 (2016) 6669-6677.

[20] Y. Chen, C. Zhu, W. Jiao, P. Gao, M. Cao, X. Shi, Synthesis and Enhanced Ethanol Sensing Characteristics of α-Fe_2O_3/SnO_2 Core–Shell Nanorods, Nanotechnology 20 (2009) 045502.

[21] A. Katoch, Z.U. Abideen, H.W. Kim, S.S. Kim, Grain-Size-Tuned Highly H_2-Selective Chemiresistive Sensors Based on ZnO–SnO_2 Composite Nanofibers, ACS Appl. Mater. Interfaces 8 (2016) 2486-2494.

[22] Ü. Özgür, Y.I. Alivov, C. Liu, A. Teke, M. A. Reshchikov, S. Doğan, V. Avrutin, S. J. Cho, H. Morkoç, A Comprehensive Review of ZnO Materials and Devices, J. Appl. Phys. 98 (2005) 041301.

[23] W. Lin, Zinc Oxide Nanostructures: Growth, Properties and Applications, J. Phys.: Condens. Matter 16 (2004) R829.

[24] M. Kevin, Y.H. Fou, A.S.W. Wong, G.W. Ho, A Novel Maskless Approach Towards Aligned, Density Modulated and Multi-Junction ZnO Nanowires for Enhanced Surface Area and Light Trapping Solar Cells, Nanotechnology 21 (2010) 315602.

[25] R. Kumar, O. Al-Dossary, G. Kumar, A. Umar, Zinc Oxide Nanostructures for NO_2 Gas–Sensor Applications: A Review, Nano-Micro Lett. 7 (2015) 97-120.

[26] Q. Simon, D. Barreca, D. Bekermann, A. Gasparotto, C. Maccato, E. Comini, V. Gombac, P. Fornasiero, O.I. Lebedev, S. Turner, A. Devi, R.A. Fischer, G.V. Tendeloo, Plasma-assisted synthesis of Ag/ZnO nanocomposites: First example of photo-induced H_2 production and sensing, Int. J. Hydrogen Energy 36 (2011) 15527-15537.

[27] S. Quentin, B. Davide, G. Alberto, M. Chiara, T. Eugenio, S. Cinzia, C. Elisabetta, D.

Anjana, A.F. Roland, Ag/ZnO nanomaterials as high performance sensors for flammable and toxic gases, Nanotechnology 23 (2012) 025502

[28] D. Bekermann, A. Gasparotto, D. Barreca, C. Maccato, E. Comini, C. Sada, G. Sberveglieri, A. Devi, R.A. Fischer, Co_3O_4/ZnO Nanocomposites: From Plasma Synthesis to Gas Sensing Applications, ACS Appl. Mater. Interfaces 4 (2012) 928-934.

[29] Q. Simon, D. Barreca, A. Gasparotto, C. Maccato, E. Tondello, C. Sada, E. Comini, G. Sberveglieri, M. Banerjee, K. Xu, A. Devi, R.A. Fischer, CuO/ZnO Nanocomposite Gas Sensors Developed by a Plasma-Assisted Route, ChemPhysChem, 13 (2012) 2342-2348.

[30] H.W. Kim, Y.J. Kwon, A. Mirzaei, S.Y. Kang, M.S. Choi, J.H. Bang, S.S. Kim, Synthesis of zinc oxide semiconductors-graphene nanocomposites by microwave irradiation for application to gas sensors, Sens. Actuators B Chem. 249 (2017) 590-601.

[31] V.P. Dinesh, A. Sukhananazerin, P. Biji, An emphatic study on role of spill-over sensitization and surface defects on NO2 gas sensor properties of ultralong ZnO@Au heterojunction NRs, J. Alloys Compd. 712 (2017) 811-821.

[32] K. Diao, Y. Huang, M. Zhou, J. Zhang, Y. Tang, S. Wang, T. Liu, X. Cui, Selectively Enhanced Sensing Performance for Oxidizing Gases Based on ZnO Nanoparticle-Loaded Electrospun SnO_2 Nanotube Heterostructures, Rsc Adv. 6 (2016) 28419-28427.

[33] I.S. Hwang, S.J. Kim, J.K. Choi, J.W. Choi, H.J. Ji, G.T. Kim, G. Cao, J.H. Lee, Synthesis and Gas Sensing Characteristics of Highly Crystalline ZnO–SnO_2 Core–Shell Nanowires, Sens. Actuators B Chem. 148 (2010) 595-600.

[34] S.W. Choi, A. Katoch, G.J. Sun, S.S. Kim, Synthesis and Gas Sensing Performance of ZnO–SnO_2 Nanofiber–Nanowire Stem-Branch Heterostructure, Sens. Actuators B Chem. 181 (2013) 787-794.

[35] H.W. Kim, H.G. Na, Y.J. Kwon, H.Y. Cho, C. Lee, Decoration of Co Nanoparticles on ZnO-Branched SnO_2 Nanowires to Enhance Gas Sensing, Sens. Actuators B Chem. 219 (2015)

22-29.

[36] J.A. Park, J.H. Moon, S.J. Lee, S.H. Kim, H.Y. Chu, T.Y. Zyung, SnO_2–ZnO Hybrid Nanofibers-Based Highly Sensitive Nitrogen Dioxides Sensor, Sens. Actuators B Chem. 145 (2010) 592-595.

[37] D.J. Yang, I. Kamienchick, D.Y. Youn, A. Rothschild, I.D. Kim, Ultrasensitive and Highly Selective Gas Sensors Based on Electrospun SnO_2 Nanofibers Modified by Pd Loading, Adv. Funct. Mater. 20 (2010) 4258-4264.

[38] S.S. Kim, S. W. Choi, H. G. Na, D. S. Kwak, Y. J. Kwon, H. W. Kim, ZnO–SnO_2 Branch–Stem Nanowires Based on A Two-Step Process: Synthesis and Sensing Capability, Curr. Appl. Phys. 13 (2013) 526-532.

[39] H.G. Na, Y.J. Kwon, H.Y. Cho, S.Y. Kang, H.W. Kim, Improvement of Gas Sensing Characteristics by Adding Pt Nanoparticles on ZnO-Branched SnO_2 Nanowires, J. Nanosci. Nanotechno. 15 (2015) 8571-8576.

[40] S.W. Choi, J.Y. Park, S.S. Park, Synthesis of SnO_2–ZnO Core–Shell Nanofibers Via a Novel Two-Step Process and Their Gas Sensing Properties, Nanotechnology 20 (2009) 465603.

[41] L. Chen, S. Bai, G. Zhou, D. Li, A. Chen, C. Liu, Synthesis of ZnO–SnO_2 Nanocomposites by Microemulsion and Sensing Properties for NO_2, Sens. Actuators B Chem. 134 (2008) 360-366.

[42] J. Dai, C. Xu, J. Guo, X. Xu, G. Zhu, Y. Lin, Brush-like SnO_2/ZnO hierarchical nanostructure: Synthesis, characterization and application in UV photoresponse, AIP Adv. 3 (2013) 062108.

[43] S. Sun, G. Meng, G. Zhang, L. Zhang, Controlled growth and optical properties of one-dimensional ZnO nanostructures on SnO_2 nanobelts, Cryst. Growth Des., 7 (2007) 1988-1991.

[44] C. Cheng, B. Liu, H. Yang, W. Zhou, L. Sun, R. Chen, S. Yu, J. Zhang, H. Gong, H. Sun, H. Fan, Hierarchical Assembly of ZnO Nanostructures on SnO_2 Backbone Nanowires: Low-

Temperature Hydrothermal Preparation and Optical Properties, ACS Nano 3 (2009) 3069-3076.

[45] L. Zhu, M. Hong, G.W. Ho, Hierarchical Assembly of SnO_2/ZnO Nanostructures for Enhanced Photocatalytic Performance, Sci. Rep-UK 5 (2015) 11609.

[46] N.D. Khoang, D.D. Trung, N.V. Duy, N.D. Hoa, N.V. Hieu, Design of SnO_2/ZnO hierarchical nanostructures for enhanced ethanol gas-sensing performance, Sens. Actuators B Chem. 174 (2012) 594-601.

[47] J. Wang, N. Du, H. Zhang, J. Yu, D. Yang, Layer-by-layer assembly synthesis of ZnO/SnO_2 composite nanowire arrays as high-performance anode for lithium-ion batteries, Mater. Res. Bull. 46 (2011) 2378-2384.

[48] J. Kong, Z. Rui, H. Ji, Y. Tong, Facile synthesis of ZnO/SnO_2 hetero nanotubes with enhanced electrocatalytic property, Catal. Today 258 (2015) 75-82.

[49] Z. Liu, L. Ding, Z. Wang, Y. Mao, S. Xie, Y. Zhang, G. Li, Y. Tong, ZnO/SnO_2 hierarchical and flower-like nanostructures: facile synthesis, formation mechanism, and optical and magnetic properties, CrystEngComm 14 (2012) 2289-2295.

[50] X. Huang, L. Shang, S. Chen, J. Xia, X. Qi, X. Wang, T. Zhang, X. Meng, Type-II ZnO nanorod-SnO_2 nanoparticle heterostructures: characterization of structural, optical and photocatalytic properties, Nanoscale 5 (2013) 3828-3833.

[51] Y. Cai, X. Li, Y. Liu, S. Du, P. Cheng, F. Liu, K. Shimanoe, N. Yamazoe, G. Lu, Hollow cylinder ZnO/SnO_2 nanostructures synthesized by ultrasonic spray pyrolysis and their gas-sensing performance, CrystEngComm 16 (2014) 6135-6140.

[52] Q. Kuang, Z. Jiang, Z. Xie, S. Lin, Z. Lin, S. Xie, R. Huang, L. Zheng, Tailoring The Optical Property by A Three-Dimensional Epitaxial Heterostructure: A Case of ZnO/SnO_2, J. Am. Chem. Soc. 127 (2005) 11777-11784.

[53] W. Wang, Y. Zhu, L. Yang, ZnO–SnO_2 Hollow Spheres and Hierarchical Nanosheets: Hydrothermal Preparation, Formation Mechanism, and Photocatalytic Properties, Adv. Funct.

Mater. 17 (2007) 59-64.

[54] S. Yan, S. Ma, W. Li, X. Xu, L. Cheng, H. Song, X. Liang, Synthesis of SnO_2–ZnO heterostructured nanofibers for enhanced ethanol gas-sensing performance, Sens. Actuators B Chem. 221 (2015) 88-95.

[55] A. Katoch, J. H. Kim, Y. J. Kwon, H. W. Kim, S.S. Kim, Bifunctional Sensing Mechanism of SnO_2–ZnO Composite Nanofibers for Drastically Enhancing the Sensing Behavior in H_2 Gas, ACS Appl. Mater. Interfaces 7 (2015) 11351-11358.

[56] Z. Zhang, M. Xu, X. Ruan, J. Yan, J. Yun, W. Zhao, Y. Wang, Enhanced Radar and Infrared Compatible Stealth Properties in Hierarchical ZnO@SnO_2 Nanostructures, Ceram. Int. 43 (2017) 3443-3447.

[57] D. Briggs, M. P. Seah, Practical Surface Analysis: Auger and X-ray Photoelectron Spectroscopy, Wiley, New York, 1990.

[58] D. Bekermann, A. Gasparotto, D. Barreca, A. Devi, R. A. Fischer, p-Co_3O_4/n-ZnO, Obtained by PECVD, Analyzed by X-ray Photoelectron Spectroscopy, Surf. Sci. Spectra 18 (2011) 36-45.

[59] D. Barreca, D. Bekermann, E. Comini, A. Devi, R. A. Fischer, A. Gasparotto, C. Maccato, G. Sberveglieri, E. Tondello, 1D ZnO nano-assemblies by Plasma-CVD as chemical sensors for flammable and toxic gases, Sens. Actuators B Chem. 149 (2010) 1-7.

[60] D. Ju, H. Xu, Z. Qiu, Z. Zhang, Q. Xu, J. Zhang, J. Wang, B. Cao, Near Room Temperature, Fast-Response, and Highly Sensitive Triethylamine Sensor Assembled with Au-Loaded ZnO/SnO_2 Core–Shell Nanorods on Flat Alumina Substrates, ACS Appl. Mater. Interfaces 7 (2015) 19163-19171.

[61] Z. Zhang, C. Shao, X. Li, L. Zhang, H. Xue, C. Wang, Y. Liu, Electrospun nanofibers of ZnO−SnO_2 heterojunction with high photocatalytic activity, J. Phys. Chem. C. 114 (2010) 7920-7925.

[62] L. Xu, R. Xing, J. Song, W. Xu, H. Song, ZnO-SnO2 Nanotubes Surface Engineered by Ag Nanoparticles: Synthesis, Characterization, and Highly Enhanced Hcho Gas Sensing Properties, J. Mater. Chem. C 1 (2013) 2174-2182.

[63] J. Wang, N. Du, H. Zhang, J. Yu, D. Yang, Large-Scale Synthesis Of SnO_2 Nanotube Arrays as High-Performance Anode Materials of Li-Ion Batteries, J. Phys. Chem. C 115 (2011) 11302-11305.

[64] D. Zhang, L. Sun, G. Xu, C. Yan, Size-Controllable One-Dimensinal SnO_2 Nanocrystals: Synthesis, Growth Mechanism, and Gas Sensing Property, Phys. Chem. Chem. Phys. 8 (2006) 4874-4880.

[65] Y. Ma, Q. Xie, X. Liu, Y. Zhao, D. Zeng, L. Wang, Y. Zheng, D. Peng, Synthesis of Amorphous ZnSnO3 Double-Shell Hollow Microcubes As Advanced Anode Materials for Lithium Ion Batteries, Electrochim. Acta 182 (2015) 327-333.

[66] L. Wang, K. Tang, Z. Liu, D. Wang, J. Sheng, W. Cheng, Single-Crystalline ZnSn(OH)6 Hollow Cubes Via Self-Templated Synthesis at Room Temperature and Their Photocatalytic Properties, J. Mater. Chem. 21 (2011) 4352-4357.

[67] J. Yin, F. Gao, C. Wei, Q. Lu, Controlled Growth and Applications of Complex Metal Oxide $ZnSn(OH)_6$ Polyhedra, Inorg. Chem. 51 (2012) 10990-10995.

[68] H. Yu, R. Lai, H. Zhuang, Z. Zhang, X. Wang, Controllable Synthesis of Crystallographic Facet-Oriented Polyhedral ZnSn(OH)6 Microcrystals With Assistance of A Simple Ion, CrystEngComm 14 (2012) 8530-8535.

[69] J. A. Kerr, D. W. Stocker, CRC Handbook of Chemistry and Physics, 82th ed. CRC Press, Boca Raton, FL, 2002.

[70] H. D. B. Jenkins, H. K. Roobottom, CRC Handbook of Chemistry and Physics, 95th ed. CRC Press, Boca Raton, FL, 2014.

[71] Z. Wang, X. Kong, J. Zuo, Induced Growth of Asymmetric Nanocantilever Arrays on Polar

Surfaces, Phys. Rev. Lett. 91 (2003) 185502.

[72] J. Zhao, C. Ye, X. Fang, L. Qin, L. Zhang, Selective Growth of Crystalline SnO_2 on the Polar Surface of ZnO Nanobelts, Cryst. Growth Des. 6 (2006) 2643-2647.

[73] E.R. Leite, T.R. Giraldi, F.M. Pontes, E. Longo, A. Beltrán, J. Andrés, Crystal Growth in Colloidal Tin Oxide Nanocrystals Induced by Coalescence at Room Temperature, Appl. Phys. Lett. 83 (2003) 1566-1568.

[74] L. Vayssieres, M. Graetzel, Highly Ordered SnO_2 Nanorod Arrays from Controlled Aqueous Growth, Angew. Chem. Int. Ed. 43 (2004) 3666-3670.

[75] C.C. Yec, H. Zeng, Synthesis of Complex Nanomaterials Via Ostwald Ripening, J. Mater. Chem. A 2 (2014) 4843-4851.

[76] B. Liu, H. Zeng, Symmetric and Asymmetric Ostwald Ripening in the Fabrication of Homogeneous Core–Shell Semiconductors, Small 1 (2005) 566-571.

[77] H. Zeng, Synthetic Architecture of Interior Space for Inorganic Nanostructures, J. Mater. Chem. 16 (2006) 649-662.

[78] Q. Kuang, X. Zhou, L. Zheng, Hexagonal ZnO/SnO_2 core-Shell Micropyramids: Epitaxial Growth-Based Synthesis, Chemical Conversion, and Cathodoluminescence, Inorg. Chem. Front. 1 (2014) 186-192.

[79] Q. Kuang, T. Xu, Z. Xie, S. Lin, R. Huang, L. Zheng, Versatile Fabrication of Aligned SnO_2 Nanotube Arrays by Using Various ZnO Arrays as Sacrificial Templates, J. Mater. Chem. 19 (2009) 1019-1023.

[80] N.N. Nashaat, Asphaltene Adsorption onto Alumina Nanoparticles: Kinetics and Thermodynamic Studies, Energy Fuels 24 (2010) 4116-4122.

[81] W.B. Weir, Automatic measurement of complex dielectric constant and permeability at microwave frequencies, P. IEEE 62 (1974) 33-36.

[82] N. Yamazoe, New Approaches for Improving Semiconductor Gas Sensors, Sens. Actuators

B Chem. 5 (1991) 7-19.

[83] F. Yang, J. Zhu, X, Zou, X. Pang, R. Yang, S. Chen, Y. Fang, T. Shao, X. Luo, L. Zhang, Three-dimensional TiO_2/SiO_2 composite aerogel films via atomic layer deposition with enhanced H_2S gas sensing performance, Ceram. Int, 44(2018) 1078-1085.

[84] L. Zhua, K. Yuan, J. Yang, H. Ma, T. Wang, X. Ji, J. Feng, A. Devi, H. Lu, Fabrication of heterostructured p-CuO/n-SnO_2 core-shell nanowires for enhanced sensitive and selective formaldehyde detection, Sens. Actuators B Chem. 209 (2019) 233-241.

[85] S. Lee, V. Galstyan, A. Ponzoni, I.G. Juan, R. Riedel, M.A. Dourges, Y. Nicolas, T. Toupance, Finely Tuned SnO_2 Nanoparticles for Efficient Detection of Reducing and Oxidizing Gases: The Influence of Alkali Metal Cation on GasSensing Properties, ACS Appl. Mater. Interfaces 10 (2018) 10173−10184.

[86] J.H. Kim, S.S. Kim, Realization of ppb-Scale Toluene-Sensing Abilities with Pt-Functionalized SnO_2–ZnO Core–Shell Nanowires, ACS Appl. Mater. Interfaces 7 (2015) 17199-17208.

[87] V.V. Sysoev, J. Goschnick, T. Schneider, E. Strelcov, A. Kolmakov, A Gradient Microarray Electronic Nose Based on Percolating SnO_2 Nanowire Sensing Elements, Nano Lett. 7 (2007) 3182-3188.

[88] T. Rakshit, S. Santra, I. Manna, S.K. Ray, Enhanced Sensitivity and Selectivity of Brush-Like SnO_2 Nanowire/ZnO Nanorod Heterostructure Based Sensors for Volatile Organic Compounds, Rsc Adv. 4 (2014) 36749-36756.

2.7. Supplementary Data

Design of Novel ZnO@SnO_2 n-n Heterostructures for Highly Sensitive NO2 Sensing

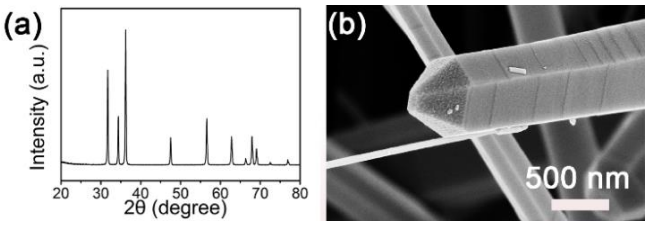

Figure S 2.1 (a) XRD and (b) SEM image of ZnO nanorod.

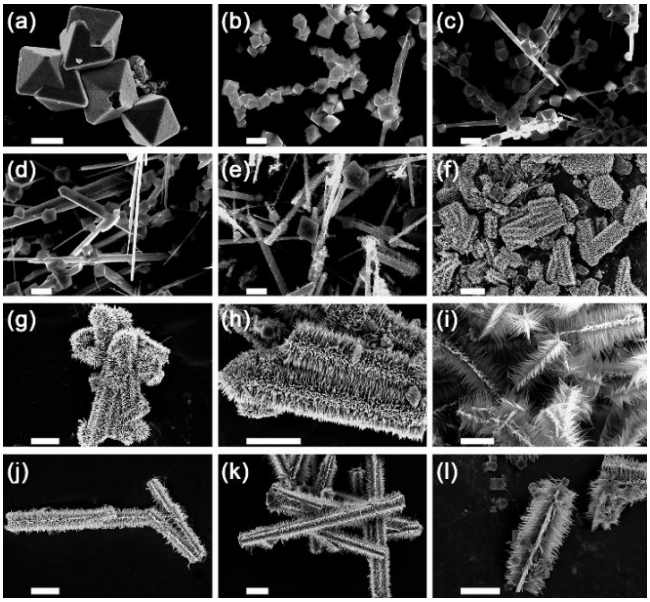

Figure S 2.2 The SEM images (Scale bars, 2 μm) of B-ZnO@SnO_2 HNSs at 200 °C with different reaction time: (a) 15, (b) 30 min, (c) 1, (d) 2, (e) 4, (f) 6, (g) 8, (h) 10, (i) 12, (j) 16, (k) 20, (l) 24 h.

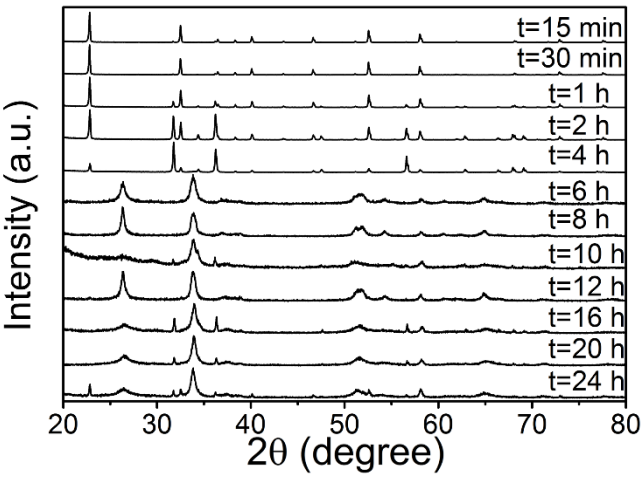

Figure S 2.3 The XRD patterns of B-ZnO@SnO_2 HNSs at 200 °C for different reaction time.

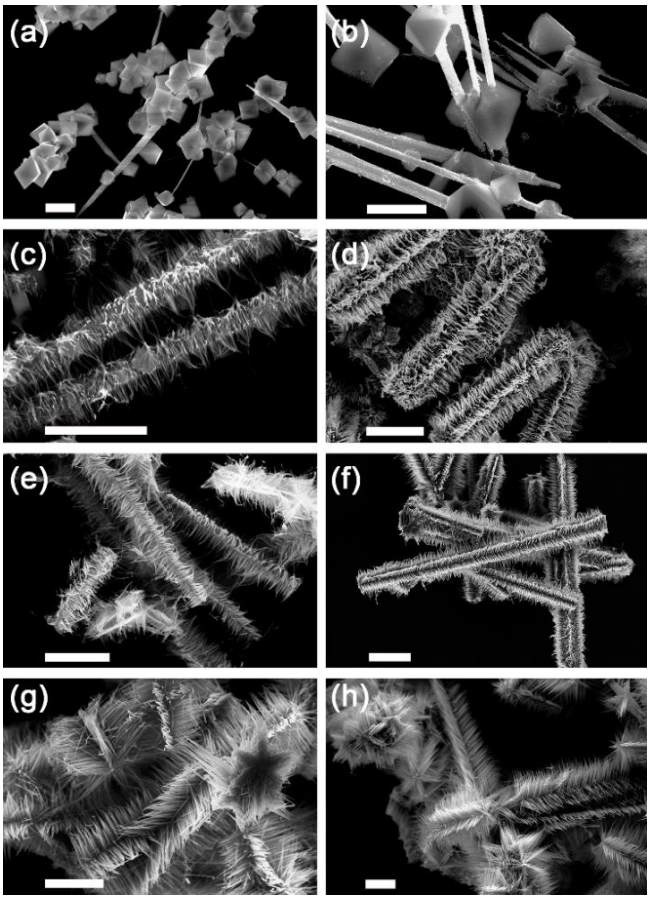

Figure S 2.4 The SEM images (Scale bars, 2 μm) of B-ZnO@SnO_2 HNSs with different reaction temperature: (a) 160, (b) 170, (c) 180, (d) 190, (e) 195, (f) 200, (g) 205, (h) 210 °C for 20 h.

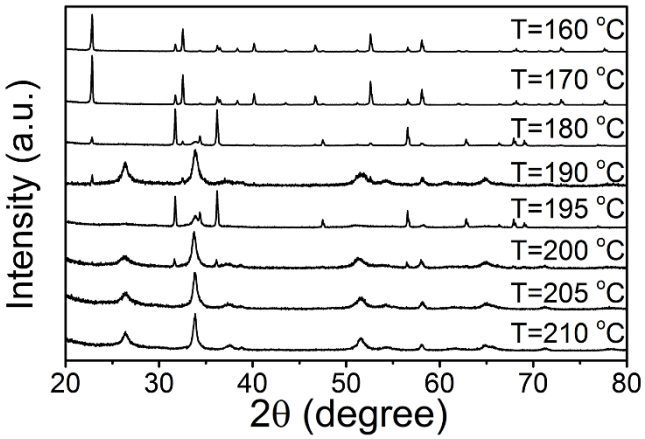

Figure S 2.5The XRD patterns of B-ZnO@SnO_2 HNSs at 200 °C with different reaction temperature.

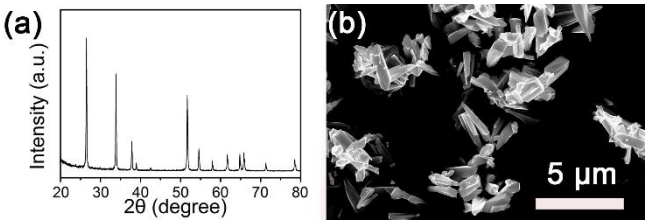

Figure S 2.6 (a) XRD and (b) SEM image of SnO_2 nanowires.

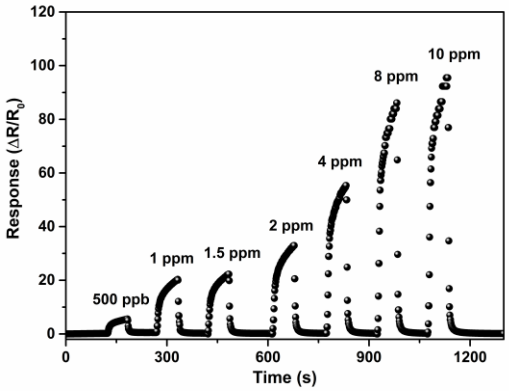

Figure S 2.7 (a) Real–time response of the B-ZnO@SnO_2 HNSs sensor to NO_2 from 500 ppb to 10 ppm over 7 months.

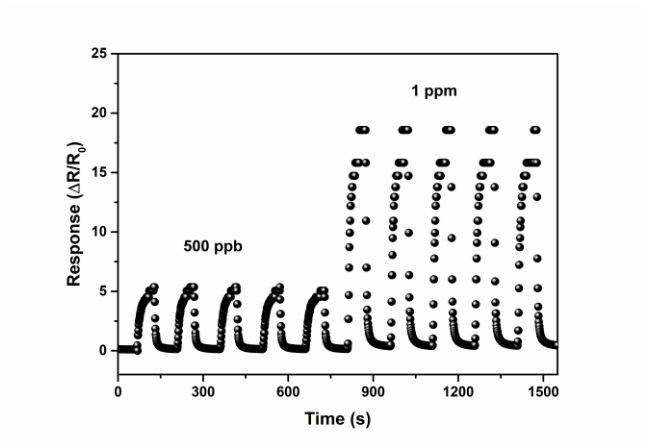

Figure S 2.8 Reproducibility characterization of the B-ZnO@SnO_2 HNSs based sensor to 500 ppb and 1 ppm NO_2 over 7 months.

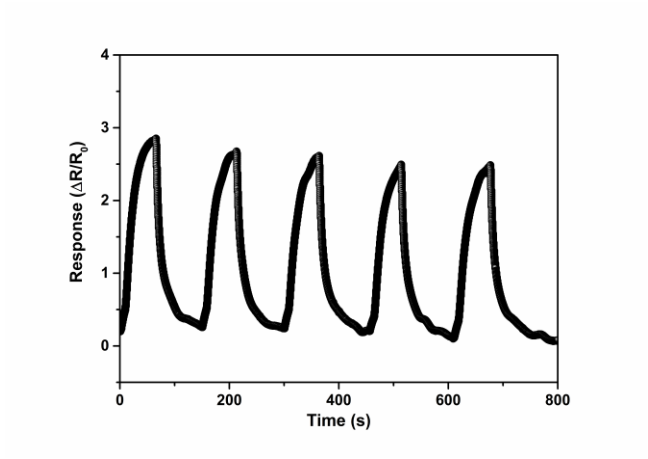

Figure S 2.9 Reproducibility characterization of the B-ZnO@SnO_2 HNSs based sensor under the relative humidity of 85% over 7 months.

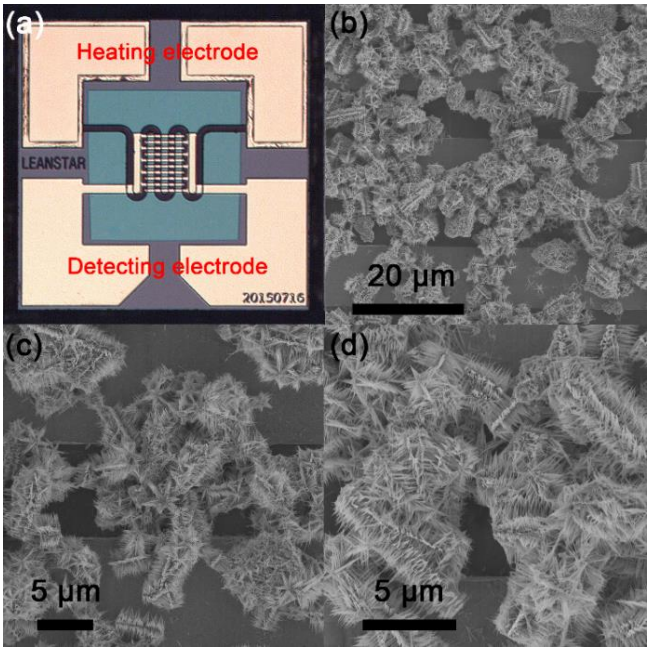

Figure S 2.10 (a) Optical photograph of the micro hotplate. (b) SEM images of the B-ZnO@SnO_2 HNSs sensor and (c–d) the B-ZnO@SnO_2 HNSs bridging the two electrodes.

Table S 0.1 NO_2 gas sensing abilities of SnO_2-ZnO composite materials.

Materials	MDL (ppm)	C (ppm)	T (˚C)	Response (R_g/R_a)	$T_{response}$ (S)	$T_{recover}$ (S)	Reference
SnO_2-ZnO NWs	1	5	RT	6.1	100	220	[16]
SnO_2-ZnO NWs	10	10	300	~50	—	—	[17]
ZnO-SnO_2 HSs	0.5	5	300	30.8	~500	~240	[32]
ZnO-SnO_2 NWs	0.5	10	200	66.3	~50	~60	[33]
ZnO-SnO_2 NWs	0.1	1	300	~26	—	—	[34]
ZnO-SnO_2 NWs	1	10	250	4.3	317	343	[35]
SnO_2-ZnO NFs	0.4	4	200	105	—	—	[36]
ZnO-SnO_2 NWs	0.5	1	250	~3	—	—	[38]
ZnO-SnO_2 NWs	2	2	250	1.5	303	473	[39]
ZnO-SnO_2 NWs	1	5	300	0.4	—	—	[40]

ZnO-SnO_2 NCs	200	500	250	34.5	—	—	[41]
B-ZnO@SnO_2 HNSs	0.005	0.005	150	1.2	45	60	This work
	0.005	10	150	106.0	50	55	This work

References:

[16] S.H. Park, S.Y. An, Y.H. Mun, C.M. Lee, UV-Enhanced NO_2 Gas Sensing Properties of SnO_2-Core/ZnO-Shell Nanowires at Room Temperature, ACS Appl. Mater. Interfaces, 5 (2013) 4285-4292.

[17] S.W. Choi, A. Katoch, G.J. Sun, J.H. Kim, S.H. Kim, S.S. Kim, Dual Functional Sensing Mechanism in SnO_2–ZnO Core–Shell Nanowires, ACS Appl. Mater. Interfaces, 6 (2014) 8281-8287.

[32] K. Diao, Y. Huang, M. Zhou, J. Zhang, Y. Tang, S. Wang, T. Liu, X. Cui, Selectively Enhanced Sensing Performance for Oxidizing Gases Based on ZnO Nanoparticle-Loaded Electrospun SnO_2 Nanotube Heterostructures, Rsc Adv., 6 (2016) 28419-28427. [33] I.S. Hwang, S.J. Kim, J.K. Choi, J.W. Choi, H.j. Ji, G.T. Kim, G.Z. Cao, J.H. Lee, Synthesis and Gas Sensing Characteristics of Highly Crystalline ZnO–SnO_2 Core–Shell Nanowires, Sensor. Actuat. B, 148 (2010) 595-600.

[34] S.W. Choi, A. Katoch, G.J. Sun, S.S. Kim, Synthesis and Gas Sensing Performance of ZnO–SnO_2 Nanofiber–Nanowire Stem-Branch Heterostructure, Sensor. Actuat. B, 181 (2013) 787-794.

[35] H.W. Kim, H.G. Na, Y.J. Kwon, H.Y. Cho, C. Lee, Decoration of Co Nanoparticles on ZnO-Branched SnO_2 Nanowires to Enhance Gas Sensing, Sensor. Actuat. B, 219 (2015) 22-29.

[36] J.A. Park, J.H. Moon, S.J. Lee, S.H. Kim, H.Y. Chu, T.Y. Zyung, SnO_2–ZnO Hybrid Nanofibers-Based Highly Sensitive Nitrogen Dioxides Sensor, Sensor. Actuat. B, 145 (2010)

592-595.

[38] S.S. Kim, S.W. Choi, H.G. Na, D.S. Kwak, Y.J. Kwon, H.W. Kim, ZnO–SnO_2 Branch–Stem Nanowires Based on A Two-Step Process: Synthesis and Sensing Capability, Curr. Appl. Phys., 13 (2013) 526-532.

[39] H.G. Na, Y.J. Kwon, H.Y. Cho, S.Y. Kang, H.W. Kim, Improvement of Gas Sensing Characteristics by Adding Pt Nanoparticles on ZnO-Branched SnO_2 Nanowires, J. Nanosci. Nanotechno., 15 (2015) 8571-8576.

[40] C. Sun-Woo, P. Jae Young, K. Sang Sub, Synthesis of SnO_2–ZnO Core–Shell Nanofibers Via a Novel Two-Step Process and Their Gas Sensing Properties, Nanotechnology, 20 (2009) 465603

[41] L. Chen, S. Bai, G. Zhou, D. Li, A. Chen, C.C. Liu, Synthesis of ZnO–SnO_2 Nanocomposites by Microemulsion and Sensing Properties for NO_2, Sensor. Actuat. B, 134 (2008) 360-366.

This page intentionally left blank

Chapter 3: In situ Growth of NiO@SnO_2 p-n Heterostructures for High Performance H_2S Sensing

3.1. Abstract

Heterostructural metal oxides with high specific surface area are crucial for constructing high performance gas sensors. However, using slurry-coating and screen-printing methods to fabricate gas sensors cannot result in high uniformity of the sensors as reported in Chapter 2. Here, NiO nanowalls decorated by SnO_2 nanoneedles (NiO@SnO_2) were in situ grown on ceramic microchips via a chemical bath deposition method to obtain highly uniform NiO@SnO_2 p-n hierarchical nanostructures (HNSs) for H_2S sensing instead of slurry-coating method. The morphologies and compositions of the NiO@SnO_2 HNSs were well tuned by varying the growth time of the NiO@SnO_2 HNSs to optimize the sensing performance. The response of the NiO@SnO_2 HNSs (2 h) to 1 ppm H_2S was over 23 times higher than that of the pure NiO nanowalls and 17 times higher than that of the pure SnO_2 nanosheets. This dramatic enhancement is mainly due to the large surface area of the NiO@SnO_2 HNSs and the p-n heterojunction at the interface of SnO_2 and NiO. The variation in the depletion layers (W_{SnO_2} and W_{NiO}) at the interface of SnO_2 and NiO greatly depends on the properties of the target gases (*e.g.*, electron-withdrawing property (NO_2) or electron-donating property (H_2S)).

Author contributions: Lin Liu has got the permission from other co-authors for this paper to her thesis. All the paper work and data analysis are finished by Lin Liu and most of the data including SEM, EDXS, sensing performance are also collected by Lin Liu.

3.2 Introductions

Hydrogen sulfide (H_2S) is a toxic, corrosive, and flammable gas that causes air pollution and is harmful to human health. An individual's blood lactate concentration will increase when exposed to 5-10 ppm H_2S, and more symptoms, such as olfactory paralysis, respiratory distress, and even death, will appear with further increases in the H_2S concentration [1]. There is a great demand for highly sensitive, selective and stable gas sensors for detecting trace concentrations of H_2S. Recently, much effort has been devoted to developing high-performance gas sensors based on semiconducting metal oxides. Their performance highly depends on the specific surface area and chemical composition of the sensing materials [2-4]. Therefore, many nanostructured metal oxides with high specific surface area have been developed (*e.g.*, SnO_2 [5,6], NiO [7-9], CuO [8], Fe_2O_3 [9], WO_3 [10], and ZnO [10]). Among them, SnO_2 (E_g = 3.5 eV), a typical n-type semiconductor that is widely used in commercial semiconducting gas sensors, has attracted significant attention due to its high chemical stability and excellent electrical properties [11]. Generally, constructing heterostructural nanomaterials can significantly enhance sensing performance due to the synergistic effects induced by the heterojunction, which can efficiently modulate conduction channels [11-14]. For example, Ji et al. [15] studied a high-performance room-temperature (RT) NO_2 sensor based on an ultrathin heterojunction film (1 nm diphenyl perylene tetracarboxylic diimide (PTCDI-Ph)/5 nm para-hexaphenyl (p-6P)), and the high sensing response was mainly due to the accumulated electrons in the PTCDI-Ph layer caused by the heterojunction. Choi et al. [11] modified SnO_2 nanowires with p-type Cr_2O_3 nanoparticles and demonstrated an enhanced response toward reducing gases by efficiently modulating the conduction channel of the SnO_2 nanowires. Notably, NiO is an ideal p-type semiconductor (Eg = 4.4 eV) that can form a type-II p-n heterojunction with SnO_2 to facilitate carrier transportation due to the difference in the working functions of SnO_2 ($\Phi_{(SnO2)}$ = 4.9 eV) and NiO ($\Phi_{(NiO)}$ = 5.3 eV) [11,16,17].

To date, the most common fabrication methods for gas sensors are slurry-coating or screen-printing the sensing materials onto the electrodes of the sensor chips [18,23]. However, these methods may affect the sensitivity, stability, and reproducibility of the sensors [9,12,23]. First, the sensing materials easily aggregate during the slurry and printing processes, which can significantly reduce the specific surface area of the sensing materials and lead to low sensitivity. Second, the relatively poor interconnection between the sensing materials and electrodes can affect the long-term stability of the sensors. Moreover, the reproducibility of the sensors is not controllable due to the inhomogeneity of the sensing materials. Several reports have demonstrated relatively controllable fabrication methods for sensing materials, such as chemical vapor deposition (CVD), oblique angle deposition (OAD), pulsed laser deposition (PLD), magnetron sputtering, and coelectrospinning fabrication [10,13,24-26]. For example, Fang et al. [27] and Tyagi et al. [25] developed a radio-frequency (RF) magnetron sputtering method to construct gas sensors with a heterojunction film. Xu et al. [13] fabricated NiO@ZnO heterostructural nanotubes based on a coelectrospinning setup including a high-voltage power supply, a syringe pump, and a coaxial spinneret. However, these methods are usually expensive and often require complex instruments and high fabrication temperatures. Therefore, a cost-effective method to fabricate heterostructural nanomaterials and construct gas sensors with high sensitivity, stability and uniformity is urgently needed.

Here, we developed a novel method for in situ growth of highly uniform NiO@SnO_2 hierarchical nanostructures (NiO@SnO_2 HNSs) on sensor chips for H_2S detection. In comparison with metal oxide-based gas sensors prepared by the slurry-coating method, this fabrication process does not involve a binder and avoids additional contamination. Briefly, the $Ni(OH)_2$ nanowalls were first grown onto a sensor chip via a chemical bath deposition method. Then, in situ growth of the SnO_2 nanoneedles onto the surface of the $Ni(OH)_2$ nanowalls was performed by immersing the chip into a SnF_2 solution. The morphology and composition of

the $Ni(OH)_2$@SnO_2 HNSs were well controlled by tuning the reaction time. The NiO@SnO_2 NHSs were obtained by annealing the obtained $Ni(OH)_2$@SnO_2 HNSs at 400 °C under an Ar atmosphere. The resulting sensor based on NiO@SnO_2 NHSs shows a high sensitivity and selectivity to H_2S (0.1 – 50 ppm).

3.3 Experimental Sections

3.3.1 Synthesis of Material

All reagents (Sinopharm Chemical Reagent Co., Ltd) were analytical grade and used without further purification. The sensor chips were pre-treated by sequential sonication in 1 M HCl solution, deionized (DI) water and absolute ethanol for 5 min, respectively. The $Ni(OH)_2$ nanowalls were directly growing on the sensor chip via a chemical bath deposition method [28]. Briefly, 0.75 mmol $NiCl_2$ (≥96.0%), 4 mmol NH_4Cl (≥99.5%), and 1.375 mmol NaOH (≥96.0%) were dissolved in 20 mL DI water. The sensor chips were inserted into the solution with the working electrode surface facing down and then placed in an oven at 55 °C for 15 h. Then the resulted chips with $Ni(OH)_2$ nanowalls were washed with DI water and ethanol. Different morphologies and compositions of $Ni(OH)_2$@SnO_2 HNSs were obtained by immersing the $Ni(OH)_2$ covered chips into a 25 mM SnF_2 solution at 90 °C and varying the growth time (2, 4, 8, and 12 h). The annealing treatment was conducted in a tubular furnace at 400 °C for 2 h under an Ar atmosphere to obtain NiO@SnO_2 HNSs. For comparison, sensors based on pure NiO nanowalls (reaction time 15 h) and SnO_2 nanosheets (reaction time 24 h) were also prepared and tested.

The SEM, EDXS and XRD samples were obtained by directly growing the materials on the silicon substrate before and after annealing treatment. The TEM samples were prepared by using Cu film to slightly scrape the silicon substrate after spraying the ethanol solution.

3.3.2. Characterization

The chemical composition of the synthesized materials was characterized by X-ray Diffraction (XRD, Bruker AXS, D8 Advance). Scanning electron microscopy (SEM, Hitachi-s4800) and transmission electron microscopy (TEM, Tecnai G2 F20 S-Twin) were also used to analyse the morphology and crystal structure of samples. Energy dispersive spectrometry (EDXS) was used to further verify the component of hierarchical nanostructures.

3.3.3. Gas Sensing Measurement

The as-prepared sensors were placed into a sealed glass chamber (1 cm^3) with an air inlet and outlet for targeted gases detection. The different concentrations of target gases were controlled by tuning the ratio of dry air and target gases via mass flow controllers (MFC, BEIJING SEVENSTAR ELECTRONICS CO., LTD). The dry air was switched to flow through the sealed glass chamber after exposure to a known concentration of target analyte until it reaches its initial resistance baseline.

3.4. Results and Discussions

3.4.1. Structure and Morphology Characterization

Figure 3.1a illustrates a schematic diagram of the ceramic sensor chip, from the bottom to top, including the heating electrodes (I), Pt layer, ceramic layer and working electrodes (II). The schematic graphs of the ceramic sensor chip after the growth of the $Ni(OH)_2$ nanowalls and $Ni(OH)_2$@SnO_2 HNSs (2 h) are displayed in Figure 3.1b and Figure 3.1c, respectively. Figure 3.1d-i shows a series of SEM images of the pure SnO_2 nanosheets (24 h), $Ni(OH)_2$ nanowalls, and $Ni(OH)_2$@SnO_2 HNSs. The $Ni(OH)_2$ nanowalls had a smooth surface with sharp edges. The thickness of the $Ni(OH)_2$ nanowalls was 10 - 20 nm, while that of the SnO_2 nanosheets was much less (< 10 nm, Figure 3.1d). After immersing the sensor chips covered with $Ni(OH)_2$ nanowalls into the SnF_2 solution, the $Ni(OH)_2$ nanowalls served as frameworks for growth of the SnO_2 nanoneedles. The size of the SnO_2 nanoneedles gradually increased

(from nanoneedles to nanosheets) by increasing the growth time. The $Ni(OH)_2$ nanowalls were densely covered by the SnO_2 nanosheets after 12 h (Figure 3.1i). The annealing treatment did not affect the morphology of the prepared hierarchical nanostructures (as depicted in the SEM images in Figure S3.1).

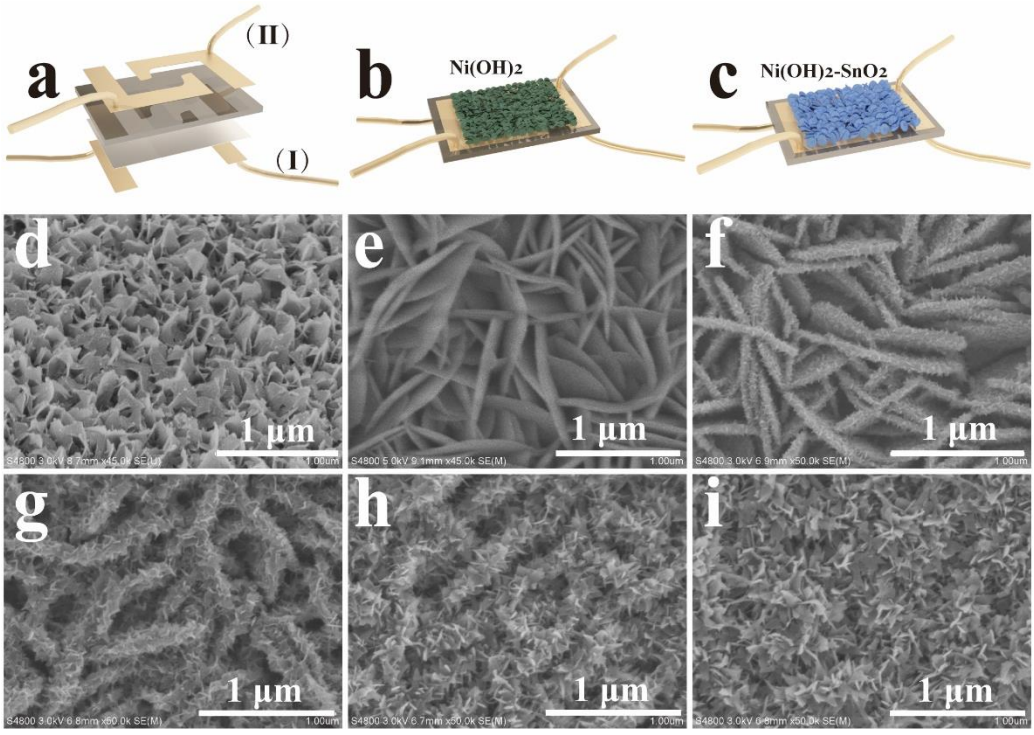

Figure 3.1Schematic diagrams of the bare ceramic microchip (a), with $Ni(OH)_2$ nanowalls (b), and $Ni(OH)_2$@SnO_2 hierarchical nanostructures (HNSs) (2 h) (c); SEM images of pure SnO_2 (d) and NiO (e), SEM images of $Ni(OH)_2$@SnO_2 HNSs with different reaction time: (f) 2 h, (g) 4 h, (h) 8 h and (i) 12 h.

Figure 3.2a reveals the X-ray diffraction patterns of $Ni(OH)_2$, SnO_2 and $Ni(OH)_2$@SnO_2 HNSs grown at different times. In the XRD pattern of $Ni(OH)_2$, there are some diagnostic diffraction peaks located at 2θ = 33.07°, 38.54°, 59.05°, and 62.73°, which correspond to the (100), (101), (110) and (111) planes of $Ni(OH)_2$ (JCPDS file No. 14-0227), respectively. The diffraction peaks of $Ni(OH)_2$ gradually decreased as the $Ni(OH)_2$ nanowalls were gradually covered by SnO_2 with the growth time increasing. To verify this result, EDXS was conducted to determine the mass ratio of Ni and Sn atoms, as shown in Table S1. The amount of Ni

decreased from 47.1% to 1.4% as the growth time of the ($Ni(OH)_2$@SnO_2 HNSs increased from 2 h to 12 h. To further confirm the crystal structure of SnO_2, pure SnO_2 nanosheets (24 h) were scraped from the PET substrate and characterized by XRD. All of the diffraction peaks were well indexed to the standard SnO_2 JCPDS card No. 41-1445 (Figure S3.2) [30]. The pure $Ni(OH)_2$ nanowalls with smooth surfaces were characterized by TEM, as shown in Figure 3.2b and c. Figure 3.2c shows the high-resolution TEM (HRTEM) image and the corresponding fast Fourier transform (FFT) image (taken from the marked box area) of the $Ni(OH)_2$ nanowalls. The lattice space of 2.7 Å matches well with the d value of the (100) crystal plane of β–$Ni(OH)_2$ [28,31]. Figure 3.2d and e illustrate the TEM images of the $Ni(OH)_2$@SnO_2 HNSs (2 h). Obviously, SnO_2 nanograins and nanoneedles were observed on the surface of the $Ni(OH)_2$ nanowalls (Figure 3.2d and e). The HRTEM image and the FFT image (taken from selected area) of the SnO_2 nanoneedle at the edge of a piece of $Ni(OH)_2$ nanowall (2 h sample) further confirm the single crystalline structure of the SnO_2 nanoneedles. The corresponding lattice spaces of 3.14 Å and 3.34 Å are consistent with the (001) and (110) crystal planes of tetragonal rutile SnO_2, respectively [21,32,33].

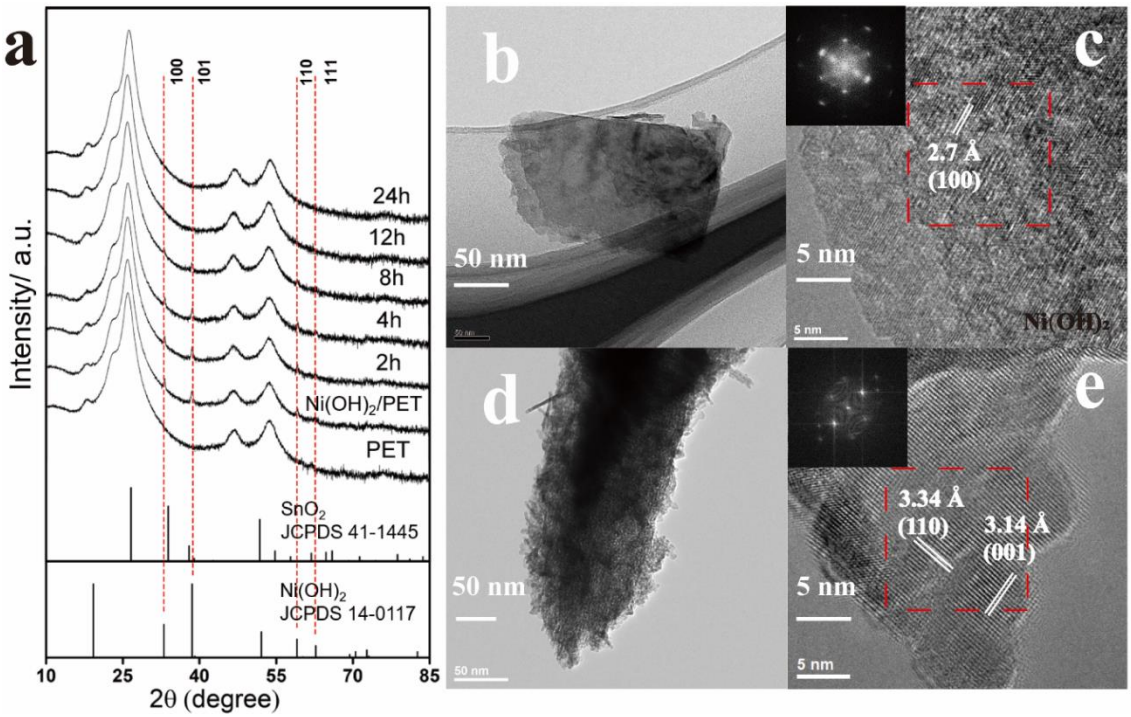

Figure 3.2 (a) XRD patterns of the prepared $Ni(OH)_2$, SnO_2, and different $Ni(OH)_2$@SnO_2 HNSs and PET substrate; (b) TEM, and (c) HRTEM and the corresponding fast Fourier transform (FFT) of $Ni(OH)_2$ nanowall; (d) TEM, and HRTEM and the corresponding fast Fourier transform (FFT) images of SnO_2 nanoneedle (2 h) at the edge of $Ni(OH)_2$ nanowall.

3.4.2. Growth Mechanism of the $Ni(OH)_2$@SnO_2 HNSs

To understand the growth mechanism, $Ni(OH)_2$@SnO_2 HNSs with different growth times were obtained and characterized with SEM (Figure S3.3). First, the $Ni(OH)_2$ nanowalls were grown on silicon substrates, which serve as the framework for growing the SnO_2 nanoneedles. The growth of the $Ni(OH)_2$ nanowalls mainly occurs through the following two steps: heterogeneous nucleation and oriented crystal growth [28]. The formation of oriented $Ni(OH)_2$ nanowalls (Figure 3.3a and Figure S3.3a) is ascribed to the selected absorption of NH_3 molecules on a specific crystal face (001) of $Ni(OH)_2$ via hydrogen bonds, which can dramatically suppress the growth of the (001) facet [34]. In this work, the formation of SnO_2 also experiences similar steps: heterogeneous nucleation and oriented crystal growth of SnO_2

nanoneedles and nanosheets [35,36]. During the early stage (0-1 h), the surface of the $Ni(OH)_2$ nanowalls became coarse and formed numerous small SnO_2 nanocrystals (Figure 3.3b and c, and Figure S3.3b and c) owing to the hydrolysis of SnF_2, the oxidization of Sn(II) to Sn(IV), and the heterogeneous nucleation process [37,38]. The needle-like morphology was observed after growth for 2 h and was attributed to the "oriented attachment" growth process (Figure 3.3d and Figure S3.3d) [39]. Subsequently, SnO_2 nanosheets formed due to the fast oriented attachment when prolonging the growth time to 4 h and 8 h. It has been reported that fluoride ions (F^-) play an important role in tuning the architectural structure and shape of SnO_2, and only when the atom ratio value of F and Sn is $R_{F/Sn} = 2$ can SnO_2 nanosheets be obtained [36]. The surface free energy of the SnO_2 facet can be tuned owing to the absorption and passivation effect of F^- on the surface of the SnO_2 nanocrystals ((001) > (110) > (113) > (102)) [40].

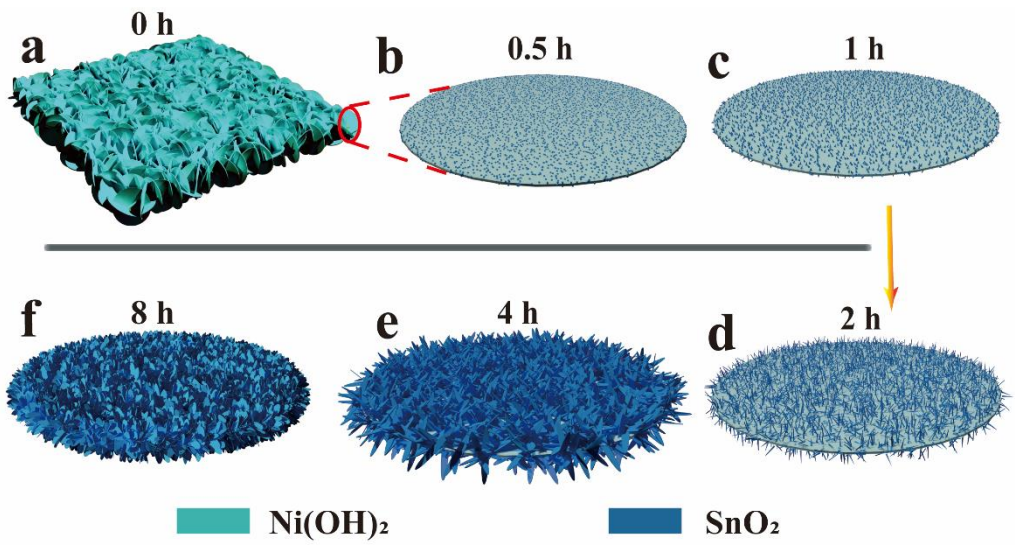

Figure 3.3 Schematic graph of the proposed growth processes of $Ni(OH)_2$@SnO_2 HNSs.

3.4.3. Gas-sensing Performance of NiO@SnO_2 HNSs

The effect of hierarchical nanostructures on the sensing performance of the sensors was studied. The sensing properties of different sensors based on NiO@SnO_2 HNSs (2, 4, 8, and 12 h), pure NiO nanowalls, and SnO_2 nanosheets are shown in Figure 3.4. In this case, the sensing response (S) was defined by $\Delta R/R_a$ (reducing gases) or $\Delta R/R_g$ (oxidizing gases), where

ΔR is the difference between the resistance in the target gas (R_g) and in air (R_a). Figure 3.4a illustrates the sensing response based on NiO@SnO_2 HNSs (2 h) at different operating temperatures (180 - 300 °C) to 1 ppm H_2S. The response increased with increasing operating temperature, reached a maximum value at 240 °C (termed the optimal operating temperature) and then gradually decreased as the temperature further increased. The influence of temperature is ascribed to the possible competition between the adsorption and desorption rates of H_2S and the surface reactivity of the adsorbed H_2S molecules and adsorbed oxygen species [41,42]. Increasing the operating temperature improves the H_2S chemisorption and the reaction rate, which can lead to an enhanced response [41,42]. However, with further increases in temperature, the desorption of H_2S outweighs the effect of absorption, resulting in a decrease in the response [41,42]. Based on this result, all other measurements were conducted at 240 °C. The sensing responses of sensors (2, 4, 8, 12 h, NiO and SnO_2) to different H_2S concentrations (0.2 -1 ppm) are shown in Figure 3.4b. The sensor based on NiO@SnO_2 HNSs (2 h) has the highest response because the sensing response of the sensors highly depends on the heterojunction of SnO_2 and NiO. (A more detailed sensing mechanism is discussed in the next section.)

Selectivity is an important parameter to judge the sensing performance of gas sensors. The response of the sensors (2, 4, 8, and 12 h) toward different gases, including NH_3, C_7H_8, CHOH, NO_2 and H_2S, at the same concentration (0.5 ppm) was tested, as shown in Figure 3.4c. All of the NiO@SnO_2 HNS-based sensors showed good selectivity to H_2S against other interfering gases. However, compared with other sensors, NiO@SnO_2 HNSs (2 h)-based sensors exhibited an ultrahigh response and selectivity toward H_2S. The sensing responses of the sensor (2 h) to NH_3, C_7H_8, CHOH, NO_2 and H_2S were 0.1, 0.21, 0.05, -0.09 and 1.86, respectively. In addition, the sensor prepared with the NiO@SnO_2 HNSs (2 h) showed a broad linear detection range (R^2 = 0.998, slope of 3.66 ppm^{-1}) from 0.1 ppm to 50 ppm, as shown in Figure 3.4d and e. The

theoretical detection limit (DL) toward H_2S was estimated to be 1.5 ppb, exceeding the requirement of the US EPA (83 ppb), according to equations (Eq (3-1) and Eq (3-2)) [42-45],

$$RMS_{noise} = \sqrt{\frac{SD^2}{N}} \quad (3\text{-}1)$$

$$\mathrm{DL} = 3\frac{RMS_{noise}}{slop} \quad (3\text{-}2)$$

The standard deviation (*SD* = 0.018) was obtained from 100 baseline data points in Figure 3.4d before exposure to H_2S. Therefore, the sensor noise (RMS_{noise}) was 0.0018, and the theoretical DL was approximately 1.5 ppb. The sensor based on the NiO@SnO_2 HNSs (2 h) also showed afast response and recovery of 37 s and 50 s (1 ppm H_2S), respectively, as shown in Figure 3.4f. Moreover, the sensing response of the sensor toward 1 ppm H_2S changed less than 3% after one month, indicating good stability and repeatability. The sensing response in this work is very high with fast response and recovery times. This work shows a higher sensing performance with fast response and recovery times and high sensing response compared with other reported H_2S sensors based on the NiO-SnO_2 system and NiO- and SnO_2-based composites in recent years (Table S3.2).

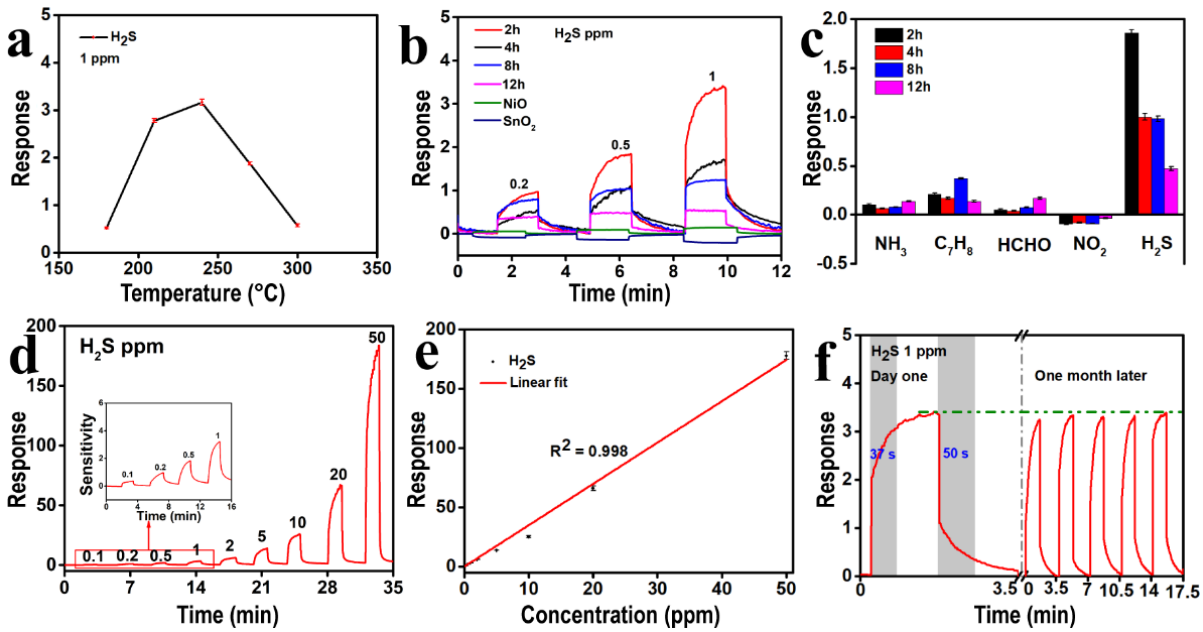

Figure 3.4 (a) Operating temperature dependence sensing response of NiO@SnO_2 HNS (2 h)-based sensor to 1 ppm H_2S; (b) Real-time response of sensors based on different NiO@SnO_2 HNSs (2, 4, 8, and 12 h), pure NiO nanowalls and pure SnO_2 nanosheets to different concentration of H_2S (ranging from 0.2 to 1 ppm); (c) Selectivity of sensors 2, 4, 8, and 12 h) to different gases with same concentration (0.5 ppm); (d) Real-time response of the sensor based on NiO@SnO_2 HNSs (2 h) to different concentration of H_2S (0.1 – 50 ppm) and (e) linear relationship of sensing response verse different concentration of H_2S; (f) Sensing response of sensor (2 h) to 1 ppm H_2S of day one and one month later.

3.4.4. Gas Sensing Mechanism of NiO@SnO_2 HNSs

For the pure SnO_2 nanosheets (24 h), the conduction property of SnO_2 depends on the concentration of electrons in SnO_2. When exposed to air, oxygen molecules adsorb onto the surface of SnO_2 in the form of oxygen ions such as O_2^- and O^- by extracting electrons from SnO_2 and forming a depleted layer on the surface of the SnO_2 nanosheets. When switching to H_2S, the chemisorbed H_2S will react with the adsorbed oxygen ions and release electrons to the SnO_2 nanosheets as follows [41,46,47]:

$$O_{2(g)} + e^- \rightarrow O_{2(ads)}^- \quad (3\text{-}3)$$

$$2H_2S + 3O_{2(ads)} \rightarrow 2H_2O + 2SO_2 + 3e^- \quad (3\text{-}4)$$

Thus, the resistance of the SnO_2 nanosheets decreases, and this trend opposites to that of pure NiO nanowalls, as it is a p-type semiconductor. Compared with pure NiO and SnO_2, the enhanced sensing performance of NiO@SnO_2 HNSs is mainly ascribed to two aspects: a) large specific surface area and b) the formed p-n heterojunction. The decorated SnO_2 nanoneedles can greatly increase the surface area of NiO@SnO_2 HNSs, leading to high sensitivity. In addition, the resistance of sensors based on heterogeneous materials also depends on the potential barrier height according to Eq (3-5) [2, 48, 49]:

$$R = R_0\, exp\left(\frac{qV}{kT}\right) \quad (3\text{-}5)$$

where R is the resistance of the material, R_0 is the initial resistance, q is the charge of an electron, k is Boltzmann's constant, T is the absolute temperature and V is the potential barrier height (including the heterojunction potential barrier (V_0) and the homojunction potential barrier). Therefore, the resistance of the sensors will exponentially change with V, which is why the sensing performance of NiO@SnO_2 HNSs is much better than that of pure NiO and SnO_2 [2, 49].

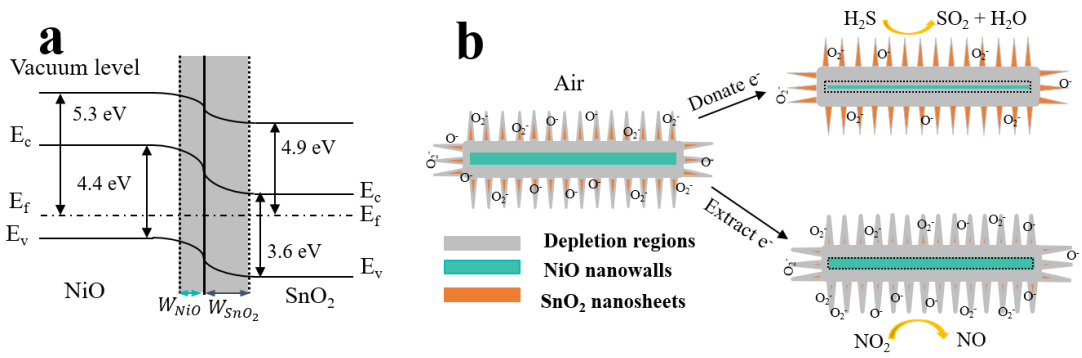

Figure 3.5 (a) Schematic band gap structure of NiO@SnO_2 p-n heterojunction; (b) Schematics show changes of the conduction channel when exposure to different gases such as air, H_2S, and NO_2.

The schematic of the sensing mechanism and the relevant energy band diagram are shown in Figure 3.5a to address the effect of the p-n heterojunction between NiO and SnO_2. The electrons will transfer from SnO_2 to NiO, while holes will transfer from NiO to SnO_2 to form a depleted layer at the interface of SnO_2 and NiO owing to the different work functions [11, 16].The width of the depletion layers (W_{SnO_2} and W_{NiO}) induced by the p-n heterojunction can be calculated using Eq (3-6) and Eq (3-7), respectively [11].

$$W_{SnO_2} = \left[\frac{2\varepsilon_{SnO_2}V_0}{q} \times \left\{\frac{N_{NiO}}{N_{SnO_2}\times(N_{SnO_2}+N_{NiO})}\right\}\right]^{1/2} \quad (3\text{-}6)$$

$$W_{NiO} = \left[\frac{2\varepsilon_{NiO}V_0}{q} \times \left\{\frac{N_{SnO_2}}{N_{NiO}\times(N_{SnO_2}+N_{NiO})}\right\}\right]^{1/2} \quad (3\text{-}7)$$

where ε_{SnO_2} (1.61×10^{-10} F·m^{-1}) and ε_{NiO} (1.04×10^{-10} F·m^{-1}) are the permittivity of SnO_2 and NiO, respectively [11, 50]; V_0 (0.4 eV) is the heterojunction potential barrier caused by the working function difference between SnO_2 and NiO; q is the charge of an electron (1.6×10^{-19} C) and N_{SnO_2} (3.6×10^{18} cm^{-3}) and N_{NiO} (1.3×10^{19} cm^{-3}) are the hole and electron concentrations, respectively [11, 51].

The calculated W_{SnO_2} and W_{NiO} values are ~ 13.1 nm and ~3 nm, respectively, based on Eq (3-6) and (3-7). According to the SEM images (Figure 3.3a, c), the thickness of the SnO_2 nanoneedles is less than 10 nm (less than 2 times the Debye length of SnO_2) [11, 52,53]. Therefore, the electrons of the SnO_2 nanoneedles are almost completely depleted in air due to the absorbed oxygen molecules. When an electron-donating gas (*e.g.*, H_2S) is supplied, the electrons captured by the absorbed oxygen ions are released, and N_{SnO_2} increases. Thus, the Fermi level (E_f) of SnO_2 shifts closer to the conduction band, and V_0 increases. As a result, W_{NiO} expands based on Eq (3-7), and the resistance of the sensor increases as the main conduction channel is the NiO nanowall in our case. In contrast, when an electron-withdrawing gas (*e.g.*, NO_2) is supplied, it extracts electrons from the SnO_2 nanoneedles and leads to a reduction in W_{NiO} and the resistance of the sensor. However, this decrease in W_{NiO} is marginal

because the electrons of the SnO_2 nanoneedles are almost completely depleted in the air, as mentioned above. This result indicates that the sensor based on NiO@SnO_2 HNSs (2 h) is more sensitive to H_2S than NO_2. The selectivity of the sensing mechanism toward H_2S among electron-donating gases (such as NH_3, C_7H_8, CHOH and H_2S) may be related to the bond dissociation energy of the gas molecules. Because the bond dissociation energy of H-S in H_2S is only 381 kJ/mol, which is smaller than that of N-H in NH_3, C-C, and C-H in VOCs, H-S can be easily broken to participate in the reaction with the adsorbed oxygen molecules. Thus, the sensor based on NiO@SnO_2 HNSs can selectively sense H_2S [54, 55]. In addition, the highest response NiO@SnO_2 HNS (2 h)-based sensor is greatly relating to the structure of sensing materials. Obviously, the size of the SnO_2 nanoneedles (2 h) is much smaller than that of the other SnO_2 nanosheets (4, 8, 12 h). For sensors based on the NiO@SnO_2 HNSs (4, 8, 12 h), the approach of H_2S to the interface of SnO_2 and NiO is hampered by the densely covered SnO_2 nanosheets. Thus, the reaction with H_2S is mainly confined to the surface of the SnO_2 nanosheets. As a result, the ability to tune the heterojunction potential barrier will become increasingly weak and lead to relatively low sensitivity. However, for the NiO@SnO_2 HNSs (2 h), the H_2S molecules can easily permeate and approach the interface of SnO_2 and NiO and efficiently tune the heterojunction potential barrier.

3.5. Conclusions

NiO@SnO_2 HNSs were uniformly and fully covered on ceramic microchips through a simple and cost-effective in situ growth method without a seed layer, additive salt, or surfactant. The morphologies and compositions of NiO@SnO_2 HNSs can be well tuned by varying the growth time. The NiO@SnO_2 HNS (2 h)-based gas microsensor showed a significant enhancement in response to H_2S compared with pure NiO nanowalls- and SnO_2 nanosheet-based sensors. This significant enhancement was due to the large surface area of the NiO@SnO_2 HNSs and the NiO@SnO_2 p-n heterojunction. This method provides a valuable approach for developing high-

performance gas microsensors with high uniformity. In addition, the performance reproducibility of sensors would be addressed if patterned sensing materials were obtained at the central part of sensor chips in the future. Because formation of patterned sensing materials can avoid contamination of electrode pads which can ensure the Ohm contact between the sensor and test system.

3.6. References

[1] M. Yang, X. Zhang, X. Cheng, Y. Xu, S. Gao, H. Zhao, L. Huo, Hierarchical NiO Cube/Nitrogen-Doped Reduced Graphene Oxide Composite with Enhanced H_2S Sensing Properties at Low Temperature, ACS Appl. Mater. Interfaces 76 (2017) 26293-26303.

[2] Z. Zhang, M. Xu, L. Liu, X. Ruan, J. Yan, W. Zhao, J. Yun, Y. Wang, S. Qin, T. Zhang, Novel SnO_2@ZnO hierarchical nanostructures for highly sensitive and selective NO_2 gas sensing, Sens. Actuators B Chem. 257 (2018) 714-727.

[3] S. Zhang, G. Sun, Y. Li, B. Zhang, L. Lin, Y. Wan, J. Cao, Z. Zhang, Continuously improved gas-sensing performance of SnO_2/Zn_2SnO_4 porous cubes by structure evolution and further NiO decoration, Sens. Actuators B Chem. 255 (2018) 2936-2943.

[4] J. Zhang, X. Liu, G. Neri, N. Pinna, Nanostructured Materials for Room-Temperature Gas Sensors, Adv. Mater. 28 (2016) 795-831.

[5] Y. Zhang, D. Li, L. Qin, P. Zhao, F. Liu, X. Chuai, P. Sun, X. Liang, Y. Gao, Y. Sun, G. Lu, Preparation and gas sensing properties of hierarchical leaf-like SnO_2 materials, Sens. Actuators B Chem. 255 (2018) 2944-2951.

[6] I. Cho, L. Kang, D. Yang, J. Yun, I. Park, Localized Liquid-Phase Synthesis of Porous SnO_2 Nanotubes on MEMS Platform for Low-Power, High Performance Gas Sensors. ACS Appl. Mater. Interfaces 9 (2017) 27111-27119.

[7] T. Yu, X. Zhang, Y. Xu, X. Cheng, S. Gao, H. Zhao, L. Huo, Enhanced H_2S sensing characteristics of CuO-NiO core-shell microspheres sensors, Sens. Actuators B Chem. 230 (2016) 706-713.

[8] Y. Wang, F. Qu, J. Liu, Y. Wang, J. Zhou, S. Ruan, Enhanced H_2S sensing characteristics of CuO-NiO core-shell microspheres sensors, Sens. Actuators B Chem. 209 (2015) 515-523.

[9] C. Wang, X. Cheng, X. Zhou, P. Sun, X. Hu, K. G. Shimanoe, G. Lu, N. Yamazoe, Hierarchical alpha-Fe_2O_3/NiO composites with a hollow structure for a gas sensor, ACS Appl.

Mater. Interfaces 6 (2014) 12031-12037.

[10] T.V. Dang, N.D. Hoa, N.V. Duy, N.V. Hieu, Chlorine Gas Sensing Performance of On-Chip Grown ZnO, WO_3, and SnO_2 Nanowire Sensors, ACS Appl. Mater. Interfaces 8 (2016) 4828-4837.

[11] S.W. Choi, A. Katoch, J.H. Kim, S.S. Kim, Prominent reducing gas-sensing performances of n-SnO_2 nanowires by local creation of p-n heterojunctions by functionalization with p-Cr_2O_3 nanoparticles, ACS Appl. Mater. Interfaces 6 (2014) 17723.

[12] J. Wang, P. Yang, X. Wei, High-performance, room-temperature, and no-humidity-impact ammonia sensor based on heterogeneous nickel oxide and zinc oxide nanocrystals, ACS Appl. Mater. Interfaces 7 (2015) 3816-3824.

[13] L. Xu, R. Zheng, S. Liu, J. Song, J. Chen, B. Dong, H. Song, NiO@ZnO heterostructural nanotubes: coelectrospinning fabrication, characterization, and highly enhanced gas sensing properties, Inorg. Chem. 51 (2012) 7733-7740.

[14] J. Zhang, D. Zeng, Q. Zhu, J. Wu, Q. Huang, W. Zhang, C. Xie, Enhanced room temperature NO_2 response of NiO-SnO_2 nanocomposites induced by interface bonds at the p-n heterojunction, Phys.Chem.Chem.Phys. 18 (2016) 5386-5896.

[15] S. Ji, H. Wang, T.Wang, D. Yan, A high-performance room-temperature NO_2 sensor based on an ultrathin heterojunction film, Adv. Mater. 5 (2013) 1755-1760.

[16] Y. Wang, C. Liu, Z. Wang, Z. Song, X. Zhou, N. Han, Y. Chen, Sputtered SnO_2:NiO thin films on self-assembled Au nanoparticle arrays for MEMS compatible NO_2 gas sensors, Sens. Actuators B 278 (2019) 28-38.

[17] D. Meng, D. Liu, G. Wang, Y. Shen, X. San, M. Li, F. Meng, Low-temperature formaldehyde gas sensors based on NiO-SnO_2 heterojunction microflowers assembled by thin porous nanosheets, Sens. Actuators B Chem. 273 (2018) 418-428.

[18] H. Liu, W. Zhang, H. Yu, L. Gao, Z. Song, S. Xu, M. Li, Y. Wang, H. Song, J. Tang,

Solution-Processed Gas Sensors Employing SnO_2 Quantum Dot/MWCNT Nanocomposites, ACS Appl. Mater. Interfaces 8 (2016) 840-846.

[19] Z. Wang, Z. Li, T. Jiang, X. Xu, C. Wang, Ultrasensitive hydrogen sensor based on Pd(0)-loaded SnO_2 electrospun nanofibers at room temperature, ACS Appl. Mater. Interfaces 5 (2013) 2013-2021.

[20] M. Yuasa, T. Kida, K. Shimanoe, Preparation of a stable sol suspension of Pd-loaded SnO(2) nanocrystals by a photochemical deposition method for highly sensitive semiconductor gas sensors, ACS Appl. Mater. Interfaces 4 (2012) 4231-4236.

[21] S. Bai, J. Liu, J. Guo, R. Luo, D. Lia, Y. Song, C. Liu, A. Chen, Facile preparation of SnO_2/NiO composites and enhancement of sensing performance to NO_2, Sens. Actuators B Chem. 249 (2017) 22-29.

[22] P.M. Bulemo, H.J. Cho, D.H. Kim, I.D. Kim, Facile Synthesis of Pt-Functionalized Meso/Macroporous SnO_2 Hollow Spheres through in Situ Templating with SiO_2 for H_2S Sensors, ACS Appl. Mater. Interfaces 10 (2018) 18183-18191.

[23] T. Kida, S. Fujiyama, K. Suematsu, M. Yuasa, K. Shimanoe, Pore and Particle Size Control of Gas Sensing Films Using SnO_2 Nanoparticles Synthesized by Seed-Mediated Growth: Design of Highly Sensitive Gas Sensors, J. Phys. Chem. C. 117 (2013) 17574-17582.

[24] H. Kwon, J. S. Yoon, Y. Lee, D. Y. Kim, C. K. Baek, J. K. Kim, An array of metal oxides nanoscale hetero p-n junctions toward designable and highly-selective gas sensors, Sens. Actuators B Chem. 255 (2018) 1663-1670.

[25] P. Tyagi, A. Sharma, M. Tomar, V. Gupta, SnO2 thin film sensor having NiO catalyst for detection of SO_2 gas with improved response characteristics, Sens. Actuators B Chem. 248 (2017) 998-1005.

[26] H. Xu, J. Ju, W. Li, J. Zhang, J. Wang, B. Cao, Superior triethylamine-sensing properties based on TiO_2/SnO_2 n–n heterojunction nanosheets directly grown on ceramic tubes, Sens.

Actuators B Chem. 228 (2016) 634-642.

[27] J. Fang, Y. Zhu, D. Wu, C. Zhang, S. Xu, D. Xiong, P. Yang, L. Wang, P. Chu, Gas sensing properties of NiO/SnO_2 heterojunction thin film, Sens. Actuators B Chem. 252 (2017) 1163-1168.

[28] G. Li, X. Wang, L. Liu, F. Shen, Z. Cui, W. Chen, T. Zhang, Controllable Synthesis of 3D $Ni(OH)_2$ and NiO Nanowalls on Various Substrates for High-Performance Nanosensors, Small, 11 (2015) 731.

Y. Cheng, Y. Wang, Y. Zheng, Y. Qin, Two-Step Self-Assembly of Nanodisks into Plate-Built Cylinders through Oriented Aggregation, J. Phys. Chem. B. 109 (2005) 11548-11551.

[29] Y. Masuda, T. Ohji, Ka. Kato, Site-Selective Chemical Reaction on Flexible Polymer Films for Tin Oxide Nanosheet Patterning, Eur. J. Inorg. Chem. 18 (2011) 2819-2825.

[30] H. Wang, S. Kalytchuk, H. Yang, L. He, C.Y. Hu, W.Y. Teoh, A.L. Rogach, Hierarchical growth of SnO_2 nanostructured films on FTO substrates: structural defects induced by Sn(II) self-doping and their effects on optical and photoelectrochemical properties, Nanoscale 6 (2014) 6084-6891.

[31] S. Sarkar, M. Pradhan, A.K. Sinha, M. Basu, Y. Negishi, T. Pal, An Aminolytic Approach toward Hierarchical β-$Ni(OH)_2$ Nanoporous Architectures: A Bimodal Forum for Photocatalytic and Surface-Enhanced Raman Scattering Activity, Inorg. Chem. 49 (2010) 8813-8827.

[32] Y. Wang, G. Cheng, Y. Zhang, H. Ke, C. Zhu, Synthesis of fluorinated SnO_2 3D hierarchical structures assembled from nanosheets and their enhanced photocatalytic activity, RSC. Adv. 5 (2015) 88079-88086.

[33] Y. Hong, J.W. Yoon, J.H. Lee, Y. Kang, One-pot synthesis of Pd-loaded SnO(2) yolk-shell nanostructures for ultraselective methyl benzene sensors, Chem. Eur. J. 20 (2014) 2737-2341.

[34] G. Li, X. Wang, H. Ding, T. Zhang, A facile synthesis method for $Ni(OH)_2$ ultrathin

nanosheets and their conversion to porous NiO nanosheets used for formaldehyde sensing, RSC Adv. 2 (2012) 13018.

[35] Y. Liu, Y. Jiao, Z. Zhang, F. Qu, A. Umar, X. Wu, Hierarchical SnO(2) nanostructures made of intermingled ultrathin nanosheets for environmental remediation, smart gas sensor, and supercapacitor applications, ACS Appl. Mater. Interfaces 6 (2014) 2174-2184.

[36] D. Li, M.H. Nielsen, J.R.I. Lee, C. Frandsen, J.F. Banfield, J.J. De Yoreo, Direction-Specific Interactions Control Crystal Growth by Oriented Attachment, Science 336 (2012) 1014-1018.

[37] Y. Masuda, T.I Ohji, K. Kato, Tin oxide nanosheet assembly for hydrophobic/hydrophilic coating and cancer sensing, ACS Appl. Mater. Interfaces 4 (2012) 1666-1674.

[38] G. Denes, G. Lazanas, Oxidation of SnF_2 stannous fluoride in aqueous solutions, Hyperfine Interact. 90 (1994) 435-439.

[39] X. Zhao, B. Liu, C. Hu, M. Cao, In situ growth of hierarchical SnO(2) nanosheet arrays on 3D macroporous substrates as high-performance electrodes, Chem. Eur. J. 20 (2014) 467.

[40] H. Wang, A. Rogach, Hierarchical SnO_2 Nanostructures: Recent Advances in Design, Synthesis, and Applications, Chem. Mater. 26 (2014) 123-133.

[41] G. J. Sun, H. Kheel, J. K. Lee, S. Choi, S. Lee, C. Lee, H2S gas sensing properties of Fe_2O_3 nanoparticle-decorated NiO nanoplate sensors, Surf. Coat. Technol. 307 (2016) 1088-1095.

[42] T. Yu, X. Cheng, X. Zhang, L. Sui, Y. Xu, S. Gao, H. Zhao, L. Huo, Highly sensitive H_2S detection sensors at low temperature based on hierarchically structured NiO porous nanowall arrays, J. Mater. Chem. A. 3 (2015) 11991-11999.

[43] M. Li, D. Zhou, J. Zhao, Z. Zheng, J. He, L. Hu, Z. Xia, J. Tang, H. Liu, Resistive gas sensors based on colloidal quantum dot (CQD) solids for hydrogen sulfide detection, Sens. Actuators B Chem. 217 (2015) 198-201.

[44] Z. Song, Z. Wei, B. Wang, Z. Luo, S. Xu, W. Zhang, H. Yu, M. Li, Z. Huang, J. Zang, F. Yi, H. Liu, Sensitive Room-Temperature H_2S Gas Sensors Employing SnO_2 Quantum Wire/Reduced Graphene Oxide Nanocomposites, Chem. Mater. 28 (2016) 1205-1212.

[45] A. Shanmugasundaram, N.D. Chinh, Y.J. Jeong, T.F. Hou, D.S. Kim, D. Kim, Y. Kim, D. Lee, Hierarchical nanohybrids of B- and N-codoped graphene/mesoporous NiO nanodisks: an exciting new material for selective sensing of H_2S at near ambient temperature, J. Mater. Chem. A 7 (2019) 9263-9278.

[46] J. Kim, K. Yong, Mechanism Study of ZnO Nanorod-Bundle Sensors for H_2S Gas Sensing, J. Phys. Chem. C. 115 (2011) 7218-7224.

[47] P. Su, Y. Peng, Fabrication of a room-temperature H_2S gas sensor based on PPy/WO_3 nanocomposite films by in-situ photopolymerization, Sens. Actuators B 193 (2014) 637-643.

[48] Z. Hua, Y. Li, Y. Zeng, Y. Wu, A theoretical investigation of the power-law response of metal oxide semiconductor gas sensors I: Schottky barrier control, Sens. Actuators B 225 (2018) 1911-1919.

[49] D.R. Miller, S.A. Akbar, P.A. Morris, Nanoscale metal oxide-based heterojunctions for gas sensing: A review, Sens. Actuators B 204 (2014) 250-272.

[50] P. Zhao, Z. Liu, Z. Lin, D. Chen, J. Su, C. Zhang, J. Zhang, J. Chang, Y. Hao, Device simulation of inverted $CH_3NH_3PbI_{3-x}Cl_x$ perovskite solar cells based on PCBM electron transport layer and NiO hole transport layer, Sol. Energy 169 (2018), 11.

[51] H. Sato, T. Minami, S. Takata, T. Yamada, Transparent conducting p-type NiO thin films prepared by magnetron sputtering, Thin Solid Films 236 (1993) 27.

[52] S.H. Lee, V. Galstyan, A. Ponzoni, I. G. Juan, R. Riedel, M.A. Dourges, Y. Nicolas, T. Toupance, Finely Tuned SnO_2 Nanoparticles for Efficient Detection of Reducing and Oxidizing Gases: The Influence of Alkali Metal Cation on Gas-Sensing Properties. ACS Appl. Mater. Interfaces 10 (2018) 10173-10184.

[53] Zhu, L.; Yuan, K.; Yang, J.; Ma, H.; Wang, T.; Ji, X.; Feng, J.; Devi, A.; Lu, H., Fabrication of heterostructural p-CuO/n-SnO_2 core-shell nanowires for enhanced sensitive and selective formaldehyde detection, Sens. Actuators B 290 (2019) 233-241.

[54] D.W. Breck, Zeolite Molecular Sieves: Structure, Chemistry, and Use, John Wiley and Sons, New York, 1974, Ch. 8.

[55] J.A. Dean, Lange's Handbook of Chemistry, McGraw-Hill Professional, 2004, Ch. 4.

3.7. Supplementary Data

In situ Growth of NiO@SnO_2 p-n Heterostructures for High Performance H_2S Sensing

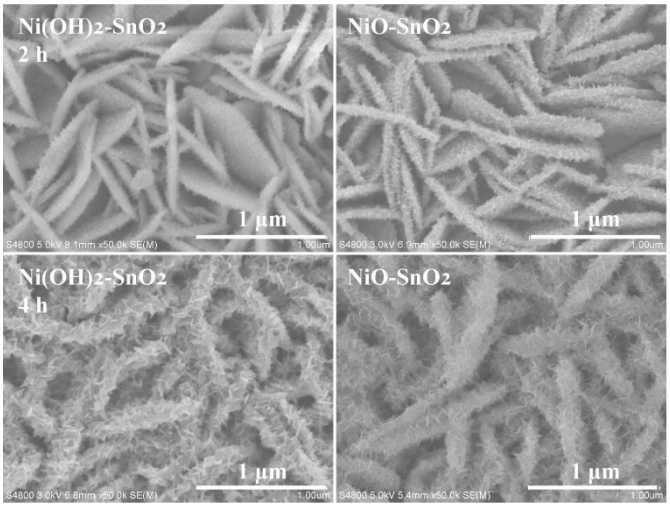

Figure S 3.1 SEM images (Scale bar: 1 μm) of prepared $Ni(OH)_2$@SnO_2 hierarchical nanostructures (HNSs) before and after annealing treatment.

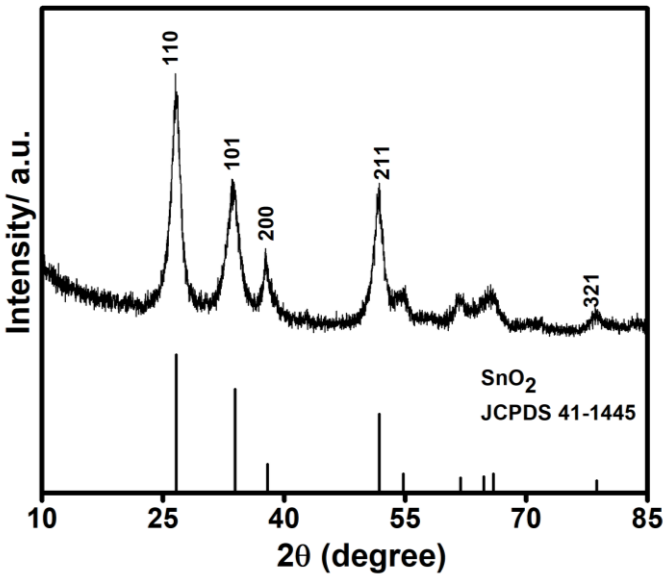

Figure S 3.2 XRD pattern of pure SnO_2.

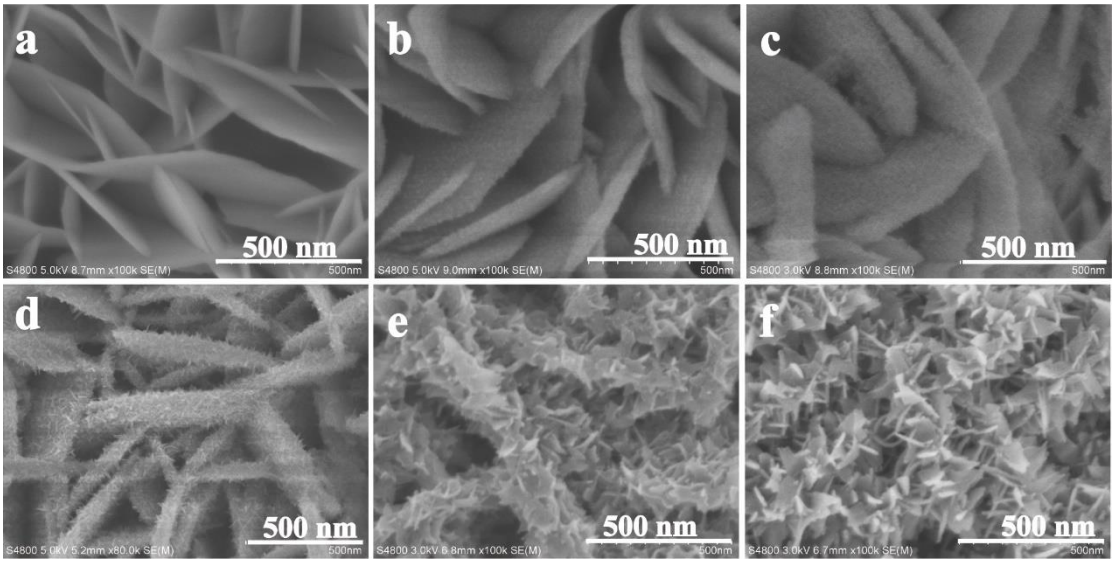

Figure S 3.3 The SEM images (Scale bars, 500 nm) of (a) pure $Ni(OH)_2$ nanowalls and $Ni(OH)_2@SnO_2$ HNSs under different reaction times: (b) 0.5 h, (c) 1 h, (d) 2 h, (e) 4 h, and (f) 8 h.

Table S 3.1 EDXS results of $Ni(OH)_2@SnO_2$ HNSs

	O (At%)	Ni (At%)	Sn (At%)
2 h	22.60	47.13	30.26
4 h	18.23	28.14	53.63
8 h	21.94	15.24	62.81
12h	16.72	1.4	81.88

Table S 3.2 Comparison results of H_2S sensors based on NiO-SnO_2 system and NiO-based and SnO_2-based nanomaterials in recent few years.

Material	Synthesis method	T (°C)	C(ppm)/S	τ_{resp}/τ_{recov} (s)	Year	Ref
SnO_2-NiO	Physically mixing	350	1 ppm/0.8[a]	NG/>1000	2013	[1]
SnO_2@Cu	supttering	180	100 ppm/24.3[b]	~10.1/~42.4	2014	[2]
NiO@Fe_2O_3	hydrothermal	200	10 ppm/6.5[b]	NG/~25	2014	[3]
CuO@NiO	hydrothermal	260	100 ppm/43.5[b]	~18/~28	2015	[4]
NiO@CdO	hydrothermal	92	50 ppm/47.8[b]	NG/~82	2016	[5]
rGO@SnO_2	hydrothermal	RT	50 ppm/33[b]	2/292	2016	[6]
SnO_2@NiO	RF sputter	RT	10 ppm/440[b]	NG/>5000	2017	[7]
SnO_2@NiO	sputter	250	100 ppm/8[b]	15/100	2017	[8]
N-rGO@NiO	hydrothermal	92	50 ppm/31[b]	NG/~12	2017	[9]
NiO@PdO	metal-citrate complex method	60	100 ppm/0.95[a]	~6/~10	2017	[10]
WO_3@NiO	Aerosol assisted chemical vapor deposition	250	50 ppm/13[b]	88/NG	2018	[11]

B-rGO@NiO	hydrothermal	150	10 ppm/5.57[b]	38/44	2019	[12]
NiO@SnO_2 HNSs	chemical deposition	240	50 ppm/183.5[a] 10 ppm/25.4[a]	~45/~60 ~35/~42		This work

Note: [a]S = ΔR/Rg or S = ΔR/Ra; [b]S = Ra/Rg or S = Rg/Ra; NG: not giving

References

[1] S.C. Lee, S. Y. Kim, B.W. Hwang, S.Y. Jung, D. Ragupathy, I.S. Son, D.D. Lee, J.C. Kim, Improvement of H_2S sensing properties of SnO_2-based thick film gas sensors promoted with MoO_3 and NiO, Sensors 13 (2013) 3889-3901.

[2] S. Zhang, P. Zhang, Y. Wang, Y. Ma, J. Zhong, X. Sun, Facile fabrication of a well-ordered porous Cu-doped SnO_2 thin film for H_2S sensing, ACS Appl. Mater. Interfaces 6 (2014) 14975-14980.

[3] F. Li, Y. Chen, J. Ma, Fe^{3+} facilitating the response of NiO towards H_2S, RSC Adv. 4 (2014) 14201-14205.

[4] Y. Wang, F. Qu, J. Liu, Y. Wang, J. Zhou, S. Ruan, Enhanced H_2S sensing characteristics of CuO-NiO core-shell microspheres sensors, Sens. Actuators B 209 (20150 515-523.

[5] T. Yu, X. Zhang, Y. Xu, X. Cheng, S. Gao, H. Zhao, L. Huo, Low concentration H_2S detection of CdO-decorated hierarchically mesoporous NiO nanofilm with wrinkle structure, Sens. Actuators B 230 (2016) 706-713.

[6] Z. Song, Z. Wei, B. Wang, Z. Luo, S. Xu, W. Zhang, H. Yu, M. Li, Z. Huang, J. Zang, F. Yi, H. Liu, Sensitive Room-Temperature H_2S Gas Sensors Employing SnO_2 Quantum Wire/Reduced Graphene Oxide Nanocomposites, Chem. Mater. 28 (2016) 1205-1212.

[7] M. Kaur, B.K. Dadhich, R. Singh, K. Ganapathi, T. Bagwaiya, S. Bhattacharya, A.K. Debnath, K.P. Muthe, S.C. Gadkari, RF sputtered SnO_2: NiO thin films as sub-ppm H_2S sensor operable at room temperature, Sens. Actuators B 242 (2017) 389-403.

[8] J. Fang, Y. Zhu, D. Wu, C. Zhang, S. Xu, D. Xiong, P.Yang, L. Wang, P.K. Chu, Gas sensing properties of NiO/SnO_2 heterojunction thin film, Sens. Actuators B 252 (2017) 1163-1168.

[9] M. Yang, X. Zhang, X. Cheng, Y. Xu, S. Gao, H. Zhao, L. Huo, Hierarchical NiO Cube/Nitrogen-Doped Reduced Graphene Oxide Composite with Enhanced H2S Sensing Properties at Low Temperature, ACS Appl. Mater. Interfaces 9 (2017) 26293-26303.

[10] C. Balamurugan, Y.J. Jeong, D.W. Lee, Enhanced H_2S Sensing Performance of a p -type Semiconducting PdO-NiO Nanoscale Heteromixture, Appl. Surf. Sci. 420 (2017) 638-650.

[11] E. Navarrete, C. Bittencourt, P. Umek, E. Llobet, AACVD and gas sensing properties of nickel oxide nanoparticle decorated tungsten oxide nanowires, J. Mater. Chem. C 6 (2018) 5181-5192.

[12] A. Shanmugasundaram, N.D. Chinh, Y.J. Jeong, T.F. Hou, D.S. Kim, D. Kim, Y.B. Kim, D.W. Lee, Hierarchical nanohybrids of B- and N-codoped graphene/mesoporous NiO nanodisks: an exciting new material for selective sensing of H_2S at near ambient temperature, J. Mater. Chem. C 7 (2019) 9263-9278.

Chapter 4: In situ Growth of Patterned NiO Nanowalls for Wafer-scaled Miniaturized Gas Sensors Design and Fabrication

4.1. Abstract

The reproducibility and uniformity of the sensors in wafer-scale fabrication are still a challenge as mentioned in Chapter 3. In this work, a “top-down” and “bottom-up” combined strategy was proposed to manufacture wafer-scaled miniaturized gas sensors with high-throughput by growth in situ of $Ni(OH)_2$ nanowalls at specific locations. First, the micro-hotplates were fabricated on a two-inch (2”) silicon wafer by micro electro mechanical system (MEMS) fabrication techniques (“top-down” strategy). Then a template-guided controllable de-wetting method was used to assemble a thermoplastic elastomer (TPE) thin film with uniform micro-sized holes (relative standard deviation (RSD) of the size of micro-hole < 3.5 %, n >300), which serves as the patterned mask for in situ growing $Ni(OH)_2$ nanowalls at the micro-hole areas (“bottom up” strategy). Owing to this unique fabrication stategy, it can avoid contamination of electrode pads and form Ohm contact between sensors and test system. The obtained gas microsensors based on this strategy showed great reproducibility of electric properties (RSD < 0.8%, n=8) and sensing response toward real-time H_2S detection (RSD <3.5%, n=8).

Author contributions: Lin Liu has got the permission from other co-authors for this paper to her thesis. All the paper work and data analysis are finished by Lin Liu and most of the data including SEM, FTIR, pictures, sensing performance are also collected by Lin Liu.

4.2. Introduction

High-throughput and low-cost wafer-scale fabrication of metal oxides based gas sensors with good reproducibility and uniformity are urgent demand for widely applications in environmental monitoring [1, 2]. Two main technological hurdles need to be overcomed for low-cost wafer-scale fabrication, namely, how to efficiently form microscale-patterned sensing nanomaterials at specific locations on micro-elelctrode chips and how to rationally integrate patterning methods with the micro electro mechanical system (MEMS) technique ("top-down" microfabrication technique). During past few decades, many advanced instruments and techniques have been utilized to obtain high-resolution material patterns on substrates including printing [3, 4], precisely manipulated coating [5-7], soft-photolithography-guided method [8-10], controllable de-wetting [11-13], and combined strategies of two or three techniques [14-16]. However, compared with in situ growing method ('bottom-up' strategy), the interconnection of sensing materials and substrate is relatively weak and the obtained sensing material patterns are tend to be inhomogeneity, which can greatly influence the stability, uniformity and reproducibility of sensors [17, 18].

A few studies have shown the feasibility to directly obtain patterned metal oxides on the micro-electrode chips such as laser-assisted method and sputtering which are compatible with MEMS fabrication techniques [19-22]. However, for the laser-assisted method, the continuous laser irradiation and complicated set-ups are required resulted in increased cost. The sputtering method also has high and always leads to low sensitivity compared with solotion-based synthesized methods [22-24]. Notably, template-guided controllable de-wetting method with the capability to precisely control of the shape, size and location of liquid droplets shows the feasibility to assemble uniform porous film due to the immiscibility of two different solutions [25]. Therefore, it is a potential solution to integrate "bottom-up"and "top-down"strategies for

wafer-scale fabrication of miniaturized gas sensors by utilizing the uniform porous film as a mask for growth in situ of metal oxides. An ideal mask material requires good thermal stability and durability to acid and alkali solutions, and also must be easily removed. Although photoresists are common mask materials in the field of the MEMS, their thermal and chemical stabilities are not good enough to serve as masks in reaction solutions (acid or alkali condition) during growth in situ of metal oxides at elevated temperatures (50 to 90 ℃) for a long time (> 15 h). According to our previous work, thermoplastic elastomer (TPE) is an ideal cost-effective mask due to its good chemical and thermal stability and can be easily peeled-off from the Si substrate [26, 27]. In this work, we combined "bottom-up"and "top-down"strategies for wafer-scale fabrication of miniaturized gas sensors with excellent reproducibility and high-throughput. Firstly, a "top-down" strategy was employed to fabricate the micro-hotplate wafer, which was followed by photolithography to form a dry film photoresist (DFP) dot array. The DPF dots serve as templates to assemble the porous TPE film with uniform micro-sized holes. In order to strengthen the interconnection between Si substrate and sensing materials, a "bottom-up" strategy was utilized to form patterned NiO nanowalls at specific locations on the micro-hotplate wafer. The obtained miniaturized gas sensors showed excellent reproducibility of electrical properties (RSD < 0.8%, n=8) and sensing response toward H_2S (RSD <3.5%, n=8).

4.3. Experimental Section

4.3.1. Chemicals

All reagents are analytical grade and were used without further purification. *n*-Hexane, sodium carbonate (Na_2CO_3), ethanol, $Ni(OH)_2$, NaOH and NH_4Cl were from Sinopharm Chemical Reagent Co., Ltd. and 25% tetramethylammonium hydroxide (TMAH) was purchased from Jianghua Microelectronics Materials Co., Ltd.. TPE (C6612T-A78) was from GainShine Co., Ltd. and DFP (SAF2100) was a negative-type DFP from Dupont Co., Ltd.. De-

ionized (DI) water used to prepare reagents was obtained from a Millipore system (resistivity 18.2 MΩ.cm). TPE elastomer was dissolved in *n*-hexane through magnetic stirring and ready for using. The 2-inch silicon wafers (300 um, double sides polished, Tianjing Yunjing Technologh Co., Ltd.). Micro-hotplate wafers were fabricated by Leanstar-Tech Co., Ltd., which contain more than 1000 micro-hotplates in each 2-inch wafer.

4.3.2. Preparing Porous TPE Film

The DFP film was cut to fit the size of silicon wafer and then laminated on the prepared micro-hotplate wafer at a specific temperature (90 ºC) and baked at 60 ºC for 15 min. Standard UV exposure (10 s) was performed at 365 nm to obtain patterned DFP dots via photolithography. After treatment in the developing solution (2% Na_2CO_3) for 10 min at room temperature, the unexposed area of DFP film was thoroughly removed. Then, spin-coating water (500 rpm, 9 s) on the micro-hotplate wafer and waiting for the template-guided controllable de-wetting process to form uniform water droplets. Subsequently, 18% TPE solution was spin-coated (500 rpm, 9 s) on the wafer and this was followed by spin-coating with ethanol after the evaporation of *n*-hexane (~5 s). 5% TMAH solution was applied to strip off DFP dots and then the wafer was rinsed with water and ethanol for few times. Finally, the micro-hotplate wafer covered with porous TPE film was obtained and ready for growth in situ of $Ni(OH)_2$ nanowalls.

4.3.3. Characterization

XRD (Bruker AXS, D8 Advance) and SEM (Hitachi-s4800) were used to analyse the chemical composition and morphology of synthesized materials. I-V curves were measures with Agilent B1500A. Functional groups of DFP was tested by Fourier transform infrared spectroscopy (FTIR) (Nicolet iN10). The water contact angle (WCA) measurements were conducted on an OCA20 machine (Data-Physics, Germany) at ambient temperature. Optical

images and videos were captured by using a Canon Camera (Nikon, Japan) and microscope (Motic SMZ-168) which is connected with CCD camera.

4.3.4. Measurement of Gas Sensing Performance

After growing the $Ni(OH)_2$ nanowalls, the porous TPE film was peeled off from the micro-hotplate wafer. Then, the wafer was placed in the fixture (Figure S4.1b) by exposing the back of micro-hotplate and then immersed in 25% TMAH at 90 ºC in an oil bath to further remove the silicon below the sensing area (the centre of micro-hotplate). After annealing treatment (Ar, 400 ℃, 2 h), the micro-hotplates with sensing materials (NiO nanowalls) were bonded to the test substrate. The performance of the sensors was measured simultaneously in a WS-30A static analysis system (Hanwei Electronics Co. Ltd., Henan Province, China) with the constant loop voltage of 5 V. Typically, the sensors were placed in a gas chamber (18 L) in air. The different concentrations of target gas (C_2H_5OH and HCHO) were obtained by injecting a certain amount target solution into the chamber. The precise concentration was calculated according to following formula [28]:

$$C = \frac{22.4 \times \varphi \times \rho \times V1}{M \times V2} \quad (4\text{-}1)$$

where C (ppm) is concentration of target gas, φ is volume fraction of target gas, ρ (g/mL), V1 (μL) and M(g/mol) are density, injected volume and molecular weight of target solution, respectively and V2 (L) is volume of chamber. For the target gases such as NH_3, C_7H_8, NO_2 and H_2S, the different concentrations were implemented by simply diluting the high concentration of gas sources. The sensing response of sensor is defined as ΔV/Vg, where ΔV is the absolute differential of voltage on sensor in air and target gas, Vg is the voltage on sensor in target gas. All the sensing measurements were performed under laboratory conditions (RH: 50–60%; temperature: 20–25 °C).

4.4 Results and Discussion

4.4.1. Schematic of Fabrication of Wafer-scaled Gas Sensors

The schematic structure of the micro-hotplate is shown in Figure 4.1a, from bottom to top are silicon covered with a thin layer of silicon nitride (Si_3N_4) on both side of silicon, heating electrode (Pt, ~200 nm), Si_3N_4 (insulator layer, ~280 nm), and the working electrode (Pt, ~ 200 nm), respectively. After constructing all of the structures on the front side, reactive ion etching (RIE) and silicon deep etching were employed to etch the back side of the silicon (etching area 720 μm * 720 μm; etching depth 250 μm). Wet etching was used to further etch the silicon on the back side in 25% TMAH solution at 90 °C with a specially designed fixture (Figure S4.1b) to protect the front side. The size of each micro-hotplate was 1.2 mm *1.2 mm. As the micro-hotplate becomes very fragile after the wet-etching process, wet-etching was not carried out until the growth in situ of the $Ni(OH)_2$ nanowalls. A controllable template-guided de-wetting method was utilized to implement growth in situ of patterned $Ni(OH)_2$ nanowalls for wafer-scale fabrication (Figure 4.1a). The details of assembling porous TPE films are demonstrated in Figure 4.1b. Firstly, the DFP dots were formed on the two-inch (2”) micro-hotplate wafer via photolithography (Figure 4.1b (1)). Then, water was spin-coated onto the micro-hotplate wafer covered with DFP dots and water droplets were pinned by the DFP dots during the template-guided controllable de-wetting process (Figure 4.1b (2)). Subsequently, TPE solution (18 wt%, in *n*-hexane) was spin-coated and waited for the evaporation of hexane (Figure 4.1b (3)). After that, in order to obtain a uniform porous TPE film as displayed in Figure 4.1b (4), ethanol was spin-coated twice to release the water, as it can partially dissolve the ultrathin TPE film which is covered on the surface of water droplets. In the optical picture result of step ‘b (4)’, an obvious gap between the DFP dots and porous TPF film was formed. Because the water droplet is immiscible with hexane and the density of water is greater than hexane so the TPE solution can be effectively isolated from the DFP dots. Since the DFP dots

will absorb water and swell once immersed in a 5% TMAH solution, the formed gap can facilitate striping off the DFP dots by offering enough swelling space (Figure 4.1b (5)). Without the gap, the swelled DFP dots would tightly contact with the TPE film and the TPE film would peel off from the substrate with the DFP dots together during the striping off process. After assembly of the porous TPE film, the micro-hotplate wafer covered with the porous TPE film was immersed in the mixed solution of 37.5 mM $NiCl_2$, 200 mM NH_4Cl, and 68.75 mM NaOH to grow in situ the $Ni(OH)_2$ nanowalls at the micro-hole areas (Figure 4.1b (6)). The micro-hotplates covered with the porous TPE film after growth of the $Ni(OH)_2$ nanowalls at centre of each micro-hotplate are displayed in the photograph of step 'b (6)'. The porous TPE film was peeled off effortlessly and thoroughly with the assistance of ethanol without contaminating $Ni(OH)_2$ nanowalls (Figure 4.1b (7)). The optical photograph of the step 'b (7)' shows the micro-hotplates covered with NiO nanowalls after removing the porous TPE film and annealing at 400 °C for 2 h under an argon atmosphere.

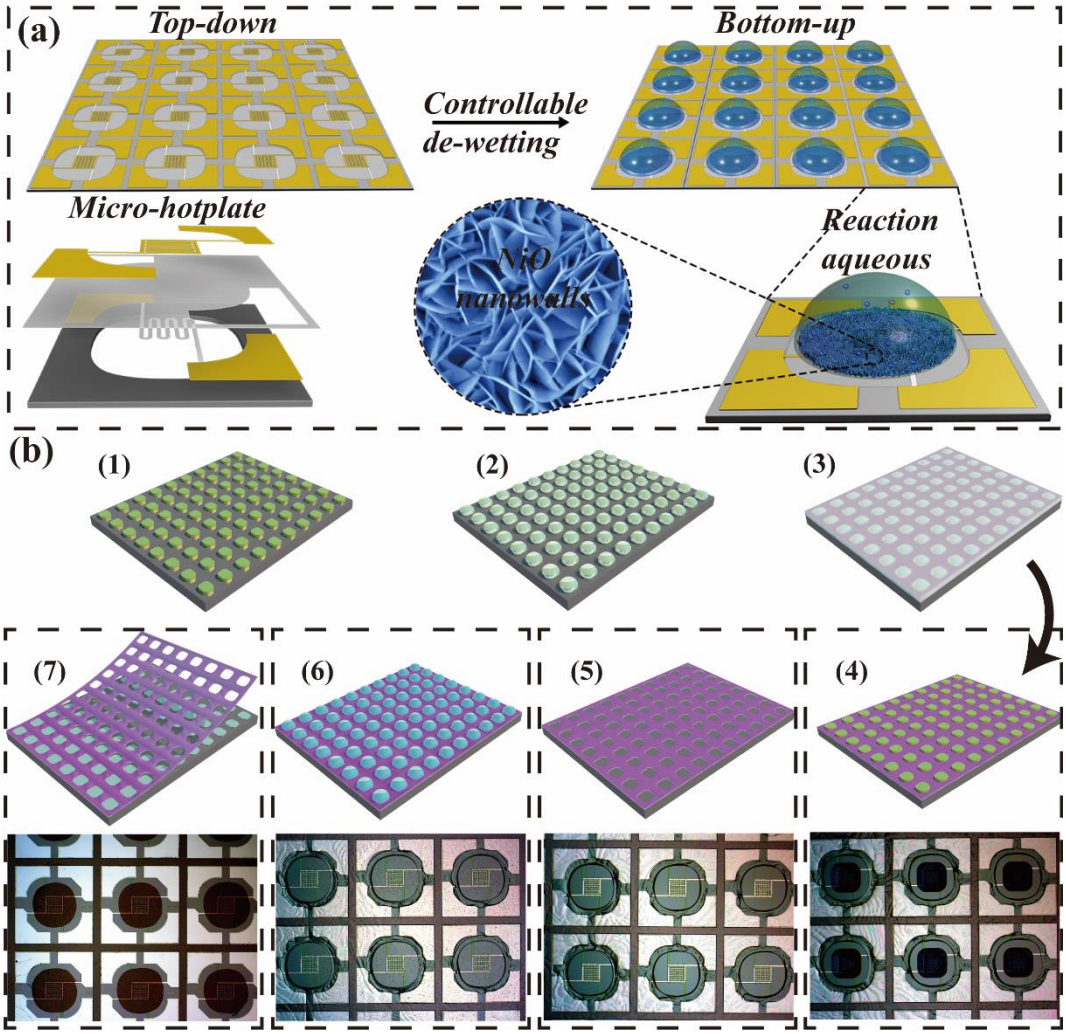

Figure 4.1 (a) schematic of a top-down and bottom-up combined strategy for fabricating wafer-scale miniaturized gas sensors; (b) schematic of template-guided controllable de-wetting and in situ growth steps during wafer-scale fabrication process and relevant photograph results of some steps: (1) patterned dry film photoresist (DFP) dots were formed on the two-inch (2”) micro-hotplate wafer via photolithography; (2) the formed of water droplet array on the surface of DFP dots; (3) spin-coating of 18% TPE solution and waiting for evaporation of n-hexane; (4) the formed uniform porous TPE film with a gap to the DFP dots; (5) strip off of the DFP dots; (6) in situ growth of $Ni(OH)_2$ nanowalls; (7) peel off of the porous TPE film.

4.4.2. Effect of DFP Dots’ Size to Assemble Porous TPE Film

The reproducibility of sensors is significantly dependent on the size uniformity of micro-holes of the porous TPE film. The size of micro-holes is defined by measuring the distance

from centre point of each edge to the centre point of opposite edge and calculating the average value. Porous TPE films with different size of micro-holes were obtained by varying the size of DFP dots (from 500 μm to 300 μm; Figure 4.2). Obviously, the size of micro-holes decreased along with decrease of the size of DFP dots. From the histogram graph of size distribution of micro-holes, it can be seen the size of micro-holes decreases from ~763.69 ± 22.32 μm to ~500.87 ± 47.97 μm. The dispersion of the obtained size of micro-holes based on different size of DFP dots is shown in Table 4.1. According to the Table 1, the relative standard deviation (RSD) values (n > 300) of the size of micro-holes based on 500 μm, 400 μm and 300 μm DFP dots are 3.31%, 2.94%, and 9.58%, respectively. For the DFP dots larger than 300 μm, the size distribution of micro-holes is significantly narrowed and the RSD values are less than 3.5% indicating that the obtained micro-holes of the porous TPE films have an excellent uniformity which is a precondition to ensure the reproducibility of gas sensors.

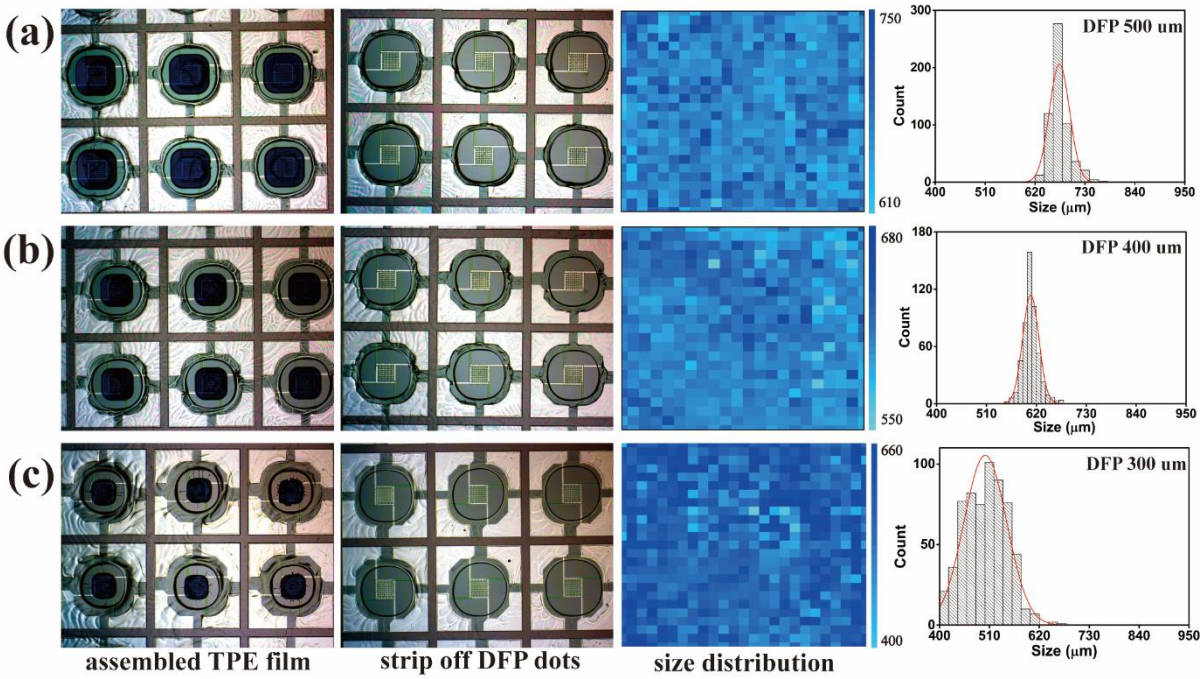

Figure 4.2 (a-c) the photographs of porous TPE films and the size distribution of micro-holes based on different sizes of DFP dots. From left to right of each row are the picture of assembled TPE film on the micro-hotplates surrounding the DFP dots, the picture of porous TPE film after

stripping off the DFP dots, the size distribution mapping and histogram graphs of size of the micro-holes, respectively.

Table 4.1 The size dispersion of micro-holes based on different size of DFP dots.

DFP Size （μm）	N	SD （μm）	Mean （μm）	RSD (%)
500	576	22.32	673.69	3.31
400	510	17.85	607.49	2.94
300	575	47.97	500.87	9.58

Working temperature distribution is another important parameter which can influence the reproducibility and needs to be taken into consideration since the performance of the gas sensors (sensing response, response and recovery speed) are considerably depending on the working temperature. The working temperature is determined by applying a certain potential on the Pt heating electrode due to Joule heating. As the heating area (300 μm * 300 μm) is limited by the serpentine Pt electrode at the centre of the micro-hotplate, a temperature gradient forms from the centre to the edge of a micro-hotplate according to the COMSOL simulation result of the temperature distribution when applying 2.2 V (Figure S4.2). Therefore, in order to diminish the temperature differential on the sensing material, a smaller area of the sensing materials is better. In addition, when deliberating the size distribution of micro-holes, DFP dots (400 μm) were chosen to assemble porous TPE film for the sake of guarantee the reproducibility.

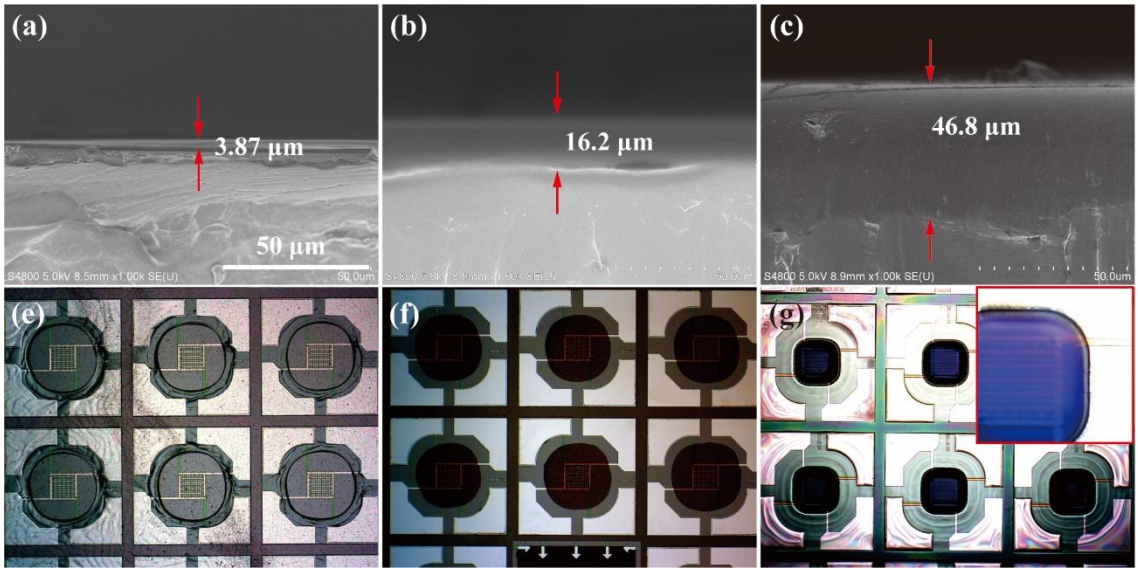

Figure 4.3 Sross-sectional SEM images of TPE film on polyethylene terephthalate (PET) substrate obtained from different concentration of TPE solution: (a) 10%; (b) 18%; (c) 25%; (d) the peel off result of the porous TPE film (10%) after in situ growth of $Ni(OH)_2$ nanowalls; (e) the peel off result of the porous TPE film (10%) after in situ growth of $Ni(OH)_2$ nanowalls and annealed at 400 ℃ for 2 h; (f) the photograph of spin-coated TPE film (25%) after spin-coating ethanol.

4.4.3. Effect of the Concentration of TPE Solution to Assemble Porous TPE Film

Based on the schematic fabrication process, the assembled porous TPE film should be thoroughly peeled off after growth in situ of the $Ni(OH)_2$ nanowalls. Thus, the effect of thickness of the TPE film was studied by assembling porous TPE films with different concentration of TPE solution (10, 18 and 25 wt%). The thicknesses of the TPE film increased from 3.84 μm to 46.8 μm when increasing the concentration of TPE solution owing to increased viscosity of the TPE solution (Figure 4.3 a-c). Figures 4.3d and e reveal the peeling-off results of the TPE film based on 10% and 18% TPE solutions. Compared with thicker TPE film, the thinner one obtained from 10% TPE solution was failed to peel off from the micro-hotplate wafer due to the enhanced interconnection after growth of $Ni(OH)_2$ nanowalls. For the 25% TPE solution, it was failed to obtain the porous TPE film due to the increased thickness

of the TPE film which is covered on the surface of the micro-hotplate wafer as well as the surface of the water droplets. Although spin-coated ethanol can dissolve ultrathin TPE film covered on the surface of water droplets to form the micro-holes, the solubility of TPE in ethanol is limited [26]. So even the water droplets can insulate the DFP dots from the TPE film (inset picture in Figure 4.3f)), the TPE film still remained and covered on the surface of water droplet after spin-coating ethanol (Figure 4.3f). Therefore, the 18% TPE solution was chosen to assemble porous TPE film.

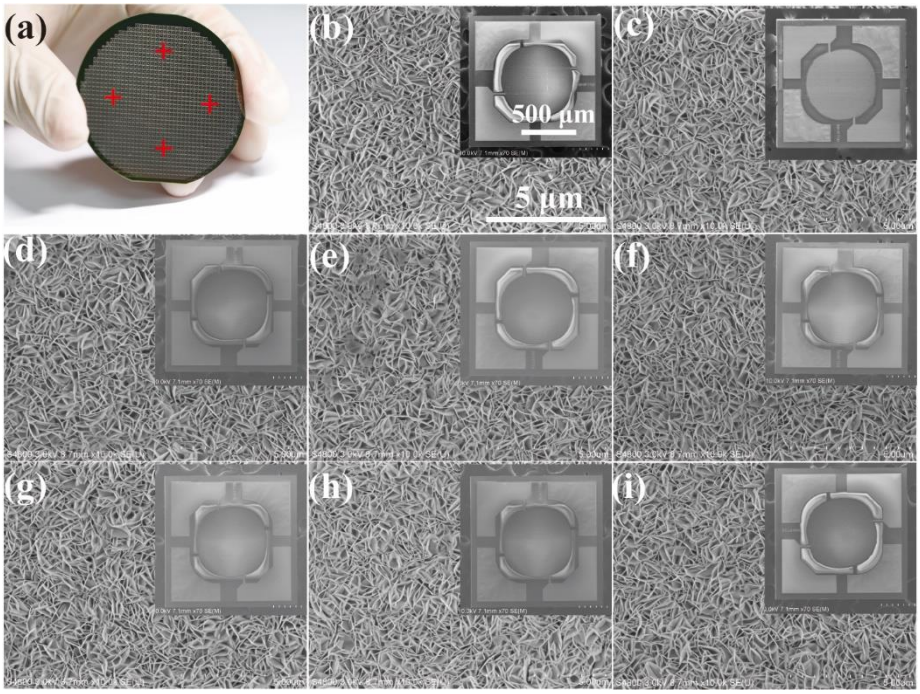

Figure 4.4 (a) The optical picture of wafer-scale micro-hotplate; (b-i) SEM images of 8 sensors which are randomly chosen in the marked area of the wafer-scale micro-hotplate. Scale bar of sensor chip is 500 μm and for NiO nanowalls is 5 μm.

4.4.4. Structure and Morphology Characterization

Crystal structures of $Ni(OH)_2$ nanowalls on the silicon substrate before and after annealing treatment were further verified by X-ray Diffraction (XRD) (Figure S4.3). All of the reflection peaks of $Ni(OH)_2$ nanowalls are consistent with hexagonal crystal phase of β–$Ni(OH)_2$ (JCPDS file NO.14-0117). After annealing treatment, the diffraction index peaks correspond with

standard values (JCPDS file NO. 47-1049), indicating that the $Ni(OH)_2$ nanowalls are completely converted to NiO nanowalls. The unexpected peak at 69° is ascribed to the diffraction of silicon substrate. Eight gas sensors were randomly picked out from the four labelled areas on the micro-hotplate wafer and characterised using scanning electron microscopy (SEM; Figure 4.4) after annealing at 400 ℃ under Ar atmosphere and finishing wet-etching process. These images reveal that NiO nanowalls are oriented vertically at the centre of the micro-hotplate and exhibit uniform morphology without obvious cracks either in overall view of sensor or in local zoom images of the NiO nanowalls.

4.4.5. Mechanism of formation of Porous TEP Film

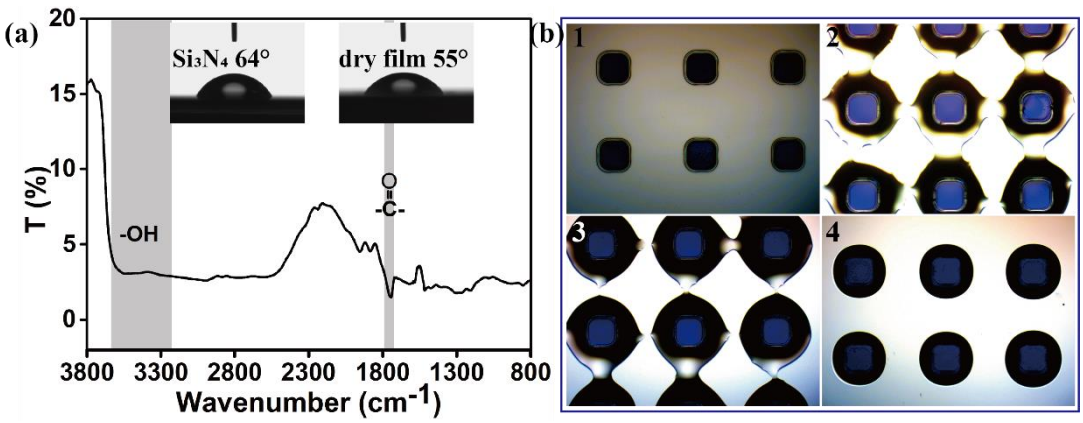

Figure 4.5 (a) FTIR result of DFP after Standard UV exposure (10 s) and contact angle results of Si_3N_4 and DFP (inset pictures); (b) a series of optical images of process (from stage 1 to stage 4) of forming water droplets based on template-guided controllable de-wetting method using 400 μm DFP dots.

In order to further investigate the mechanism of assembly of water droplet array based on template-guided method, a piece of DFP film was characterized with Fourier transform infrared (FTIR) spectroscopy and water contact angle after exposing to standard ultraviolet (UV) (Figure 4.5a). As the DFP is mainly consisted of epoxy- or acrylic-based composites indicating that it contains abundant carboxyl and hydroxyl groups [29, 30]. The FTIR data of the DFP film also confirms this result, which shows a very strong broad absorption peak (around

3200 cm^{-1} to 3650 cm^{-1}) and a narrow peak (around 1740 cm^{-1}) assigned to hydroxyl and carboxyl groups, respectively. Those function groups guarantee the DFP has a better hydrophilicity compared with Si_3N_4 which is confirmed by the water contact angle results (Figure 4.5a). This hydrophilic property ensures that the DFP dots can efficiently pin water during the template-guided controllable de-wetting process. The specific process of assembling water droplets based on 400 μm DFP dots (Figure 4.5b) has four different stages: (1) before spin-coating water; (2) ruptures appear at the water film; (3) contact lines gradually recede according to the contour of the DFP dots; (4) the water film completely breaks into discrete water droplets covering on the surface of DFP dots. Obviously, ruptures appear at the central point of diagonal of DFP dots because the water film preferentially ruptures at thinnest locations during de-wetting [12, 13]. De-wetting is a very common phenomenon in nature that liquid films break into hemi-spherical cap droplets and remain where there are surface defects and artificially-induced defects, which can provide nucleation sites (*e.g.*, patterned microstructure) due to a heterogeneous mechanism [11-13, 31, 32]. Hence, the patterned DFP dots will not only work as pinners to pin water, but also offer the nucleation sites. Similar phenomena can be observed by varying the size of the DFP dots (Figure S4.4). The size, shape and location of the water droplets are determined by the DFP dots and most importantly the existence of DFP dots can also work as a fixer to ensure that the anchored water droplets will not shift to other locations when spin-coating TPE solution. As the periodicity (λst) of the DFP dots is constant (1200 μm) and identical to the length of micro-hotplate, the distance between the edge of adjacent DFP dots (ld) varies via tuning the size of the DFP dots. Thus, the de-wetting process becomes progressively slower by increasing the size of DFP dots due to enhanced capillary force between the adjacent DFP dots, resulting from the decreased ld. When the size of the DFP dots decreasing to 300 μm, it is not easy to precisely control the time of

drop casting and spin-coating of the TPE solution (within 1-2 s), because the de-wetting process is too fast resulted in a relatively poor uniformity of the micro-holes (Figure 4.2).

4.4.5. Sensing Performance of Fabricated Sensors

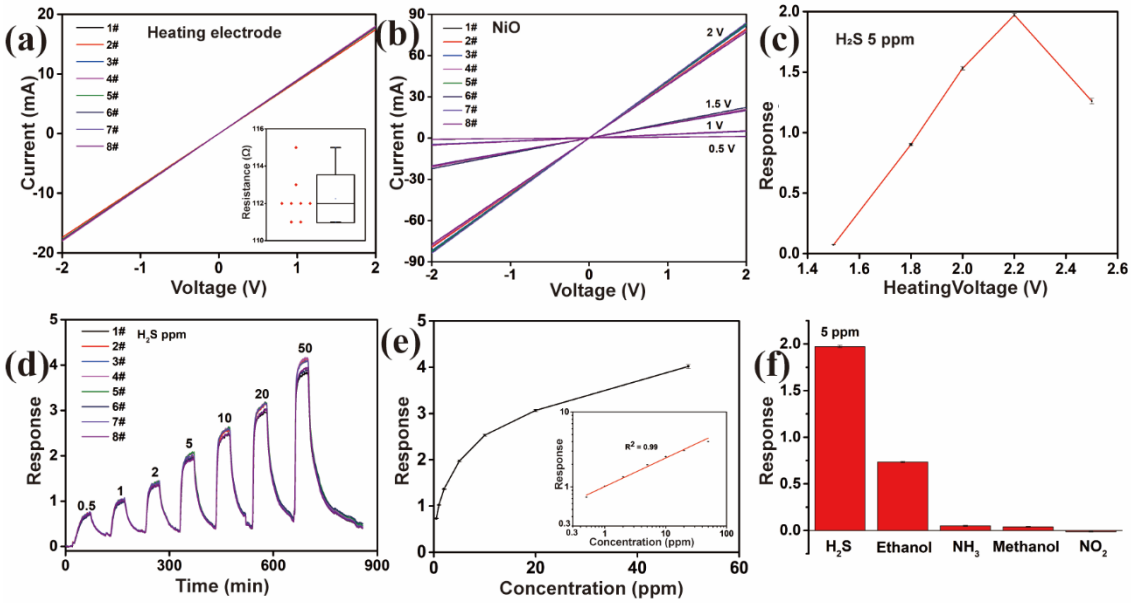

Figure 4.6 (a) I-V curves of heating electrodes of eight gas sensors from -2 V to 2 V (inset graph is the box chart of resistance of heating electrodes); (b) I-V curves of eight sensors at different heating voltage; (c) heating voltage dependent responses of eight gas sensors to 5 ppm H_2S; (d) dynamic response of eight gas sensors to different H_2S concentrations; (e) scatter graph of response to various H_2S concentrations (inset graph is the linear relationship of logarithm of response with the logarithm of H_2S concentrations); (f) response of eight gas sensors toward different gases and the concentration is 5 ppm.

Eight gas sensors were randomly picked out form the wafer and wire-bonded for measurement. The reproducibility and uniformity of electrical and sensing performances of eight gas sensors were presented in Figure 4.6. The I-V curves of the heating electrode are almost overlapping (Figure 4.6a) indicating that the fabricated micro-hotplates possess great uniformity and reproducibility with a very small RSD value (< 0.8%). Figure 4.6b demonstrates the I-V curves of eight sensors at different heating voltages after in situ growth of patterned

NiO nanowalls at the centre of micro-hotplates. The resistance of NiO nanowalls decreases with increasing heating voltage due to their semiconducting property. The RSD values of eight gas sensors under different heating voltages (0.5, 1, 1.5, and 2.0 V) were 3.4%, 2.9%, 3.6%, and 2.9%, respectively, demonstrating a good electrical uniformity. This is a precondition to ensure good uniformity and reproducibility of the gas sensors. Figure 4.6c illustrates the sensing responses of the selected sensors to 5 ppm H_2S by varying the heating voltage (1.5 – 2.2 V). Evidently, the response of the 8 sensors sharply increased by increasing the heating voltage and reached a maximum value at 2.2 V, and then steeply declined. Therefore, all other measurements were made at 2.2 V. Figure 4.6d shows the dynamic response of the sensors to different concentrations of H_2S. Obviously, all sensors also demonstrate high sensing performance uniformity and reproducibility with a small RSD (< 5%). The relationship of response and H_2S concentrations is displayed in Figure 4.6e. The response rapidly increases at low H_2S concentrations (< 10 ppm) and then become slower with further increasing H_2S concentrations as H_2S adsorption gradually reaches saturation according to Langmuir adsorption theory. However, there is a good relationship between the response in logarithm scale and H_2S concentrations (R^2 = 0.99, inset graph of Figure 4.6e). The response of the gas sensors to different gases is illustrated in Figure 4.6f. All the gas sensors can selectively detect H_2S. The sensing mechanism of NiO nanowalls based sensor toward H_2S may be described as follows. NiO is a p-type metal oxide semiconductor, which contains many oxygen vacancies. When the sensor stays in air, O_2 molecules will adsorb onto the surface of NiO nanowalls and extract electrons from Ni^{2+} to form ionized oxygen species such as O^{2-}, O_2^-, and O^- and the Ni^{2+} is oxidized to the Ni^{3+} [33, 34]. Thus, the resistance of the sensor is low in the air attributing to the increased hole concentration of NiO nanowalls. When injecting H_2S, the H_2S molecules will react with the ionized oxygen species and donate trapped electrons back to NiO nanowalls causing the decrease of hole concentration. Finally, the resistance of the sensor increases. The

selectivity toward H_2S is possibly ascribing to low bond dissociation energy of H-S compared with other tested interference gases, it means that H-S can be easily broken and oxidized to form SO_2 [35, 36].

4.5 Conclusion

"Top-down" & "bottom-up" strategies were combined to fabricate wafer-scale miniaturized gas sensors. "Top-down" strategy (MEMS fabrication techniques) guarantees the fabricated micro-hotplates with great reproducibility for further in situ growth of $Ni(OH)_2$ nanowalls. The template-guided controllable de-wetting method was utilized to integrate "top-down" and "bottom-up" strategy by assembling the uniform porous TPE film to serve as the mask for growing $Ni(OH)_2$ nanowalls. In order to obtain porous TPE film with uniform micro-holes, the effects of the size of DFP dots and the concentration of TPE solution were systematically studied. Thus, a 400 μm DFP dots and 18% TPE solution were selected to assemble porous TPE film (RSD of the size of micro-holes < 3.5%). The reproducibility and uniformity of obtained gas sensors were studied by randomly choosing 8 gas sensors at different sites via various methods such as SEM, I-V curves of heating electrodes and also the NiO nanowall, and dynamic gas response. Notably, the obtained gas microsensors showed great reproducibility of electrical properties (RSD < 0.8%, n=8) and response toward real-time H_2S detection (RSD <3.5%, n=8).This fabrication strategy shows great potential to fabricate wafer-scaled miniaturized gas sensors based on different sensing materials due to the chemical and thermal stability of TPE film for practical applications. However, the drawback of the metal oxide-based chemiresistive gas sensors is energy consumption because external power sources are required to drive the sensor and provide high working temperature. Thus, development of novel self-powered gas sensors is a potential approach to address this problem.

4.6 References

[1] W. Zou, B. Quan, K. Wang, L. Xia, J. Yao, Z. Wei, Patterned growth of polyaniline nanowire arrays on a flexible substrate for high-performance gas sensing, Small 7(2011) 3287-3291.

[2] V.D. Tran, D.H. Nguyen, V.D. Nguyen, V.H. Nguyen, Chlorine Gas Sensing Performance of On-Chip Grown ZnO, WO_3, and SnO_2 Nanowire Sensors, ACS Appl. Mater. Interfaces 8(2016) 4828-4837.

[3] M.R. Niazi, R. Li, E. Qiang Li, A.R. Kirmani, M. Abdelsamie, Q. Wang, W. Pan, M.M.Payne, John.E. Anthony, D.M. Smilgies, S.T. Thoroddsen, E.P. Giannelis, A. Amassian, Solution-printed organic semiconductor blends exhibiting transport properties on par with single crystals, Nat. Commun. 6(2015) 8598.

[4] G. Azzellino, A. Grimoldi, M. Binda, M. Caironi, D. Natali, M. Sampietro, Fully inkjet-printed organic photodetectors with high quantum yield, Adv. Mater. 25(2013) 6829-6833.

[5] H. Yabu, M. Shimomura, Preparation of Self-Organized Mesoscale Polymer Patterns on a Solid Substrate: Continuous Pattern Formation from a Receding Meniscus, Adv. Funct. Mater. 15(2005) 575-581.

[6] J. Chang, C. Chi, J. Zhang, J. Wu, Controlled growth of large-area high-performance small-molecule organic single-crystalline transistors by slot-die coating using a mixed solvent system, Adv. Mater. 25(2013) 6442-6447.

[7] X. Gu, L. Shaw, K. Gu, M.F. Toney, Z. Bao, The meniscus-guided deposition of semiconducting polymers, Nat. Commun. 9(2018) 534.

[8] P.S. Jo, A. Vailionis, Y.M. Park, A. Salleo, Scalable Fabrication of Strongly Textured Organic Semiconductor Micropatterns by Capillary Force Lithography, Adv. Mater. 24(2012) 3269–3274.

[9] M. Cavallini, D. Gentili, P. Greco, F. Valle, F. Biscarini, Micro- and nanopatterning by lithographically controlled wetting, Nat. Protoc. 7(2012) 1668-76.

[10] J. Feng, X. Jiang, X. Yan, Y. Wu, B. Su, H. Fu, J. Yao, L. Jiang, "Capillary-Bridge Lithography" for Patterning Organic Crystals toward Mode-Tunable Microlaser Arrays, Adv. Mater. 29(2017) 1603652.

[11] H. Li, B.C. Tee, J.J. Cha, Y. Cui, J.W. Chung, S.Y. Lee, Z. Bao, High-mobility field-effect transistors from large-area solution-grown aligned C60 single crystals, J. Am. Chem.Soc. 134(2012) 2760-2765.

[12] N. Bhandaru, P.S. Goohpattader, D. Faruqui, R. Mukherjee, A. Sharma, Solvent-vapor-assisted dewetting of prepatterned thin polymer films: control of morphology, order, and pattern miniaturization, Langmuir 31(2015) 3203-3214.

[13] D. Gentili, G. Foschi, F. Valle, M. Cavallini, F. Biscarini, Applications of dewetting in micro and nanotechnology, Chem. Soc. Rev. 41(2012) 4430-4443.

[14] R. Eckstein, M. Alt, T. Rodlmeier, P. Scharfer, U. Lemmer, G. Hernandez-Sosa, Digitally Printed Dewetting Patterns for Self-Organized Microelectronics, Adv. Mater. 28(2016) 7708-7715.

[15] X. Zhang, J. Jie, W. Deng, Q. Shang, J. Wang, H. Wang, X. Chen, X. Zhang, Alignment and Patterning of Ordered Small-Molecule Organic Semiconductor Micro-/Nanocrystals for Device Applications, Adv. Mater. 28(2016) 2475-2503.

[16] K.S. Park, J. Baek, Y. Park, L. Lee, Y.E. Lee, Y. Kang, M.M Sung, Inkjet-Assisted Nanotransfer Printing for Large-Scale Integrated Nanopatterns of Various Single-Crystal Organic Materials, Adv. Mater. 28(2016) 2874-2880.

[17] T. Kida, S. Fujiyama, K. Suematsu, M. Yuasa, K. Shimanoe, Pore and Particle Size Control of Gas Sensing Films Using SnO_2 Nanoparticles Synthesized by Seed-Mediated Growth: Design of Highly Sensitive Gas Sensors, J. Phys. Chem. C 117(2013) 17574-17582.

[18] H.S. Lee, H.S. Rhee, B.T. Ahn, Improved Morphological Stability of $CoSi_2$ Layer by In Situ Growth on Polycrystalline Silicon Using Reactive Chemical Vapor Deposition, J. Electrochem. Soc. 149(2002) 16-20.

[19] L. Cao, D.N. Barsic, A.R. Guichard, M.L. Brongersma, Plasmon-Assisted Local Temperature Control to Pattern Individual Semiconductor Nanowires and Carbon Nanotubes, Nano lett. 11(2007) 3523-3527.

[20] J. Yeo, S. Hong, G. Kim, H. Lee, Y.D. Suh, I. Park, C.P. Grigoropoulos, S.H. Ko, Laser-Induced Hydrothermal Growth of Heterogeneous Metal-Oxide Nanowire on Flexible Substrate by Laser Absorption Layer Design, ACS Nano 2015(2015) 6059-6068.

[21] J.B. In, H.J. Kwon, D. Lee, S.H. Ko, C.P. Grigoropoulos, In situ monitoring of laser-assisted hydrothermal growth of ZnO nanowires: thermally deactivating growth kinetics, Small 10(2014) 741-749.

[22] J. Fang, Y. Zhu, D. Wu, C. Zhang, S. Xu, D. Xiong, P. Yang, L. Wang, P. Chu, Gas sensing properties of NiO/SnO_2 heterojunction thin film, Sens. Actuators B Chem. 252(2017) 1163-1168.

[23] H. Ren, W. Zhao, L. Wang, S.O. Ryu, C. Gu, Preparation of porous flower-like SnO_2 micro/nano structures and their enhanced gas sensing property, J. Alloy. Compd. 653(2015) 611-618.

[24] Y. Chen, L. Yu, D. Feng, M. Zhuo, M. Zhang, E. Zhang, Z. Xu, Q. Li, T. Wang, Superior ethanol-sensing properties based on Ni-doped SnO_2 p–n heterojunction hollow spheres, Sens. Actuators B Chem. 166-167(2012) 61-67.

[25] W. Li, Y. Nie, J. Zhang, Z. Wang, D. Zhu, Q. Lin, B. Yang, Y. Wang, Fabricating a binary pattern of ordered two-dimensional luminescent (mdppy)BF arrays by dewetting, J. Mater. Chem. 16(2006) 2135-2141.

[26] L. Li, Y. Bai, L. Li, S. Wang, T. Zhang, A Superhydrophobic Smart Coating for Flexible and Wearable Sensing Electronics, Adv. Mater. 29(2017) 1702517.

[27] L. Li, H. Xiang, Y. Xiong, H. Zhao, Y. Bai, S. Wang, F. Sun, M. Hao, L. Liu, T. Li, Z. Peng, J. Xu, T. Zhang, Ultrastretchable Fiber Sensor with High Sensitivity in Whole Workable Range for Wearable Electronics and Implantable Medicine, Adv. Sci. 5(2018) 1800558.

[28] D. Meng, D. Liu, G. Wang, Y. Shen, X. San, M. Li, F. Meng, Low-temperature formaldehyde gas sensors based on NiO-SnO_2 heterojunction microflowers assembled by thin porous nanosheets, Sens. Actuators B Chem. 273(2018) 418-428.

[29] A.V. Quintero, D. Briand, N.F. de Rooij, Effect of low-temperature processing on dry film photoresist properties for flexible electronics, J. Polym. Sci., Part B: Polym. Phys 51(2013) 668-679.

[30] L.E. Fissi, D. Vandormael, L.A. Francis, Direct assembly of cyclic olefin copolymer microfluidic devices helped by dry photoresist, Sens. Actuators A: Phys. 223(2015) 76-83.

[31] A. Sharma, G. Reiter, Instability of Thin Polymer Films on Coated Substrates: Rupture, Dewetting, and Drop Formation, J. Colloid. Interface Sci. 178(1996) 383-399.

[32] R. Verma, A. Sharma, Defect Sensitivity in Instability and Dewetting of Thin Liquid Films: Two Regimes of Spinodal Dewetting, Ind Eng Chem Res, 46(2007) 3108-3118.

[33] G. Li, X. Wang, H. Ding, T. Zhang, A facile synthesis method for $Ni(OH)_2$ ultrathin nanosheets and their conversion to porous NiO nanosheets used for formaldehyde sensing, RSC Adv. 2(2012) 13018.

[34] R. Miao, X. Yu, W. Zeng, Novel NiO flower-like microspheres with abundant nanoparticles adhering to the petals: Hydrothermal synthesis and their gas sensing properties, Mate. Lett. 173(2016) 107-110.

[35] Breck, D. W. in Zeolite Molecular Sieves: Structure, Chemistry, and Use, John Wiley and Sons. 1974, Ch. 8.

[36] Dean, J. A., in Lange's Handbook of Chemistry 70 edn, McGraw-Hill Professional, 2004, Ch. 4.

4.7. Supplementary Data

In situ Growth of Patterned NiO Nanowalls for Wafer-scaled Miniaturized Gas Sensors Design and Fabrication

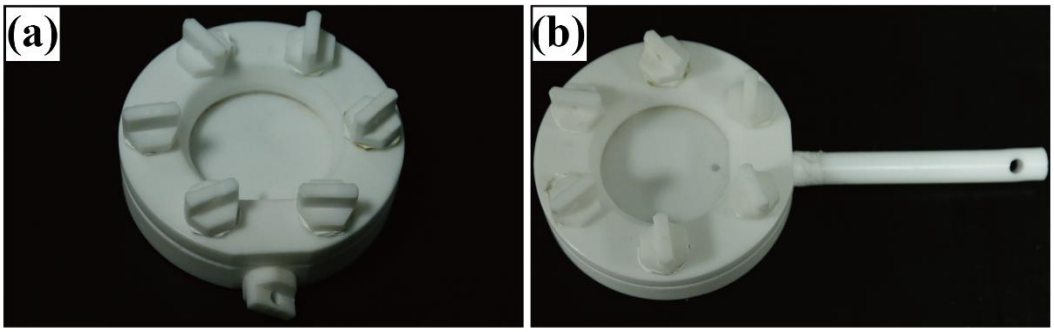

Figure S 4.1 Pictures of a designed fixture (a) is used for in situ growth of $Ni(OH)_2$ nanowalls; (b) is used for wet-etching of silicon on the back of micro-hotplate wafer.

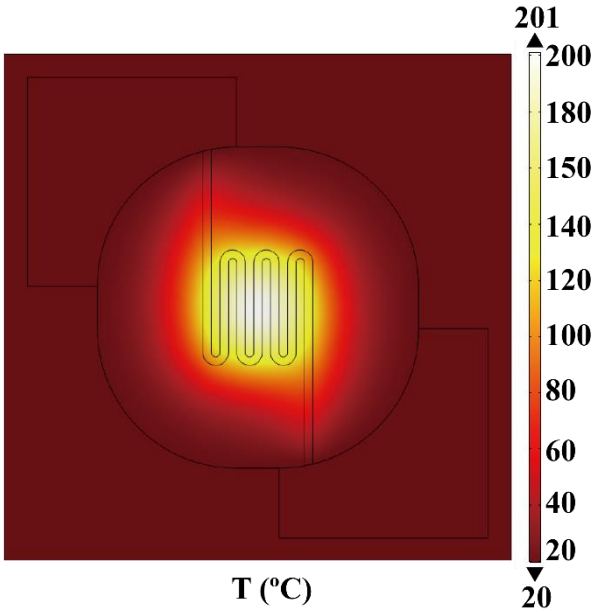

Figure S 4.2 Temperature distribution simulation result on micro-hotplate.

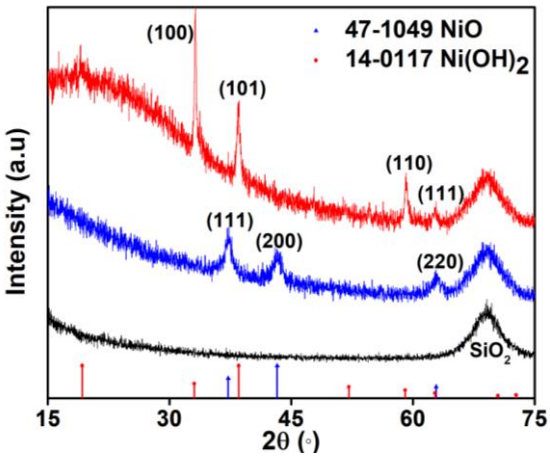

Figure S 4.3 XRD patterns of grown $Ni(OH)_2$ and NiO nanowalls on silicon substrate with a layer of SiO_2.

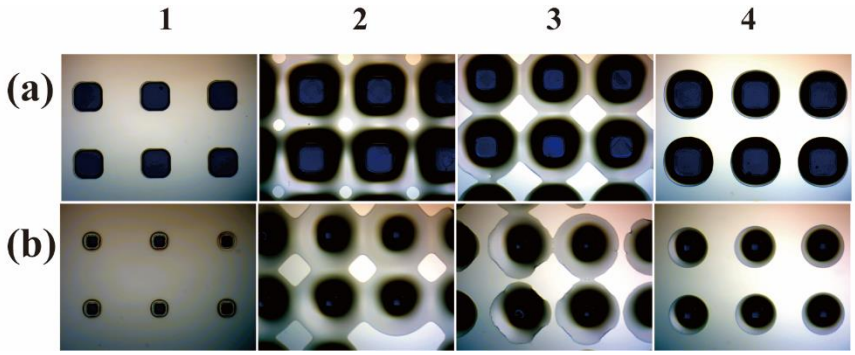

Figure S 4.4 A series of optical images of process (from stage 1 to stage 4) of forming water droplet array based on template-guided method using different size of DFP dots (500 μm (a), and 300 μm (b), respectively).

Chapter 5: Design of Photovoltaic Self-Powered Gas Sensor Based on Single-Walled Carbon Nanotubes/Si p-n Heterojunction

5.1. Abstract

Different from the chemiresistive gas sensors reported in this thesis, which are driven by external power source, a novel device structure was proposed to construct photovoltaic self-powered H_2S sensor based on p-type single-walled carbon nanotubes (SWNTs) and n-type silicon (n-Si) heterojunction. The energy from visible light suffice to drive the device owing to a built-in electric field (BEF) induced by the differences between Fermi levels of SWNTs and n-Si. The device showed a linear response to 100-800 ppb H_2S (R^2 = 0.996) when illuminated under visible light (λ = 600 nm, P = 1.8 mW/cm^2). Compared with the conventional chemiresistive gas sensor based on SWNTs, the sensing response of the photovoltaic self-powered gas sensor enhanced 4.5 folds, and the response time also improved dramatically. The influence of different wavelength of illuminated light to sensing performance was investigated.

Author contributions: Lin Liu has got the permission from other co-authors for this paper to her thesis. All the paper work and data analysis are finished by Lin Liu and most of the data including SEM, EDXS, sensing performance are also collected by Lin Liu.

5.2. Introduction

There is a pressing need for novel gas sensing technologies for addressing the problems of energy crises and air pollution. Previous efforts mainly focused on reducing the sensor's power consumption via lowing the operation temperature. The most popular method is synthesizing novel nanomaterials and nano-composites to construct room temperature gas sensors [1-4]. Single-walled carbon nanotubes (SWNTs) have shown great sensitivity to various gases with a series of unique properties such as high mobility (~10^5 $cm^2/(Vs)$), on/off current ratio (>10^5), current carrying capacity (>10^9 A/cm^2) and large surface area [5-10]. Dube et al. [9] presented gas sensors based on carbon nanotube and systematically investigate the electrical response and sensing mechanism of the sensor to various gases. Zhou et al. [10] reported a printed thin-film transistor with high sensing response (~96%) and fast response (30 s) to 60 ppm NO_2. In addition, it is acknowledged that light illumination may help lower power consumption in gas sensors. Comini et al. [11] reported that UV illumination greatly enhanced the gas sensing performance (*e.g.*, sensitivity and response and recovery time) of In_2O_3 and SnO_2 by changing the concentration of adsorption center and the density of free carriers. Several studies also demonstrated that UV irradiation can diminish the power consumption by reducing the working temperature of devices [12-14].

Although, there are many room temperature gas sensors available such as the chemiresistive [5, 15, 16], field-effect-transistive1 and capacitive gas sensors [17], all of them are driven by applying a considerable source-drain bias voltage (V_{ds}) which requires external power. Therefore, developing self-powered devices has attracted considerable attention. Compared with conventional semiconductor material-based gas sensors, self-powered sensors can dramatically reduce power consumption as well as the required space for integration. Triboelectric nanogenerators (TENGs), which can harvest mechanical energy from ambient environment to power micro-devices or generate a read-out signal, have been intensively

investigated [18-20]. A few recent works have also implemented self-powered devices which are activated by light based on p-n heterojunction [21-24]. The existing BEF can separate photogenerated carriers which facilitate to drive devices under light illumination. For example, Hoffmann et al. [22,23] reported two kinds of self-powered gas sensors based on p-Si/n-ZnO and p-Si/n-ZnO@CdS via complicate fabrication processes, respectively. The sensing performance of p-Si/n-ZnO@CdS-based sensor is much higher than that of p-Si/n-ZnO-based sensor, as the decorated CdS nanoparticals (~2.4 eV) can provide more reactive electrons to ZnO nanorods due to photogenerated carriers after absorbing photons. Hence, to effectively construct self-powered gas sensor based on p-n heterojunction, the carrier mobility of the sensing materials and the facile fabrication process must be considered. In this study, based on our previous work [24], p-SWNTs and n-Si were employed to fabricate photovoltaic self-powered gas sensor with a simple p-n heterojunction structure to address the aforementioned problems. SWNTs are flexible one-dimensional materials can be easily interconnected into two-dimensional networks to serve as the transparent electrode for charge collection and transport and also work as the sensing materials for gas molecules detection [25]. Compared with the conventional chemiresistive gas sensor based on SWNTs, the sensing response of the photovoltaic self-powered gas sensor enhanced 4.5 folds, and the response time also improved dramatically. The device has showed a linear response to 100-800 ppb H_2S (R^2 = 0.996) when illuminated under visible light (λ = 600 nm, P = 1.8 mW/cm^2). The influence of different wavelength has been investigated by controlling the power density of light as a constant.

5.3. Experimental Section

5.3.1. Fabrication Process

The fabrication of the gas sensor is shown in Figure S5.1. The patterned microelectrodes were fabricated by Micro Electro Mechanical System (MEMS) techniques, which has been reported in our previous work [24]. Briefly, SiO_2 thin layer was removed by reacting ion

etching, followed by sequentially sputtering Ti (~20 nm in thickness) and Au (~150 nm) thin film onto the Si and SiO_2 layer respectively, (FHR, Germany). The distance between the Ti/Au electrodes and bare silicon was controlled to be 40 μm. SWNTs powder ((7, 6) chirality, carbon >90%, ≥77% (semiconducting carbon nanotubes), Sigma) was purified, refer to our previous work, before being well dispersed in dimethylformamide (DMF) via tip sonication [26]. The as-prepared SWNTs dispersion was then drop-cast onto the prefabricated sensor chip to form a SWNT thin film on the surface of silicon. To totally remove the solvent left in SWNT thin film and reduce the contact barrier between SWNTs and the Ti/Au electrode, the prepared devices were annealed in a tube furnace under pure Ar gas at 300 ^{o}C for 20 minutes. For comparison, sensors based on SWNTs-only and n-Si-only were fabricated by sputtering source-drain electrodes on the both sides of SWNTs-only film and bare n-Si, respectively, and then annealed at the same condition.

5.3.2. Characterization

The morphology of SWNTs films were characterized by scanning electron microscopy (SEM, JEOL Hitachi-s4800). Current density-Voltage (J-V) curves were measured using Agilent B1500A with potential ranging from -2 V to 2 V at room temperature, while the open-circuit voltage-time (V_{oc}-t) curves were measured by using an electrochemical workstation (CHI660D, Chenhua Shanghai, China) with open circuit voltage-time mode at zero bias. The LED light UVEC-4(SHENZHEN LAMPLIC TECH CO., LTD) was used as the light source, and the power density of the light can be regulated from 0 mW/cm^2 to 50 mW/cm^2.

5.4. Results and Discussion

5.4.1. Morphology Characterization

Figure 5.1a depicts the schematic of the photovoltaic self-powered H_2S sensor based on SWNTs/Si heterojunctions. One Ti/Au electrode (marked as electrode B) directly contacts with n-Si at the bottom, while the other electrode (marked as electrode A) is deposited on SiO_2 layer

and contacts with the SWNT thin film. The whole contacting area of the SWNTs/Si is 500 * 500 μm^2, which is composed of five identical parts with the same area (each part is 100 * 500 μm^2). Figure 5.1b demonstrates the SEM image of the device based on SWNTs/Si. As shown in the Figure 5.1c there is an obvious ledge at the interface of Si and SiO_2, indicating n-Si is connected by a uniform porous and mesh-like SWNT film. The EDXS results of two locations (Si/SWNTs and Si/SiO_2/SWNTs) are tested and showed in Figure S5.2. The contents of C atom in both locations are very low which can indicate that the SWNT film is very thin.

Figure 5.1d displays the current density-voltage (J-V) curves of the SWNTs/Si heterojunction in dark and light state (λ = 600 nm, P = 1.8 mW/cm^2). In the dark, the device demonstrates rectification characteristics, which is caused by the heterojunction formed between SWNTs and n-Si due to the differential Fermi level of SWNTs and n-Si [27, 28]. When switch to light state, a photogenerate current density (J_{sc}) is observed (around 0.81 mA/cm^2) at zero bias. The power conversion efficiency (PCE) of the device is ~3.5%, which is enough to power the sensor for real-time gas sensing. Several recent reports about pristine SWNT/Si based solar cells also reveal that the PCEs are within 5% [29, 30]. However, the I-V curves of SWNTs-only and n-Si-only sensors show linear relationship, which indicates an ohmic contact formed in these sensors (Figure S5.3).

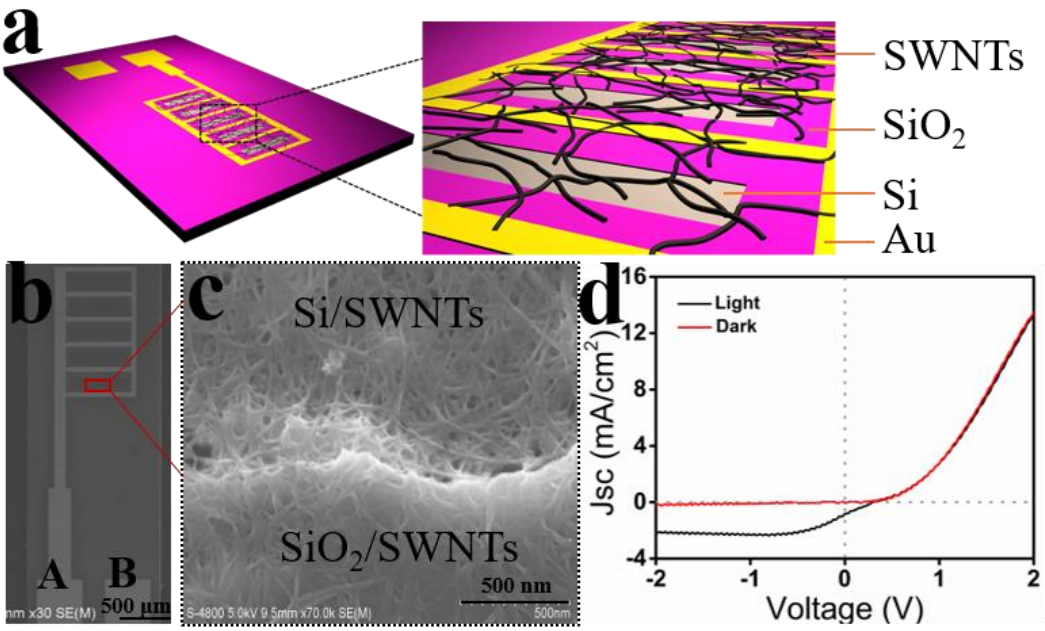

Figure 5.1 (a) The schematic graph of photovoltaic self-power H_2S sensor based on SWNTs/Si heterojunction. Electrode A (Ti/Au) is sputtered on SiO_2 layer, while Electrode B (Ti/Au) is on the bare n-Si. (b), (c) SEM images of device and the formed SWNT film. (d) The current density-voltage (J-V) curves of self-power H_2S sensor in dark and illuminated circumstance (λ = 600 nm, P = 1.8 mW/cm^2, applied potential: -2 V to 2 V). The red line is the J-V curve of self-power sensor at dark state, while the dark line is J-V curve when exposing to light.

5.4.2. Sensing Performance of Photovoltaic Self-powered Sensor

To measure the sensing characteristics of the self-powered sensor to H_2S, the open-circuit voltage-time (V_{oc} -t) curve of the device under the visible light illumination (λ = 600 nm, P = 1.8 mW/cm^2) is measured at zero bias. The micro-sensors were placed in a small transparent quartz chamber (the volume of chamber is ~0.4 mL) with an airscoop and airout, so the visible light can go through the quartz and excite the device (Figure S5.4). The electrode A and B are wired bonded to the ceramic dual in-line package (CERDIP) for electrical measurement. By diluting H_2S gas with dry air via mass flow controller (MFC), we can control the H_2S gas

concentration. In the dry air atmosphere, the V_{oc} reaches 181 mV under illumination (λ =600 nm, P = 1.8 mW/cm^2), which is shown in Figure 5.2a. After exposing to H_2S, the V_{oc} of the device shows a sharp decrease and then reaches the steady state within 54 s. With the increase of H_2S gas concentration, the V_{oc} shows a decreasing trend, shown in Figure 5.2a. The detection limit is as low as 100 ppb. The sensing response (S) of the photovoltaic self-power H_2S sensor is defined as: $S = (|V_g-V_0|)/V_0$, in which V_0 and V_g are the value of V_{oc} in dry air and target gas under illumination, respectively. However, when switch to dark state, the sensor based on SWNTs/Si has no response to H_2S (Figure S5.5). As shown in Figure 5.2b, the response of the device has a linear relationship with the H_2S concentration ranging from 100 ppb to 800 ppb (the linear correlation is 0.996). For comparison, the chemiresistive sensors based on SWNTs-only and n-Si-only show negligible response to H_2S under illumination at zero bias (Figure 5.2c and 5.2d).

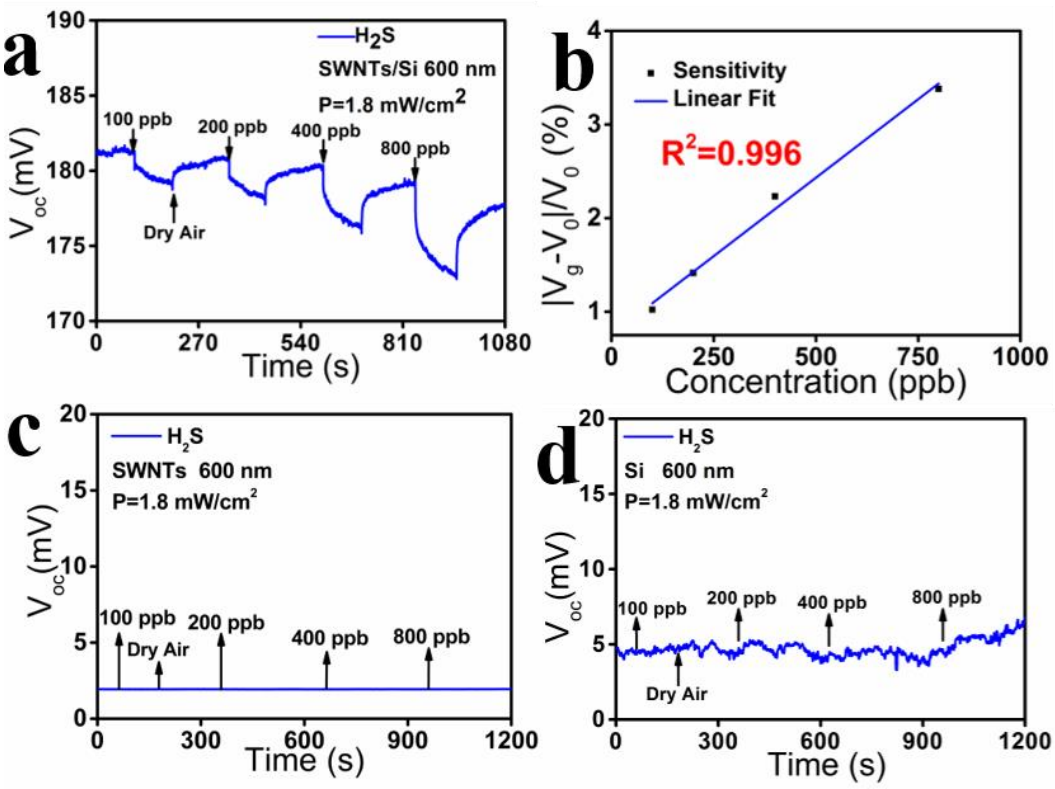

Figure 5.2 (a), (c), (d) The response of devices to different H_2S concentrations based on SWNTs/Si, SWNTs-only, and n-Si-only, respectively. The measurements are carried at zero bias with light illumination (λ = 600 nm, P = 1.8 mW/cm^2) to monitor the changing of open-circuit voltage (V_{oc}). (b) The response of the device to difference H_2S concentration under 600 nm light and its corresponding fitting curve (R^2=0.996).

The difference among the three devices is because SWNTs can form p-n heterojunctions with n-Si, and then a strong enough BEF (~0.55 eV) will be formed at the interface of p-SWNTs and n-Si due to the different work function of n-Si (~4.25 eV) and p-SWNTs (~4.8 eV) [31-33]. However, n-Si-only and SWNTs-only form Ohmic contact with the electrodes (Figure S5.3). That means although sensors based on n-Si-only and SWNTs-only can produce photogenerated hole-electron pairs under the light illumination, the photogenerated holes cannot be separated from photogenerated electrons and cannot react with H_2S owing to the lack of BEF. Therefore, electric signal changes of the devices based on n-Si-only and SWNTs-only

are difficult to detect. In addition, the response of the photovoltaic self-powered device shows 4.5 folds higher response to H_2S (S = 2.23% for 400 ppb H_2S) than the conventional H_2S sensor based on SWNTs which works under the bias of 2 V through measuring the resistance changes (S = 0.49% for 400 ppb H_2S) (Figure S5.6). Due to the illumination, the number of the holes in SWNTs reacting with H_2S increases [13]. Meanwhile, the response and recovery time of the photovoltaic self-powered sensor also are dramatically improved. The stability of the sensor based on SWNTs/Si were also investigated by comparing the sensitivities of an as-prepared sensor and the sensor storing for 5 days. After five days the response of the sensor to 200 ppb H_2S decreases from 1.42% to 1.14% (Figure S5.7). Several publications also confirmed that the stability of the devices based on Si/carbon (including C_{60}, CNT and graphene) needs to be optimized for their practical applications [25, 34, 35].

5.4.3. Influence of the Wavelength of Illuminated Light

The influence of the wavelength on the performance of the self-powered device was investigated (Figure 5.3a). By applying the same power density of light and varying the wavelength of light (420 nm and 600 nm), the response of the device decreases with the increase of the wavelength. According to the Figure 5.3a, the recovery time of the device is much shorter when illuminating under 600 nm than 420 nm. This may be caused by the charge redistribution in H_2S molecule owing to the molecule vibrations and electron transition between orbital energy levels when exposed to illumination. G. Vall-llosera et al. [36] found that there are many orbital energy levels existing in H_2S molecular by investigating the photo-fragments resonant S 2p excitations in H_2S. As the existence of abundance energy levels, H_2S can absorb photons ranging from 233 nm to 762 nm, especially in 359 nm – 532 nm [37]. Therefore, we deduced that when H_2S is subjected to the light in the range of 359 nm to 532 nm, such as 420 nm, the H_2S will absorb the light and become more active and react with

photogenerated holes in the SWNT film. Thus, it is too difficult to desorb from the surface of the device.

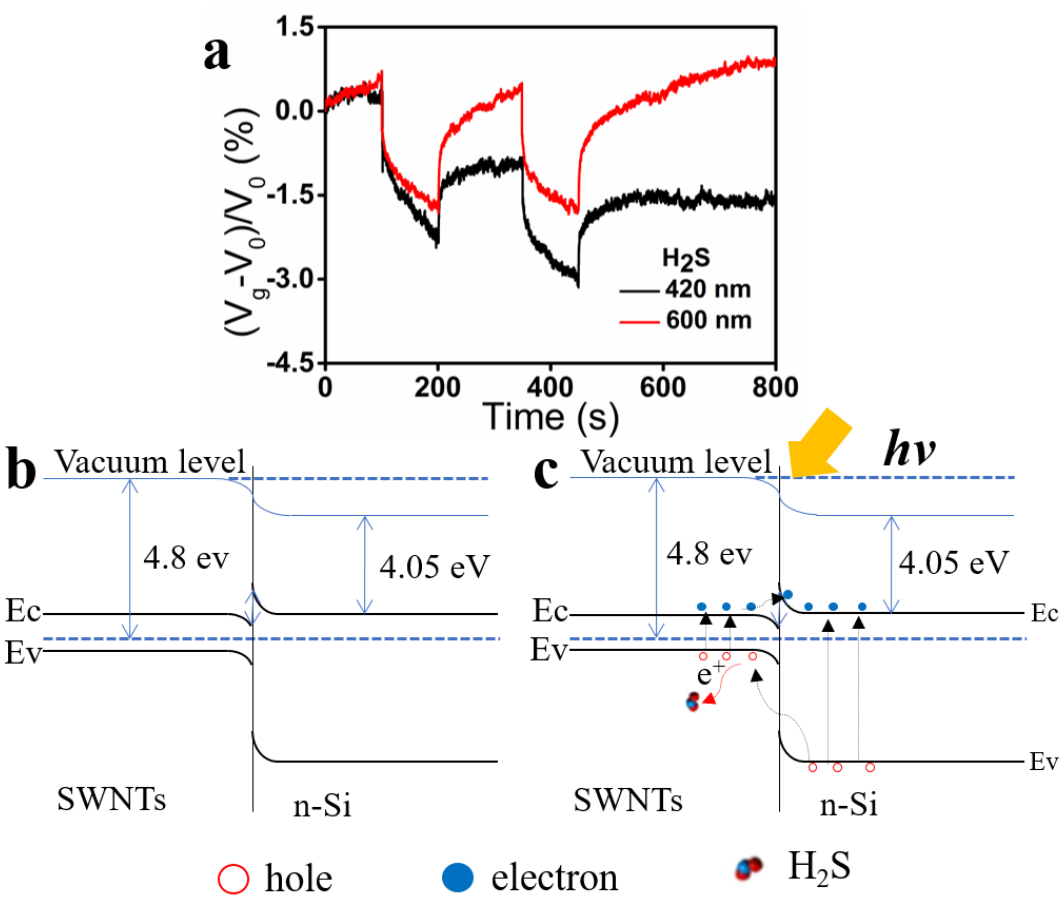

Figure 5.3 (a) The sensing response of photovoltaic self-powered H_2S sensor when applied different wavelength light (420 nm and 600 nm) with same power intensity (1.8 mW/cm^2); (b), (c) The schematic band diagram of the photovoltaic self-powered device at dark and illumination state.

5.4.4. Sensing Mechanism of Photovoltaic Self-powered Sensor

Figure 5.3b,c illustrates the schematic band structure diagram of the device, SWNT is a narrow bandgap p-type semiconductor in the air with the work function around 4.8 eV.[33] For the n-Si with a phosphor dopant concentration of 1015-1016 cm^{-3}, the band gap and work function of n-Si are about 1.12 eV and 4.05 eV, respectively, and the Femi level is 0.2 eV

below the conduction band [32,33]. At the dark state, the device is kept at a thermal equilibrium state and forms a BEF at the interface of SWNTs and n-Si as shown in Figure 5.3b. Once exposing to light with an energy above the band gap of SWNTs and n-Si, the balance state of the device will be changed due to the excited photogenerated carriers. After that the BEF will work as a power source to separate the photogenerated carriers and drive them to n-Si (electrons) and SWNTs (holes), respectively, forming photocurrent as well as the V_{oc} in the circuit. The n-Si and SWNTs both act as the e-h generators and also electrons and holes collectors, respectively, which benefit the transportation of electrons and holes [25, 27, 28]. When pumping into H_2S, H_2S molecule absorbs on the surface of SWNTs and extracts the holes from SWNTs, which decreases the concentration of photogenerated holes in the SWNTs. The electric current is defined as:

$$I=Q/t=Nq/t \qquad (5\text{-}1)$$

(Q refers to the electric charge per area, t refers time, N refers to the number of the electrons or holes, q refers to the value of charge). The decrease of the concentration of holes which is caused by absorbed H_2S molecule will reduce the value of photogenerate current (I_L).

On the other hand, the changing concentration of holes can also tune the value of V_{oc}. According to the ideal p-n heterojunction solar diode equation, the V_{oc} caused by the photo illumination can be obtained through followed formula [33]:

$$V_{oc} = \frac{kT}{q}\ln\left(\frac{I_L}{I_s}+1\right) \qquad (5\text{-}2)$$

where K is the Boltzmann constant, I_s is the reverse saturation current and I_L is the photogenerated current, respectively. Combined with the equations (1) and (2), the Voc closely relates the number of the carriers to the corresponding calculations and obtain the following equation:

$$V_{oc} = \frac{kT}{q} \ln\left(\frac{I_L}{I_s} + 1\right) = \frac{kT}{q} \ln\left(\frac{Nq}{t.I_s} + 1\right) \quad (5\text{-}3)$$

As the value of I_s is very small and usually can be regarded as a constant value, the decrease of holes will result in V_{oc} dropping, which is corresponding to the experimental results when the device is subjected to H_2S and the value of V_{oc} is decreased.

5.5. Conclusions

A Photovoltaic self-powered H_2S sensor based on SWNTs/Si heterojunction was successfully constructed. Owing to the existing BEF which can transform photon energy into electric energy, self-powered sensor detecting trace H_2S at room temperature was implemented. By comparison with chemiresistive sensors based on SWNTs-only, the sensing response and response time of self-powered sensor had greatly improved. The influence of the wavelength of light was investigated by applying different light (*e.g.*, 420 nm and 600 nm) with identical power density. The poor stability of sensor is greatly caused by the oxidation of Si in air ambient. This work may bring a novel idea and facile method to develop self-powered gas microsensors with good stability based on the rational p-n heterojunction design.

5.6. References

[1] T. Shaymurat, Q. Tang, Y. Tong, L. Dong, Y. Liu, Gas dielectric transistor of CuPc single crystalline nanowire for SO(2) detection down to sub-ppm levels at room temperature, Adv. Mater. 25 (2013) 2269-73, 376.

[2] D. Hines, M.H. Rümmeli, D. Adebimpe, D.L. Akins, High-yield photolytic generation of brominated single-walled carbon nanotubes and their application for gas sensing, Chem.Commun. 50 (2014) 11568-71.

[3] S. Mubeen, T. Zhang, N. Chartuprayoon, Y. Rheem, A. Mulchandani, N.V. Myung, M.A. Deshusses, Sensitive detection of H_2S using gold nanoparticle decorated single-walled carbon nanotubes, Anal. Chem. 82 (2010) 250-7.

[4] S. Cui, H. Pu, S.A. Wells, Z. Wen, S. Mao, J. Chang, M.C. Hersam, J. Chen, Ultrahigh sensitivity and layer-dependent sensing performance of phosphorene-based gas sensors, Nat. Commun. 6 (2015) 8632.

[5] G. Lu, L.E. Ocola, J. Chen, Room-Temperature Gas Sensing Based on Electron Transfer between Discrete Tin Oxide Nanocrystals and Multiwalled Carbon Nanotubes, Adv. Mater. 21 (2009) 2487-91.

[6] W. Li, P. Hou, C. Liu, D. Sun, J. Yuan, S. Zhao, L. Yin, H. Cong, H. Cheng, High-quality, highly concentrated semiconducting single-wall carbon nanotubes for use in field effect transistors and biosensors, ACS Nano 7 (2013) 6831-9.

[7] E.C.Silva, F.L. Urias, E.M. Sandoval, B.G. Sumpter, H. Terrones, J.C. Charlier, V. Meunier, M. Terrones, Phosphorus and phosphorus–nitrogen doped carbon nanotubes for ultrasensitive and selective molecular detection, Nanoscale 3 (2011) 1008-13.

[8] C. Dong, H. Luo, J. Cai, F. Wang, Y. Zhao, D. Li, Hydrogen sensing characteristics from carbon nanotube field emissions, Nanoscale 8 (2016) 5599-604.

[9] I. Dube, D. Jiménez, G. Fedorov, A. Boyd, I. Gayduchenko, M. Paranjape, P. Barbara, Understanding the electrical response and sensing mechanism of carbon-nanotube-based gas sensors, Carbon 87 (2015) 330-7.

[10] C. Zhou, J. Zhao, J. Ye, M. Tange, X. Zhang, W. Xu, K. Zhang, T. Okazaki, Z. Cui, Printed thin-film transistors and NO_2 gas sensors based on sorted semiconducting carbon nanotubes by isoindigo-based copolymer, Carbon 108 (2016) 372-80.

[11] E. Comini, A. Cristalli, G. Faglia, G. Sberveglieri, Light enhanced gas sensing properties of indium oxide and tin dioxide sensors, Sens. Actuators B Chem. 65 (2000) 4.

[12] S. Park, S. An, Y. Mun, C. Lee, UV-enhanced NO_2 gas sensing properties of SnO_2-core/ZnO-shell nanowires at room temperature, ACS applied materials & interfaces, 5 (2013) 4285-92.

[13] S. Park, H. Ko, S. Kim, C. Lee, UV-activated room temperature NO_2 gas sensing using $In_2Ge_2O_7$ nanofiber sensors, Mater. Res. Bull. 58 (2014) 5.

[14] Z. Yang, L. Guo, B. Zu, Y. Guo, T. Xu, X. Dou, CdS/ZnO Core/Shell Nanowire-Built Films for Enhanced Photodetecting and Optoelectronic Gas-Sensing Applications, Adv. Opt. Mater. 2 (2014) 738-45.

[15] A. Popa, J. Li, A.C. Samia, Hybrid Platinum Nanobox/Carbon Nanotube Composites for Ultrasensitive Gas Sensing, Small (2013).

[16] J. Wang, Y. Kwak, I.-y. Lee, S. Maeng, G.-H. Kim, Highly responsive hydrogen gas sensing by partially reduced graphite oxide thin films at room temperature, Carbon 50 (2012) 4061-7.

[17] F.K.P. E. S. Snow, E.J. Houser, S.C. Badescu, T.L. Reinecke, Chemical Detection with a Single-Walled Carbon Nanotube Capacitor, Science 307 (2005) 5.

[18] Y. Yang, H. Zhang, J. Chen, S. Lee, T. Hou, Z. Wang, Simultaneously harvesting mechanical and chemical energies by a hybrid cell for self-powered biosensors and personal electronics, Energy & Environmental Science 6 (2013) 1744.

[19] X. Xue, Y. Nie, B. He, L. Xing, Y. Zhang, Z. Wang, Surface free-carrier screening effect on the output of a ZnO nanowire nanogenerator and its potential as a self-powered active gas sensor, Nanotechnology 24 (2013) 225501.

[20] S. Xu, Y. Qin, C. Xu, Y. Wei, R. Yang, Z. Wang, Self-powered nanowire devices, Nature nanotechnology, 5 (2010) 366-73.

[21] M. Zhu, X. Li, S. Chung, L. Zhao, X. Li, X. Zang, K. Wang, J. Wei, K. Zhou, D. Xie, H. Zhu, Photo-induced selective gas detection based on reduced graphene oxide/Si Schottky diode, Carbon 84 (2015) 138-45.

[22] M.W. Hoffmann, L. Mayrhofer, O. Casals, L. Caccamo, F.H. Ramirez, G. Lilienkamp, W. Daum, M. Moseler, A. Waag, H. Shen, J.D.Prades, A highly selective and self-powered gas sensor via organic surface functionalization of p-Si/n-ZnO diodes, Adv. Mater. 26 (2014) 8017-22.

[23] M.W.G. Hoffmann, A.E. Gad, J.D. Prades, F.H. Ramirez, R. Fiz, H. Shen, S. Mathur, Solar diode sensor: Sensing mechanism and applications, Nano Energy, 2 (2013) 514-22.

[24] G. Li, L. Liu, G. Wu, W. Chen, S. Qin, Y. Wang, T. Zhang, Self-Powered UV-Near Infrared Photodetector Based on Reduced Graphene Oxide/n-Si Vertical Heterojunction, Small 12 (2016) 5019-26.

[25] Y. Jia, A. Cao, X. Bai, Z. Li, L. Zhang, N. Guo, J. Wei, K. Wang, H. Zhu, D. Wu, P.A. Ajayah, Achieving high efficiency silicon-carbon nanotube heterojunction solar cells by acid doping, Nano lett. 11(2011) 1901-5.

[26] X. Wang, G. Li, R. Liu, H. Ding, T. Zhang, Reproducible layer-by-layer exfoliation for free-standing ultrathin films of single-walled carbon nanotubes, J. Matet. Chem. 22 (2012) 21824.

[27] H. Sun, J. Wei, Y. Jia, X. Cui, K. Wang, D. Wu, Flexible carbon nanotube/mono-crystalline Si thin-film solar cells, Nanoscale Res. Lett. 9 (2014) 514-519.

[28] T. Uchino, F. Shimpo, T. Kawashima, G.N. Ayre, D.C. Smith, C.H. de Groot, P.Ashburn, Electrical transport properties of isolated carbon nanotube/Si heterojunction Schottky diodes, Appl. Phys. Lett. 103 (2013) 193111.

[29] X. Li, Y. Jung, J.-S. Huang, T. Goh, A.D. Taylor, Device Area Scale-Up and Improvement of SWNT/Si Solar Cells Using Silver Nanowires, Adv. Energy Mater., 4(2014) 1400186.

[30] X. Li, Y. Jung, K. Sakimoto, T.-H. Goh, M.A. Reed, A.D. Taylor, Improved efficiency of smooth and aligned single walled carbon nanotube/silicon hybrid solar cells, Energy & Environmental Science 6 (2013) 879.

[31] P. Liu, Q. Sun, F. Zhu, K. Liu, K. Jiang, L. Liu, Q. Li, S. Fan, Measuring the work function of carbon nanotubes with thermionic method, Nano lett. 8 (2008) 647-51.

[32] A. Chen, K. Zhu, Effects of TCO work function on the performance of TCO/n-Si hetero-junction solar cells, Solar Energy 107 (2014) 195-201.

[33] S. M. Sze, K. K. Ng, Physics of Semiconductor Device, Wiley, 2006.

[34] Y. Jia, P. Li, X. Gui, J. Wei, K. Wang, H. Zhu, D. Wu, L. Zhang, A. Cao, Y. Xu, Encapsulated carbon nanotube-oxide-silicon solar cells with stable 10% efficiency, Appl. Phys. Lett. 98 (2011) 133115.

[35] T. Cui, R. Lv, Z. Huang, S. Chen, Z. Zhang, X. Gan, .Y. Jia, X. Li, D. Wu, F. Kang, Enhanced efficiency of graphene/silicon heterojunction solar cells by molecular doping, J. Mater. Chem. A 1 (2013) 5736.

[36] G. Vall-Llosera, E. Melero Garcia, A. Kivimaki, E. Rachlew, M. Coreno, M. de Simone, et al., Fluorescence emission from photo-fragments after resonant S 2p excitations in H_2S, Phys. Chemi. Chem. Phys. : PCCP 9 (2007) 389-95.

5.7. Supplementary Data

Design of Photovoltaic Self-powered Gas Sensor based on Single-walled Carbon Nanotubes/Si p-n Heterojunction

Figure S5.1 is the schematic fabrication procedure of the self-powered gas sensor based on SWNTs/Si. First lithography mask with different patterns were designed and an n-type Si wafer with a layer of 300 nm SiO_2 was patterned to expose Si surface (five identical effective sensing area 5*100 μm*500 μm and one area for sputtering electrode 400 μm*400 μm) via photolithography and reactive ion etching (RIE). Second, patterned Ti/Au electrodes (~20 nm Ti and ~150 nm Au) were fabricated by photolithography and sputtering processes. After fabricating the microchip, SWNTs (Sigma Inc.) were purified by annealing under 300 ^{o}C for 2 h in a tube furnace and then treated with concentrated HCl and 30 % H_2O_2 with volume ratio 3:1 at 60 ^{o}C for 6 h. The purified SWNTs were dispersed in dimethylformamide (DMF) via sonication for 4 h to form homogenous SWNTs dispersion (0.01 mg/ml). The as-prepared SWNTs dispersion was then drop-casted onto the prefabricated sensor chip to form a SWNT network. To remove the solvent left on SWNT network and reduce the contact resistance between SWNTs and the Ti/Au electrodes, the prepared devices were annealed in a tube furnace under pure Ar gas at 300 ^{o}C for 20 minutes.

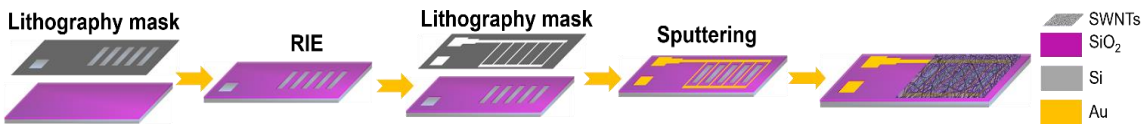

Figure S 5.1 Schematic fabrication process of gas sensor.

Figure S5.2b is the SEM image of the SWNT film which is covered on the Si and SiO_2 surface. As the thickness of SiO_2 layer is 300 nm, there is an obvious ledge at the interface of Si and SiO_2 layer and mesh-like SWNT film is worked as a bride to connect Si and SiO_2. Figure S5.2a and c are the EDXS results of two different locations (Si/SWNTs and Si/SiO_2/SWNTs).

The contents of C atom in both locations are very low which can indicate that the SWNT film is very thin. By comparison, the percentage of O atom increases from 0% to 19.51% owing to the existing of SiO_2 layer.

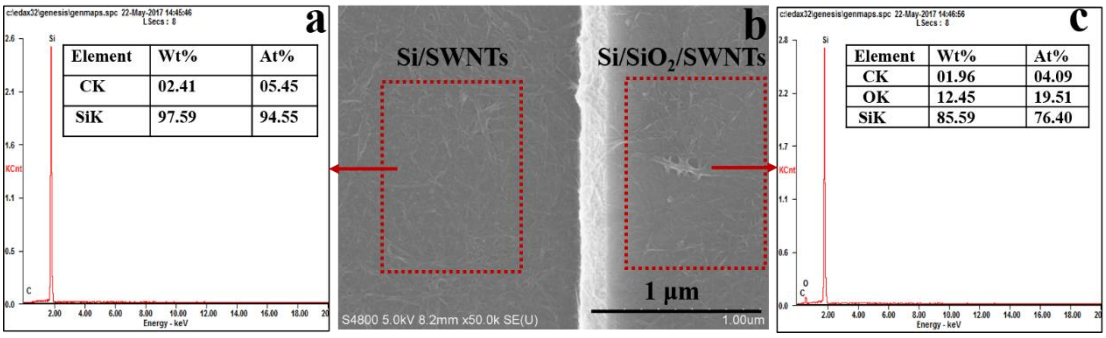

Figure S 5.2 (a), (c) The EDXS results of sensor at different locations; (b) The SEM image of the sensor at specific.

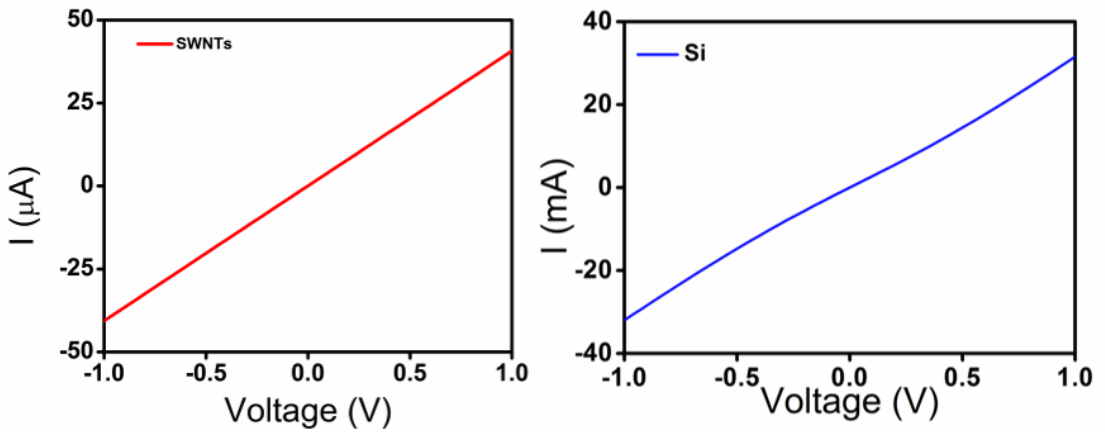

Figure S 5.3 (a) The Current-Voltage (I-V) curves of SWNTs-only device after annealed treatment. (b) The Current-Voltage (I-V) curves of n-Si-only device.

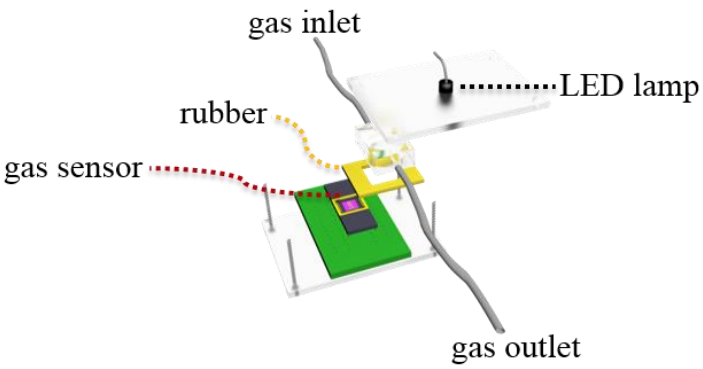

Figure S 5.4 Schematic graph of gas sensor testing process, all parts of the testing system are vertically placed.

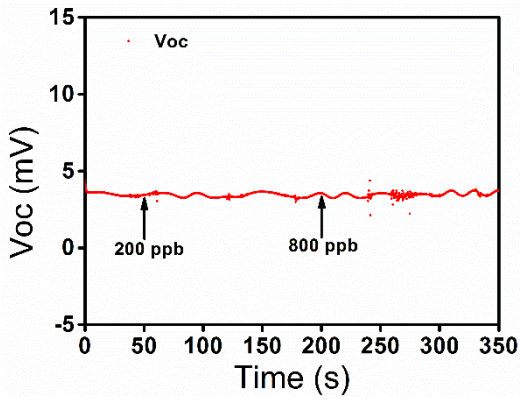

Figure S 5.5 The sensing response of photovoltaic self-powered gas sensor under dark state.

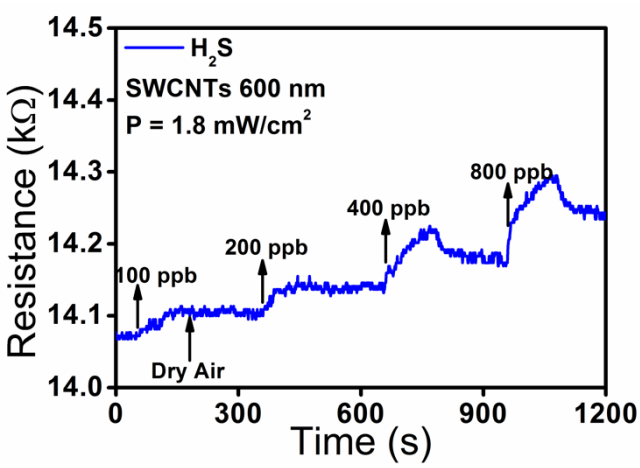

Figure S 6.6 Dynamic response of conventional SWNTs-only device to different H_2S concentration (V_{ds} = 2 V, λ = 600 nm, P = 1.8 mW/cm^2).

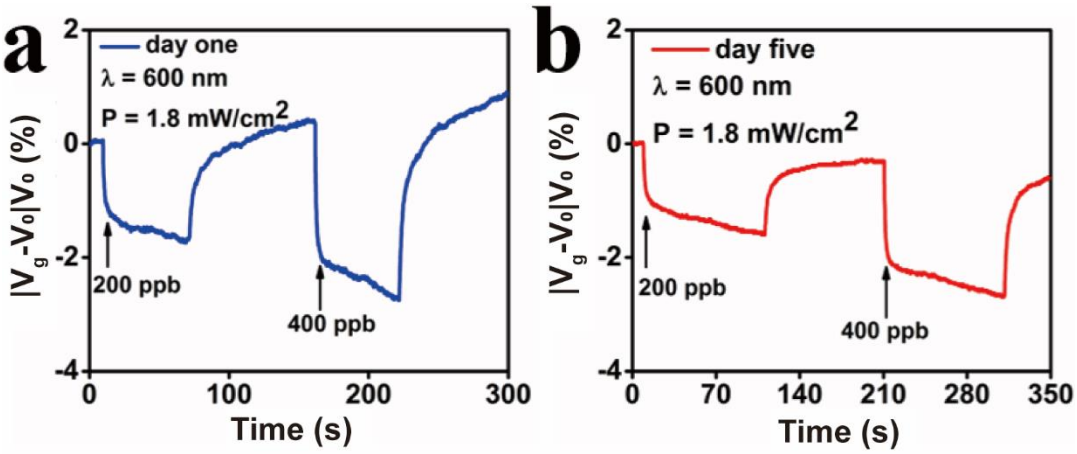

Figure S 6.7 Dynamic response of sensor to different concentration of H_2S at day one (a), and after five days (b) (λ = 600 nm, P = 1.8mW/cm^2).

This page intentionally left blank

Chapter 6: General Conclusion and Future Work

6.1 General Conclusion

In this thesis, three different heterostructure-based gas sensors were studied in order to enhance their sensing performance (sensitivity, stability, and low-power consumption, etc.). In addition, a “top-down” & “bottom-up” strategy was proposed to fabricate miniaturized gas sensors in wafer-scale with high-throughput.

The hydrothermal method is a very common method to prepare and design sensing materials with different structures. The brush-like (B-) ZnO@SnO_2 hierarchical nanostructures (HNSs) (one kind of type-II heterostructure) were synthesized through a simple two-step hydrothermal method without templates and surfactants for NO_2 sensing. By investigating the effects of growth time and reaction temperature, a “dissolution- recrystallization” growth mechanism was proposed. Most of the SnO_2 nanowires were inclined at an angle of 56° to surface of ZnO. Furthermore, the HRTEM images revealed that the (110) plane of SnO_2 and the (01-10) plane of ZnO lattice fringes were connected at the hetero-interface with a ~4° tilt, which results from the lattice mismatch between SnO_2 and ZnO. These defects provide preferential adsorption sites for the NO_2 and oxygen species thus enhancing the sensitivity. In addition, both the enhanced specific surface area and synergism effect of the formed multi-junction contributed to the enhancement in sensitivity. In this case, the main conduction channel was confined to the SnO_2 nanowires, as the ZnO nanorods were densely covered by the SnO_2 nanowires. The detail sensing mechanism was discussed in Chapter 2. Compared with pure SnO_2 and ZnO-based sensors, the sensing performance of ZnO@SnO_2 heterostructure-based sensor to NO_2 was significantly increased.

In most cases, chemiresistive sensors are prepared by slurry-coating or drop-casting sensing materials onto a micro-electrode chip using organic reagents as binders, which is

shown in Chapter 2. However, the sensing materials are chaotically distributed on the micro-electrode chip. As a result, the reproducibility of the prepared sensors is rather poor. In addition, the sensors may also experience poor stability due to the weak interconnection between the sensing materials and the micro-electrode chip compared with in situ growth method. Thus, in Chapter 3, NiO@SnO_2 HNSs were directly grown on the ceramic chip tightly via a two-step chemical bath deposition method for H_2S sensing without templates and binders. The morphology of the NiO@SnO_2 HNSs could be controlled by varying the growth time and the NiO@SnO_2 HNSs was uniformly grown on the ceramic chip. The NiO@SnO_2 HNS-based sensor demonstrated a good stability as the sensitivity of the sensor changed less than 3% after one month. In contrast to the ZnO@SnO_2 HNSs studied in Chapter 2, the conduction channel of the NiO@SnO_2 HNSs was confined to the NiO nanowalls due to the different fabrication process. Thus, the formed p-n heterojunction between NiO and SnO_2 can efficiently modulate the conduction channel of NiO when exposed to different gases.

Reproducibility in performance is very important when considering large-scale production of commercial devices. In situ growth of the sensing materials on the micro-electrode chip is a potential solution to tackle the reproducibility issue of the sensor fabrication. A “top-down” & “bottom-up” strategy was proposed in Chapter 4 for wafer-scale fabrication of gas sensors by in situ growth of the sensing material patterns at designed locations. After fabricating micro-hotplates via the “top-down” strategy (MEMS fabrication techniques), a controllable templated-guided de-wetting method was utilized to assemble porous TPE film with uniform micro-holes (RSD of the micro-hole size < 3.5 %, n >300). Then, the sensing materials were directly growing in the micro-hole areas, namely “bottom-up” strategy. The obtained gas microsensors based on this strategy showed great reproducibility of electric properties (RSD < 0.8%, n=8) and sensing response (RSD <3.5%, n=8) toward real-time H_2S detection. This fabrication strategy shows great potential to fabricate wafer-scale miniaturized

gas sensors based on different sensing materials due to the good chemical and thermal stability of TPE film. The template-guided controllable de-wetting method also shows feasibility to assemble different porous films and patterned materials.

The metal oxide-based chemiresistive sensors not only require high working temperature but also need external power sources to drive the sensors which greatly increase the energy consumption. As discussed in Chapter 1, constructing type-III heterostructure is a feasible approach to fabricate photovoltaic self-powered gas sensors. Therefore, in Chapter 5, a photovoltaic self-powered gas sensor based on SWNTs@Si p-n heterojunction was developed via a facile method by drop-casting SWNTs solutions onto the Si based sensor chip. Owing to the existence of BEF which can transform photon energy into electric energy, a self-powered sensor capable of detecting trace concentrations of H_2S at room temperature was developed. This work may bring a novel idea and facile method to develop self-powered gas microsensors based on the rational p-n heterojunction design.

Overall, the present research demonstrated that (1) constructing heterostructures is an effective way to enhance the sensing performances compared with single sensing materials, (2) the sensing mechanism of sensors depends on the structure of the devices (geometric structure or electronic structure), (3) integrating microfabrication techniques with in situ growth methods is a potential strategy to implement wafer-scale fabrication of gas sensors and guarantee the reproducibility in performance of the obtained sensors, and (4) it is possible to construct self-powered gas sensors to reduce the energy consumption by designing special device structure..

6.2. Future Work

In Chapter 2, the sensor based on ZnO@SnO_2 HNSs shows the highest sensing response to NO_2 among interference gases such as acetone, NH_3, C_7H_8, $CHCl_3$, H_2S, and ethanol under the air condition background. As all the interference gases are reducing gases, the sensing behavior of the sensor to NO_2 must be different from the interference gases. Therefore, the

SnO_2@ZnO HNS-based sensor in this case cannot confirm that it can distinguish NO_2 from other oxidizing gases. According to the discussion in the Chapter 2, the high sensitivity to NO_2 may ascribe to high electron affinity of NO_2 (2.273 eV). By searching the "LANGE'S HAND BOOK OF CHEMISTRY", the electron affinity of NO_2 is much higher than some oxidizing gases such as NO (0.026 eV), O_3 (2.1028 eV), O_2 (0.45 eV), SO_2 (1.107 eV) and SO_3 (1.97 eV), but is lower than Cl_2 (2.38 eV) and F_2 (3.01 eV) [1]. The SnO_2@ZnO HNS-based sensor may be also very sensitive to Cl_2 and F_2. Thus, to confirm the selectivity of oxidizing gas sensors, more oxidizing gases (e.g., O_3, SO_2, Cl_2) are needed to serve as interference gases at different working temperatures in the future. In Chapter 3, a high performance H_2S sensor based on NiO@SnO_2 HNSs is successfully implemented, which is prepared by two-step in situ growth method. The lowest H_2S concentration (100 ppb), which is tested in this case, is a little higher than the EPA standard (50 ppb) [2]. Although the calculated theoretical detection limitation is estimated to be around 1.5 ppb, a more scientific way is demanded to directly detect ultralow concentration (several ppb level) of H_2S to confirm the detection limitation in the future.

In Chapter 4, I have implemented wafer-scale fabrication of gas sensors based on NiO nanowalls via "top-down" & "bottom-up" strategies. This fabrication process shows a great potential in wafer-scale fabrication of gas microsensors based on various nanomaterials. Future work should link to current research to design and construct more heterostructural nanomaterials for better sensing performance. Then, exploration of the applications of wafer-scale fabrication method to design other devices and sensor arrays. Metal organic frameworks (MOFs) with uniform pores, large specific surface areas and exposed-metal sites has aroused great attention in the scientific society [3-5]. Besides, MOFs demonstrate the ability for selective adsorption of gas molecules, which is very attractive in the gas sensing field [6-8]. Thus, it is potentially an ideal material to address the selectivity of gas sensors. Moreover, by

designing the hydrophobic MOF, it is feasible to fabricate gas sensors which are non-sensitive to humidity. In order to implement wafer-scale fabrication of gas microsensors based on MOFs with no response to humidity, in the future several questions remain to be answered:

1. How can MOFs be grown on the surface of specific metal oxides to enhance the selectivity?

2. How can patterned sensing materials be formed based on previous work?

3. Is it possible to grow in situ conducting MOFs on different substrates to expand the applications of the fabrication strategy?

To overcome the above challenges, I am planning to functionalize the metal oxides to produce some functional groups that can interact with metal ions or ligands for epitaxial growth of MOF in liquid phase. In addition, it is possible to use the metal oxides as the metal ion source for growing MOF [9]. Hence, it is a potential approach to form patterned metal oxide@MOF heterostructures to enhance the selectivity by confining locations of metal oxides. As some reported metal oxide@MOF-based sensors still require high operation temperatures, so direct growth of conducting MOFs on a micro-electrode chip without corrosion of electrodes may be a feasible solution to fabricate a room temperature gas sensor [9-11]. However, the specific effect of MOF and the interaction between MOF and host materials are still not very clear. Thus, it is worth studying the sensing mechanism of metal oxide@MOF- or pure MOF-based sensors to address the research gap.

All the chemiresistive gas sensors reported in this thesis have achieved high sensing performance (*e.g.*, high sensitivity and good selectivity). However, there is still a long way for practical applications. For example, the long-term stability of gas sensors under working conditions is not presented based on the current lab conditions. Thus, in the future, a new instrument will be constructed to provide the working temperature for sensors continuously

and test the sensing performance of sensors periodically. By designing this kind of instrument, the stability the sensor can be systematically studied. The comparison results between sensors prepared in lab and commercial sensors will be investigated under same condition to evaluate the possibility of practical applications of prepared sensors.

In Chapter 5, a novel photovoltaic self-powered gas sensor based on SWNTs/Si p-n heterojunction is reported. However, the stability of the self-powered is rather poor since the Si is easily oxidized in air ambient which can greatly influence the photovoltaic effect of the sensor [12,13]. In addition, the sensitivity and selectivity of photovoltaic self-powered sensors are rather poor compared with chemiresistive gas sensors. Thus, to obtain high performance photovoltaic self-powered gas sensor, the following factors are worth to be taken into consideration. First, selecting suitable semiconductor materials to construct self-powered gas sensors. For example, the chemical stability of semiconductors can greatly influence the stability of sensors. The band gap of the semiconductors can determine whether the sensors can be driven by the UV light or visible light. Second, studying the photovoltaic effect of the photovoltaic self-powered gas sensor. As the sensing performance of photovoltaic self-powered gas sensor is studied by measuring the change in photogenerated current or V_{oc}, the photovoltaic effect of the sensor is worth studying to profoundly understand the sensing mechanism. Last, figuring out how the sensitivity and selectivity of photovoltaic self-powered gas sensor can be improved. Therefore, self-powered gas sensors with high performance are still a long way off to address the above remaining problems.

6.3. References

[1] Dean, J. A., in Lange's Handbook of Chemistry 70 edn, McGraw-Hill Professional, 2004, Ch. 4.

[2] "NAAQS Table", United States Environmental Protection Agency, https://www.epa.gov/criteria-air-pollutants/naaqs-table.

[3] M.S. Yao, W.X. Tang, G.E. Wang, B. Nath, G. Xu, MOF Thin Film-Coated Metal Oxide Nanowire Array: Significantly Improved Chemiresistor Sensor Performance, Adv. Mater. 28(2016) 5229-34.

[4] K. Rui, X. Wang, M. Du, Y. Zhang, Q. Wang, Z. Ma, Q. Zhang, D. Li, X. Huang, G. Sun, J. Zhu, W. Huang, Dual-Function Metal-Organic Framework-Based Wearable Fibers for Gas Probing and Energy Storage, ACS Appl. Mater. Interfaces 10(2018) 2837-42.

[5] S. Aguado, J. Canivet, D. Farrusseng, Facile shaping of an imidazolate-based MOF on ceramic beads for adsorption and catalytic applications, Chem. Commun. 46(2010) 7999-8001.

[6] L. Guo, M. Wang, D. Cao, A Novel Zr-MOF as Fluorescence Turn-On Probe for Real-Time Detecting H2 S Gas and Fingerprint Identification, Small 14(2018) e1703822.

[7] J. Gao, C. Huang, Y. Lin, P. Tong, L. Zhang, In situ solvothermal synthesis of metal-organic framework coated fiber for highly sensitive solid-phase microextraction of polycyclic aromatic hydrocarbons, J Chromatogr A 1436(2016) 1-8.

[8] H. Fu, D. Zhu, In situ hydrothermal grown silicalite-1 coating for solid-phase microextraction, Anal. Chem. 84(2012) 2366-72.

[9] I. Stassen, N. Burtch, A. Talin, P. Falcaro, M. Allendorfc, R. Ameloot, An updated roadmap for the integration of metal-organic frameworks with electronic devices and chemical sensors, Chem. Soc. Rev. 46(2017) 3185-3241.

[10] M. Yao, W. Tang, G. Wang , B. Nath, G. Xu, MOF Thin Film-Coated Metal Oxide Nanowire Array:Significantly Improved Chemiresistor Sensor Performance, Adv. Mater. 28(2016) 5229-5243.

[11] H. Tian, H. Fan, M. Li, L. Ma, Zeolitic Imidazolate Framework Coated ZnO Nanorods as Molecular Sieving to Improve Selectivity of Formaldehyde Gas Sensor, ACS Sens. 1(2016) 243-250.

[12] Y. Jia, X. Cui, J. Wei, K. Wang, H. Zhu, D. Wu, L. Zhang, A. Cao, Y. Xu, Encapsulated carbon nanotube-oxide-silicon solar cells with stable 10% efficiency, Appl. Phys. Lett. 98(2011) 133115.

[13] Y. Jia, A. Cao, X. Bai, Z. Li, N. Guo, J. Wei, K. Wang, H. Zhu, D. Wu, P. Ajayan, Achieving High Efficiency Silicon-Carbon Nanotube Heterojunction Solar Cells by Acid Doping, Nano Lett. 11(2011) 1901-1905.